

Non-Epitaxial Thin-Film Indium Phosphide Photovoltaics: Growth, Devices, and Cost Analysis

Maxwell Zheng



Electrical Engineering and Computer Sciences
University of California at Berkeley

Technical Report No. UCB/EECS-2015-226

<http://www.eecs.berkeley.edu/Pubs/TechRpts/2015/EECS-2015-226.html>

December 1, 2015

Copyright © 2015, by the author(s).
All rights reserved.

Permission to make digital or hard copies of all or part of this work for personal or classroom use is granted without fee provided that copies are not made or distributed for profit or commercial advantage and that copies bear this notice and the full citation on the first page. To copy otherwise, to republish, to post on servers or to redistribute to lists, requires prior specific permission.

NON-EPITAXIAL THIN-FILM INDIUM PHOSPHIDE PHOTOVOLTAICS:
GROWTH, DEVICES, AND COST ANALYSIS

By

Maxwell S Zheng

A dissertation submitted in partial satisfaction of the

requirements for the degree of

Doctor of Philosophy

in

Engineering – Electrical Engineering and Computer Sciences

in the

Graduate Division

of the

University of California, Berkeley

Committee in charge:

Professor Ali Javey, Chair

Professor Ming C Wu

Professor Roya Maboudian

Spring 2015

NON-EPITAXIAL THIN-FILM INDIUM PHOSPHIDE PHOTOVOLTAICS:
GROWTH, DEVICES, AND COST ANALYSIS

Copyright © 2015
Maxwell S Zheng

Abstract

NON-EPITAXIAL THIN-FILM INDIUM PHOSPHIDE PHOTOVOLTAICS: GROWTH, DEVICES, AND COST ANALYSIS

by

Maxwell S Zheng

Doctor of Philosophy in Electrical Engineering and Computer Sciences

University of California, Berkeley

Professor Ali Javey, Chair

In recent years, the photovoltaic market has grown significantly as module prices have continued to come down. Continued growth of the field requires higher efficiency modules at lower manufacturing costs. In particular, higher efficiencies reduce the area needed for a given power output, thus reducing the downstream balance of systems costs that scale with area such as mounting frames, installation, and soft costs. Cells and modules made from III-V materials have the highest demonstrated efficiencies to date but are not yet at the cost level of other thin film technologies, which has limited their large-scale deployment. There is a need for new materials growth, processing and fabrication techniques to address this major shortcoming of III-V semiconductors.

Chapters 2 and 3 explore growth of InP on non-epitaxial Mo substrates by MOCVD and CSS, respectively. The results from these studies demonstrate that InP optoelectronic quality is maintained even by growth on non-epitaxial metal substrates. Structural characterization by SEM and XRD show stoichiometric InP can be grown in complete thin films on Mo. Photoluminescence measurements show peak energies and widths to be similar to those of reference wafers of similar doping concentrations.

In chapter 4 the TF-VLS growth technique is introduced and cells fabricated from InP produced by this technique are characterized. The TF-VLS method results in lateral grain sizes of $>500 \mu\text{m}$ and exhibits superior optoelectronic quality. First generation devices using a *n*-TiO₂ window layer along with *p*-type TF-VLS grown InP have reached $\sim 12.1\%$ power conversion efficiency under 1 sun illumination with V_{OC} of 692 mV, J_{SC} of 26.9 mA/cm², and FF of 65%. The cells are fabricated using all non-epitaxial processing. Optical measurements show the InP in these cells have the potential to support a higher V_{OC} of ~ 795 mV, which can be achieved by improved device design.

Chapter 5 describes a cost analysis of a manufacturing process using an InP cell as the active layer in a monolithically integrated module. Importantly, TF-VLS growth avoids the hobbles of traditional growth: the epitaxial wafer substrate, low utilization efficiency of expensive metalorganic precursors, and high capital depreciation costs due to low throughput. Production costs are projected to be $\$0.76/W_{(\text{DC})}$ for the benchmark case of 12% efficient modules and would decrease to $\$0.40/W_{(\text{DC})}$ for the long-term potential case of 24% efficient modules.

To my family

TABLE OF CONTENTS

CHAPTER 1	INTRODUCTION	1
1.1	Solar energy and photovoltaics	1
1.2	The case for III-V photovoltaics	6
1.3	The advantage of polycrystalline InP	7
1.4	In this dissertation	8
CHAPTER 2	POLYCRYSTALLINE INP GROWN BY MOCVD	14
2.1	Introduction	14
2.2	Experimental details	14
2.3	Results and discussion	15
2.4	Conclusions	23
CHAPTER 3	POLYCRYSTALLINE INP GROWN BY CSS	25
3.1	Introduction	25
3.2	Experimental details	25
3.3	Results and discussion	26
3.4	Conclusions	33
CHAPTER 4	POLYCRYSTALLINE THIN-FILM INP SOLAR CELLS	36
4.1	Introduction	36
4.2	Polycrystalline InP grown by the TF-VLS method	36
4.3	Fabrication and device structure	39
4.4	Optoelectronic structure	40
4.5	<i>Ex-situ</i> p-doping using Zn	45
4.6	Device performance and characterization	47

4.7	Optical “J-V” and future potential	51
4.8	Conclusions	55
CHAPTER 5	MANUFACTURING COST ANALYSIS OF TF-VLS GROWTH	59
5.1	Introduction	59
5.2	Current cell structure and benchmark cell performance	60
5.3	Proposed module architecture and manufacturing process flow	61
5.4	Manufacturing cost analysis	62
5.5	Module cost per watt projections	66
5.6	Conclusions	67
CHAPTER 6	SUMMARY AND FUTURE OUTLOOK	70
APPENDIX A	SUPPLEMENTARY INFORMATION FOR CHAPTER 3	73

ACKNOWLEDGEMENTS

I have been fortunate in my time at Berkeley to be mentored by and work with many, many talented people. Without their help and support, this dissertation would not have been possible. First and foremost, I must thank my advisor, Professor Ali Javey. I am grateful that you took a chance on me many years ago. It has been truly educational to learn from you how to present, to negotiate, and to achieve ambitious visions. I also thank my qualifying and dissertation committee for their time and feedback on my research: Professor Ming Wu, Professor Roya Maboudian, and Professor Daryl Chrzan.

I must also thank in particular Professor Rehan Kapadia and Daniel Ruebusch for teaching me nearly everything I know about device physics (and their patience all the while). I'm also thankful for my research mentors, who taught me to conduct experiments properly: Professor Yuegang Zhang, Professor Yu-Lun Chueh, Dr. Corsin Battaglia, Dr. Joel Ager, Professor Kuniharu Takei, Dr. Daisuke Kiriya, Professor Johnny Ho, Professor Zhiyong Fan, Professor Hyunhyub Ko, Professor Zhibin Yu, and Professor Cary Pint. Additionally I would like to thank those who I've worked closely with at Berkeley: Joy Wang, Mark Hettick, Dr. Hui Fang, Jeff Beeman, Matin Amani, Dr. Xingtian Yin, and Dr. Carolin Sutter-Fella. My collaborators at the Molecular Foundry: Dr. Shaul Aloni and Dr. Tevye Kuykendall. My collaborators at NREL: Kelsey Horowitz and Dr. Michael Woodhouse. My collaborators at Purdue: Dr. Xufeng Wang, James Moore, Professor Peter Bermel, and Professor Mark Lundstrom. And finally all the other wonderfully talented scientists, postdoctoral researchers, and students I've been fortunate enough to work and interact with: Professor Min Hyung Lee, Dr. Yongjing Lin, Junjun Zhang, Dr. Tae Joon Seok, Yu-Ze Chen, James Bullock, Hank Wang, Peter Lobaccaro, Dr. Cheng-Ying Chen, Dr. Wei-Tse Hsu, Dr. Jingsan Xu, Dr. Shrek Xu, Professor Kin Man Yu, Dr. Wladek Walukiewicz, Professor Junghyo Nah, Professor Chuan Wang, Dr. Alexandra Ford, Professor Morten Madsen, Dr. Steven Chuang, Dr. Toshitake Takahashi, Dr. Hiroki Ota, Dr. Hiroshi Shiraki, Dr. Yuping Zeng, Kevin Chen, Sujay Desai, Thomas Rembert, Peter Zhao, Mahmut Tosun, Danny Lien, and Keeyoung Cho.

CHAPTER 1

INTRODUCTION

1.1 SOLAR ENERGY AND PHOTOVOLTAICS

Compared to all other energy resources known to man, there is no greater one than the sun. It can provide $\sim 23,000$ TW of power per year, dwarfing the total annual world power consumption (Fig. 1).¹ It is far larger than other renewable or sustainable sources and the amount of energy supplied by the sun in one year is larger than all known non-sustainable fossil fuel sources combined. In theory, the solar resource is large enough to supply all the world's energy needs indefinitely. In practice, there is still some work left to make this a reality. One method to harness solar power is

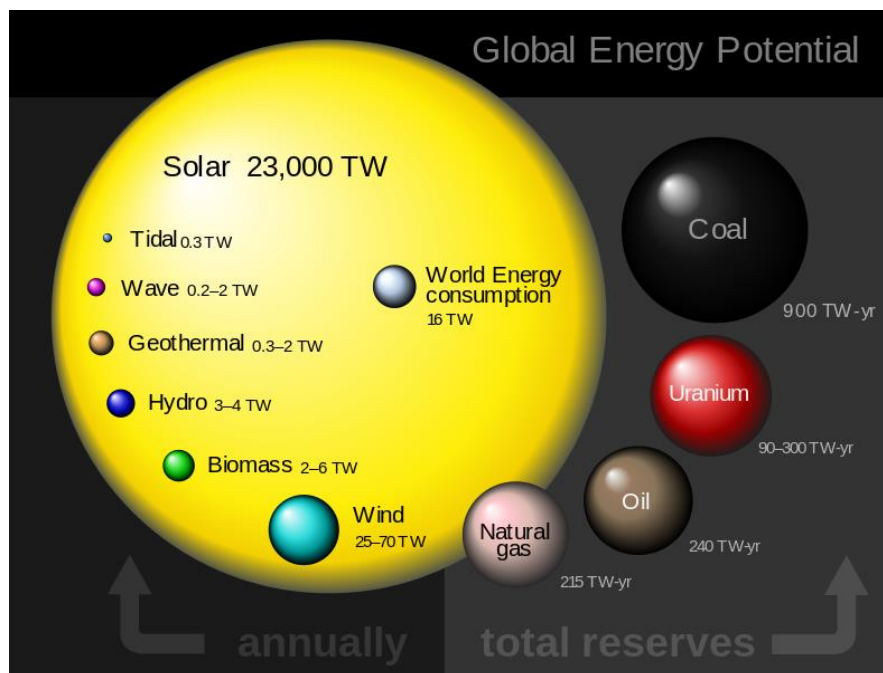


Figure 1. Energy potential of various sustainable and non-sustainable energy resources. (Reproduced from http://en.wikipedia.org/wiki/Solar_energy, data from Perez and Perez).¹

using photovoltaics (PV), which convert sunlight directly into electricity. PVs also have the important benefits of no greenhouse gas emissions during the operating lifetime, and allowing countries without domestic fossil fuel resources to achieve energy independence. The primary roadblock in the past for widespread adoption of PVs is that photovoltaic power systems are too expensive compared to conventional generation sources. This is rapidly changing however.

1.1.1 Cost metrics for PV systems

Because different energy generation methods have different economics and different modes of operation, a common metric called the levelized cost of electricity (LCOE, typically quoted in \$/MWh or ¢/kWh) is used to compare them.² The LCOE is calculated by taking the total cost of the energy generation asset (ex.: natural gas turbine, solar farm) divided by the total energy produced over the lifetime of that asset. The total costs consist of construction, operation and maintenance, decommissioning, financing, etc.³ Fig. 2 shows a comparison of the projected LCOE for a few types of utility scale non-sustainable and sustainable energy generation plants in the US.² The LCOE of PV systems has a large regional variation, and while the low end is already entering the range of conventional sources of ~6-10 ¢/kWh, the average LCOE is still too high.

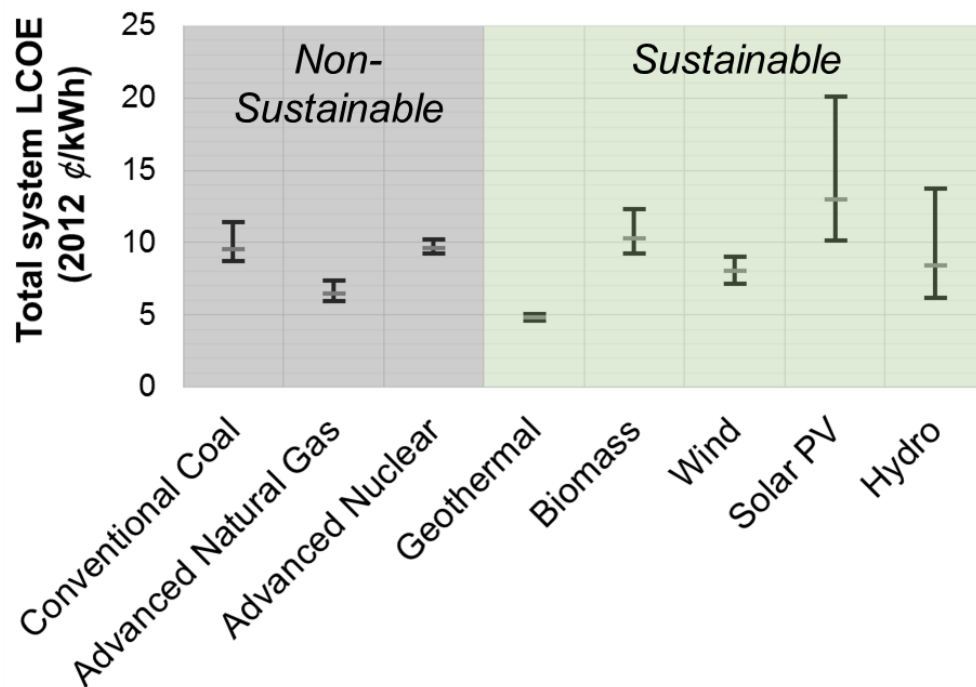


Figure 2. LCOE comparison of various energy generation methods for plants coming online in 2019 in the US. Range is regional variation and gray marks show national average. (Data from EIA).²

For PV systems, unit cost (in \$/W) is typically used instead of LCOE as the comparison metric, as it can be directly calculated without assumptions about financing, inflation, taxes, capacity factor, etc. It can be split into two parts (Fig. 3), the module and the balance of systems (BOS).⁴ BOS costs essentially include everything except the module. The main BOS cost components are

installation, inverter, financing, and permitting. In general the module and BOS costs are very much dependent on local regulations, system scale, and market conditions. The choice of technology also matters, with thin-film technologies typically being less expensive than silicon.

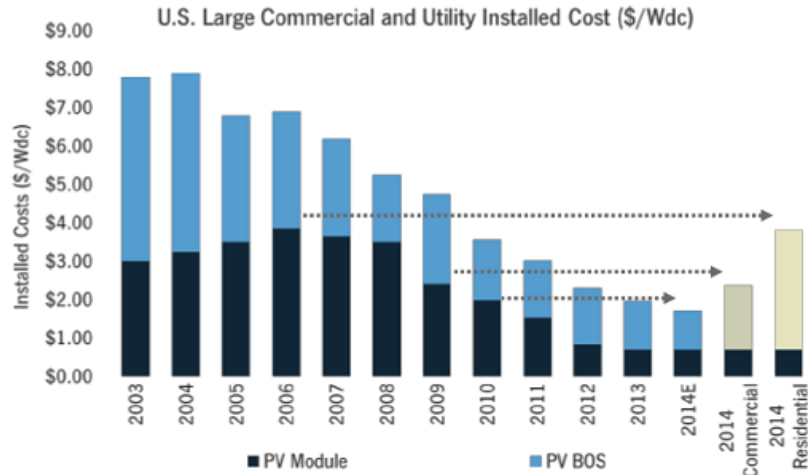


Figure 3. Total PV system costs over time showing the breakdown between balance of system and module costs. (Reproduced from GTM Research).⁴

1.1.2 Growth of the photovoltaic industry

In recent years, the photovoltaic market has grown significantly as module prices (in \$/W) have continued to come down. Growth of the cumulative global installed PV capacity has been increasing at an exponential rate with the annual deployment growing year-over-year (Fig. 4).⁴ Over half of the installed capacity has been in Europe, although rapid growth in North America and Asia since ~2010 has significantly decreased European dominance in market share.

As the cumulative production volume has gone up over the years, the module price has decreased. The relation is also known as a learning or experience curve (Fig. 5),⁴ and is commonly seen in industries that have large economies of scale. For both silicon and thin film modules this trend can be stated as a ~22% decrease in module price for a doubling in production volume.⁴ Learning curves for a given technology do not continue indefinitely, but rather asymptotically approach the cost of raw input materials.

PV market growth and cost reduction go hand in hand. As of the end of 2014, the estimated total global installed capacity was ~183 GW.^{6,7} Spot prices for both thin film and crystalline Si modules were ~\$0.60/W as of April 2015.^{8,9}

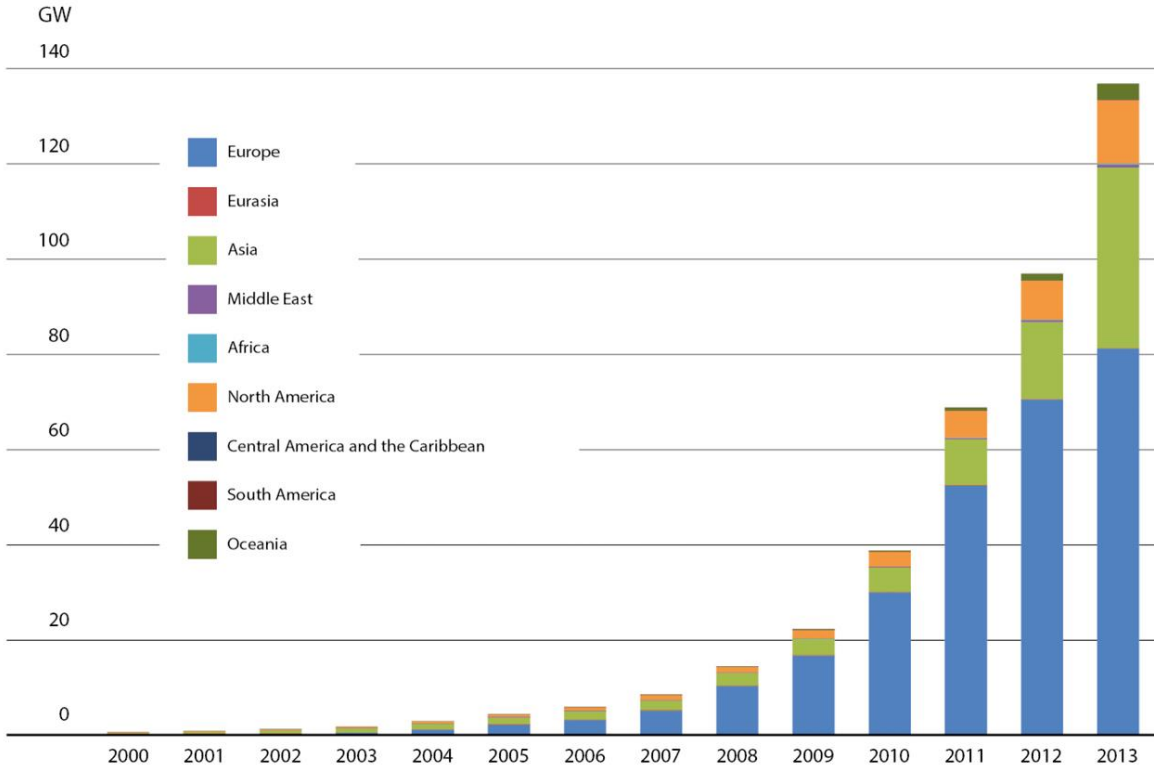


Figure 4. Cumulative worldwide PV installed capacity since 2000, broken down by region. (Reproduced from IRENA).⁵

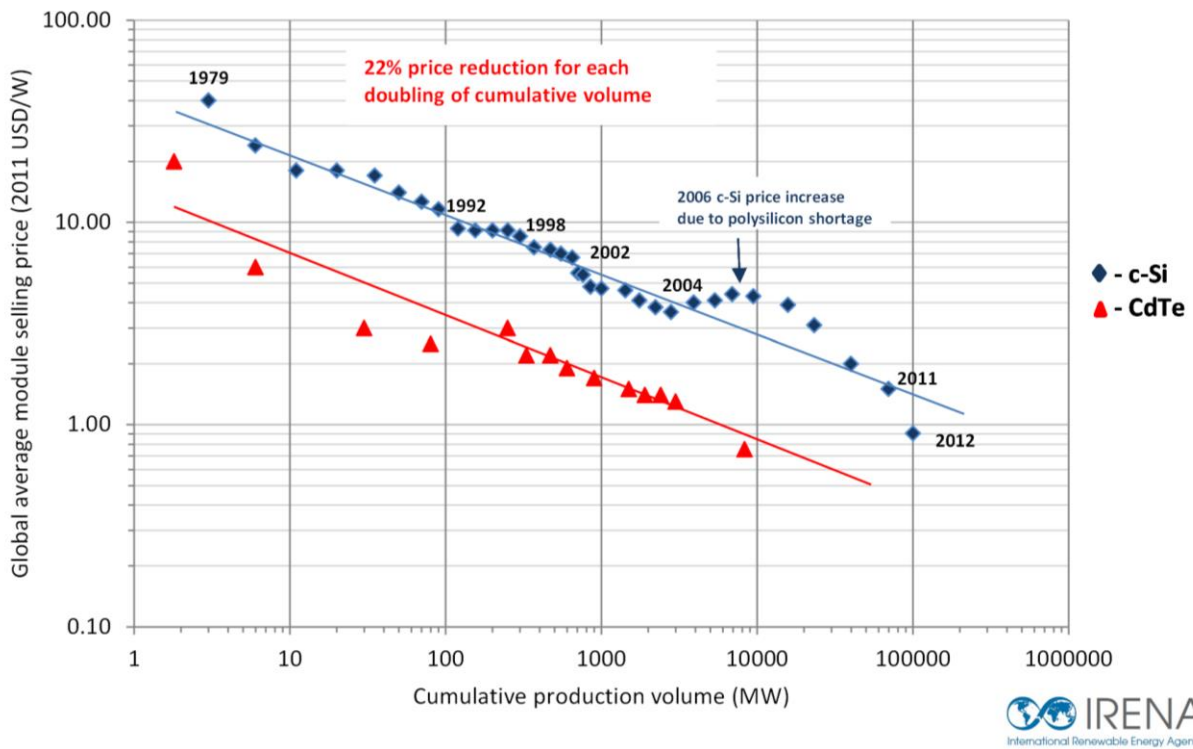


Figure 5. Learning curve for crystalline Si (c-Si) and thin film (CdTe) showing price reduction vs. cumulative production. (Reproduced from IRENA).⁵

1.1.3 Importance of efficiency

To overcome the dominance of traditional fossil fuels, the LCOE of PV cannot just match the LCOE of fossil fuels, but must be even lower to surmount switching costs, non-dispatchability, and transmission system retooling associated with large scale solar PV integration. This means PV system costs must decrease further, and so the module power conversion efficiency must increase. At the module level, the dependence on efficiency is:

$$\frac{\text{cost}}{\text{watt}} = \frac{\text{cost}/\text{m}^2}{\text{watt}/\text{m}^2} = \frac{\text{manufacturing cost}}{\text{module efficiency}}$$

The takeaway is that there is still a driving force for higher efficiencies at the same manufacturing costs in order to decrease prices. At the system level, higher efficiencies shrink the area needed for a given power output, reducing the downstream BOS costs that scale with area such as mounting frames, installation, and soft costs.

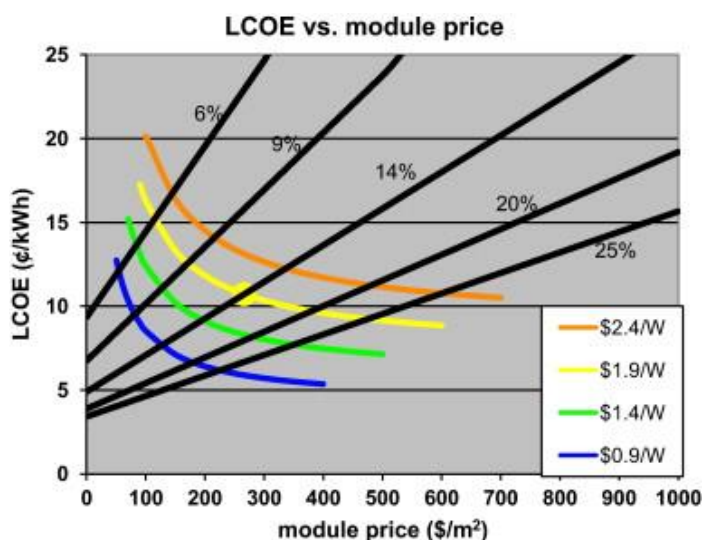


Figure 6. LCOE vs. module price for various dollars-per-watt and module efficiencies.(Reproduced from X. Wang, et. al. *Ren. and Sus. Energy Rev.* 2011).³

It is useful to examine a limiting case to see the effect of efficiency. Fig. 6 shows a plot of the relation between LCOE and module \$/m² for different module efficiencies (black lines) and \$/W (colored lines). Consider the case of the average module with 14% efficiency. Even if it were free, or cost nothing to manufacture, the total system LCOE would be ~5 ¢/kWh due to BOS costs. In contrast, a 25% efficient module could have a manufacturing cost of ~150 \$/m² and achieve the same LCOE.³

This clearly shows that the route for continued advancement in the solar industry must include high power conversion efficiency. There are many semiconductors with properties suitable for solar energy conversion, and so the choice is important. The market is dominated by Si technology, but CdTe, CIGS, organics, perovskites, and especially III-Vs have some advantages over Si.

1.2 THE CASE FOR III-V PHOTOVOLTAICS

III-V semiconductor solar cells have demonstrated the highest power conversion efficiencies to date for both single junction and multi-junctions.¹⁰ Cells and modules made from III-Vs (semiconductors composed of group III and group V elements) have the highest certified efficiencies to date (28.8% and 24.1% for systems based on single junction GaAs, respectively).¹⁰ However, the cost of III-V solar cells has historically been too high to be practical outside of specialty space applications. This stems from the cost of metalorganic precursors, expensive single crystal substrates, and slow epitaxial growth processes.¹¹ There is a need for new materials growth and fabrication techniques to bring III-V manufacturing costs down to the level of existing thin film technologies.

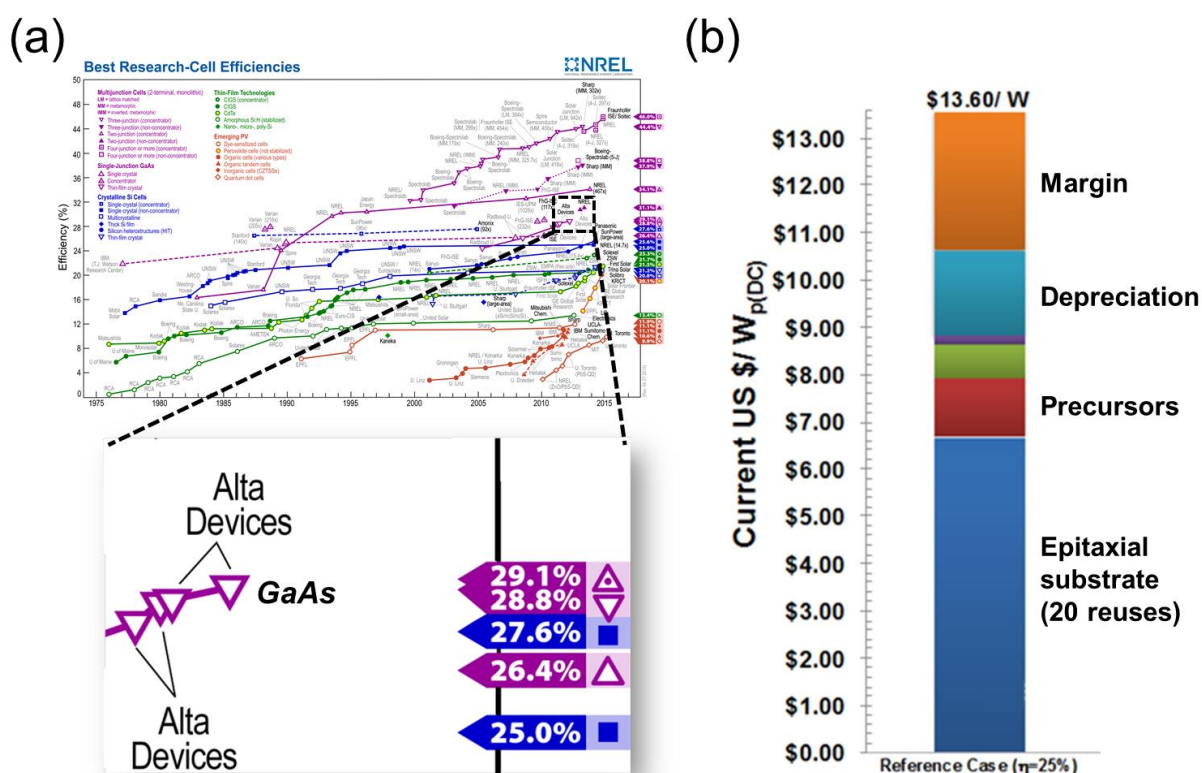


Figure 7. (a) Best research cell efficiencies over time. (Reproduced from NREL).¹² Purple lines indicate cells made using III-V semiconductors. Inset shows highest single junction efficiency of 28.8% (non-concentrator) achieved by Alta Devices using GaAs. (b) NREL cost analysis estimate of an epitaxial lift-off manufacturing process for GaAs single junction cells. (Adapted from Woodhouse and Goodrich).¹⁴

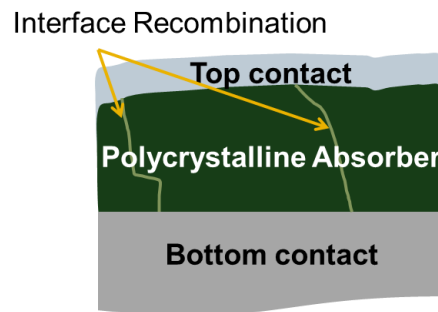
While group III elements are relatively expensive, their raw materials cost in solar cells is small due to the minute amounts needed in the absorber layer ($\sim 1 \mu\text{m}$ thickness). Viable new manufacturing techniques must exploit this fact. Along these lines, layer transfer techniques have been explored in the past where thin epitaxial films of GaAs are selectively peeled and transferred

from the growth substrate to a user-defined receiver substrate.¹³ This process enables the growth substrate to be re-used multiple times, thereby potentially lowering the manufacturing cost (Fig. 7b).¹⁴ Significant progress on this front has been made by Alta Devices.^{10,15,16}

1.3 THE ADVANTAGE OF POLYCRYSTALLINE INP

Thin film growth on non-epitaxial substrates invariably results in polycrystalline (poly) materials which presents certain constraints and challenges. In particular, the increased surface/interface area and grain boundaries may act as efficient recombination centers for photogenerated minority carriers. Thus, the use of materials with a low surface recombination velocity (SRV) is required to ensure high efficiency poly III-V solar cells (Fig. 8).

Of the III-V family, indium phosphide (InP) and gallium arsenide (GaAs) have the most ideal band gaps and highest theoretical efficiencies for single-junction cells. Untreated InP has a drastically lower SRV ($\sim 10^3 \text{ cm s}^{-1}$)¹⁷⁻²³ as compared to GaAs ($\sim 10^6 \text{ cm s}^{-1}$),^{23,24} making it an ideal candidate for efficient poly-crystalline cells. However, while poly-GaAs has been widely explored in the past,^{25,26} there have been few reports of poly-InP in terms of growth techniques,²⁷⁻²⁹ material quality,^{17,30} or device performance.^{10,31}



Material	Interface Recombination (cm/sec)	Theoretical Efficiency (%)
GaAs	10^5 - 10^6	33.5
InP	10^3-10^4	33.5

Figure 8. Schematic of solar cell with grain boundaries in the absorber and comparison of recombination velocities of GaAs and InP.

1.4 IN THIS DISSERTATION

This dissertation presents an alternative approach to epi-layer lift-off using non-epitaxial growth of poly-InP directly on low-cost metal substrates. A progression of techniques was explored for non-epitaxial InP growth, from metalorganic chemical vapor deposition (MOCVD) to close-space sublimation (CSS) to thin-film vapor-liquid-solid (TF-VLS) growth.³³⁻³⁶ To get away from expensive single crystal substrates, molybdenum (Mo) thin-films and foils are used instead. Metal foils lend themselves to low-cost roll-to-roll processing schemes, act as excellent diffusion barriers to the environment, and exhibit high thermal stability.³³ We began with MOCVD as it is the traditional technique used to grow high quality III-Vs. It grew complete thin films on Mo foils. However, it had the disadvantage of still using expensive metalorganic precursors, so CSS was tried, which used InP powder directly as the source material. The PL and lifetime properties showed an improvement over MOCVD grown films, however the grain sizes were still problematic. Finally, the TF-VLS technique was developed, which similarly used low cost precursors (elemental In and phosphine gas) and resulted in ultra-large (>500 μm) grain sizes. These TF-VLS grown films were suitable for exploration of poly-InP solar cell device performance and the manufacturing cost of InP for large-scale, high-efficiency PVs.

1.4.1 Growth on non-epitaxial substrates by MOCVD, CSS, and TF-VLS

In chapter 2, the viability of growing on Mo substrates was explored using MOCVD. These experiments answered the questions of is it possible to grow complete InP films directly on metal foils (Fig. 9), and if so what the optical qualities were. MOCVD is the traditional technique for growing high-quality III-Vs, and was used as a benchmark technique for what is possible. The grown InP films are 1-3 microns thick and are composed of micron-sized grains that generally extend from the surface to the Mo substrate. They exhibit similar photoluminescence peak widths and positions as single-crystalline InP, as well as excellent crystallinity as examined through TEM and XRD analysis.³³

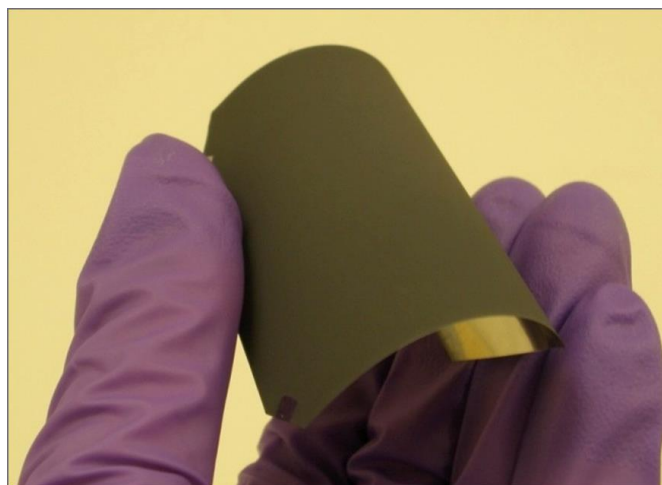


Figure 9. InP thin film grown on flexible Mo foil using MOCVD.³³

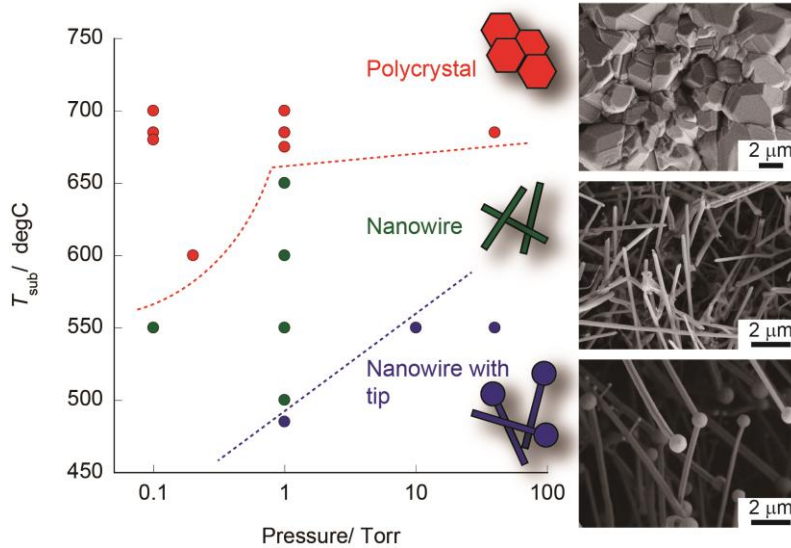


Figure 10. Temperature (T_{sub})–pressure (P) dependence of InP morphologies grown by CSS. The SEM images from top to bottom are as follows: polycrystalline film, nanowires, and nanowires with In-rich tips.³⁴

Chapter 3 discusses the use of close-space sublimation (CSS) for InP growth on Mo foils. CSS or its derivatives are the principal method for growing CdTe. This technique represents an improvement over MOCVD as it uses InP directly as the source instead of metalorganic precursors. CSS allows effective transfer of source material to the substrate due to a small (~ 2 mm gap between source and substrate) sublimation space. The crystallization was found to be dependent on the substrate temperature and pressure of the system. Importantly, experiments revealed that both InP nanowires and polycrystalline films could be obtained by tuning the growth conditions (Fig. 10). Furthermore, utilizing a silicon dioxide mask, selective nucleation of InP on metal substrates was obtained. Photoluminescence measurements show the high optical quality of the CSS grown InP.³⁴

The third growth technique introduced in chapter 4 is TF-VLS growth (Fig. 11), created by Kapadia and Yu.^{35,36} This technique was the one used for subsequent solar cell devices and manufacturing cost analysis. TF-VLS growth produces high optoelectronic quality InP absorber layers directly on molybdenum (Mo) substrates. In this implementation of the technique, a layer of In confined between a Mo substrate and silica (SiO_x) cap is heated to a temperature where the In is a liquid. Then, a phosphorus vapor is introduced and diffuses through the SiO_x into the In

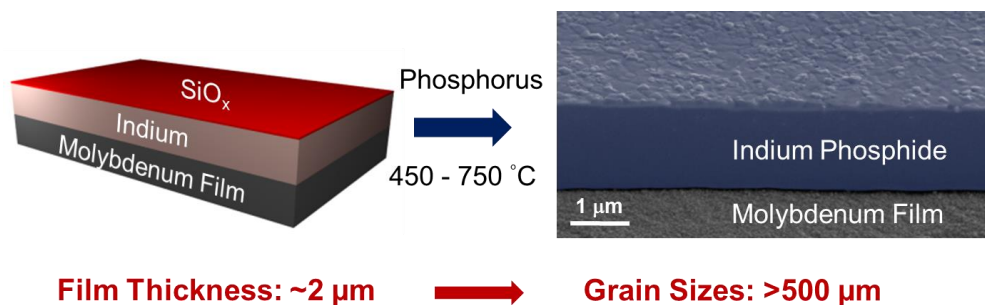


Figure 11. TF-VLS growth process for InP.

liquid, causing precipitation of solid InP. The InP grows into a polycrystalline film with large ($>100\ \mu\text{m}$) lateral grain sizes.^{35,36} The benefits of TF-VLS growth over traditional metalorganic chemical vapor deposition (MOCVD) growth are high throughput, high materials utilization efficiency, and non-epitaxial substrates.

1.4.2 InP solar cell devices

The design and performance of a solar cell based on InP grown non-epitaxially by the thin-film vapor-liquid-solid (TF-VLS) growth technique is investigated in chapter 4. The cell structure is composed of a Mo back contact, *p*-InP absorber layer, *n*-TiO₂ electron selective contact, and ITO transparent top electrode (Fig. 12). An *ex-situ* *p*-doping process for TF-VLS grown InP is introduced. Properties of the cells such as optoelectronic uniformity and electrical behavior of grain boundaries are examined. The power conversion efficiency of the first generation cells reaches 12.1% under simulated 1 sun illumination with open circuit voltage (V_{OC}) of 692 mV, short circuit current (J_{SC}) of 26.9 mA/cm², and fill factor (FF) of 65%. The FF of the cell is limited by the series resistances in the device, including the top contact, that can be mitigated in the future through device optimization. Notably, the highest measured V_{OC} under 1 sun was 692 mV which is close to the optically implied V_{OC} of $\sim 795\ \text{mV}$ as extracted from luminescence yield for *p*-InP.

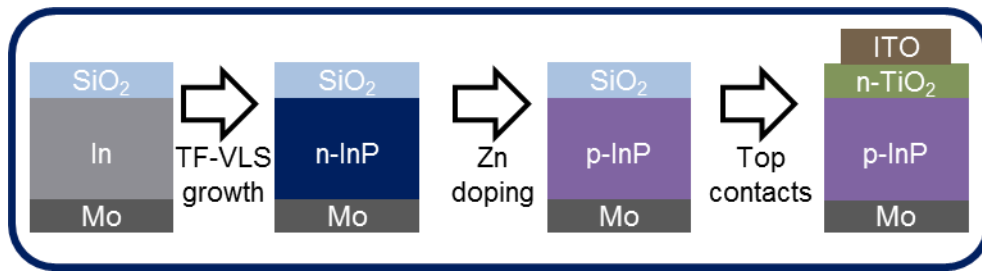


Figure 12. Process flow for producing *n*-TiO₂/*p*-InP solar cells.

1.4.3 Manufacturing cost analysis

Chapter 5 presents a manufacturing cost analysis for producing thin-film indium phosphide (InP) modules by combining a novel thin-film vapor-liquid-solid (TF-VLS) growth process with a standard monolithic module platform (Fig. 13). The example cell structure is ITO/*n*-TiO₂/*p*-InP/Mo. For a benchmark scenario of 12% efficient modules, the module cost is estimated to be $\$0.78/W_{p(DC)}$ and the module cost is calculated to be around $\$0.40/W_{p(DC)}$ at a long-term potential efficiency of 24%. The manufacturing cost for the TF-VLS growth portion is estimated to be $\$31/m^2$, a significant reduction compared to traditional metalorganic chemical vapor deposition (MOCVD). The analysis here suggests the TF-VLS growth mode could enable lower-cost, high-

efficiency III-V photovoltaics compared to manufacturing methods used today and open up possibilities for other optoelectronic applications as well.

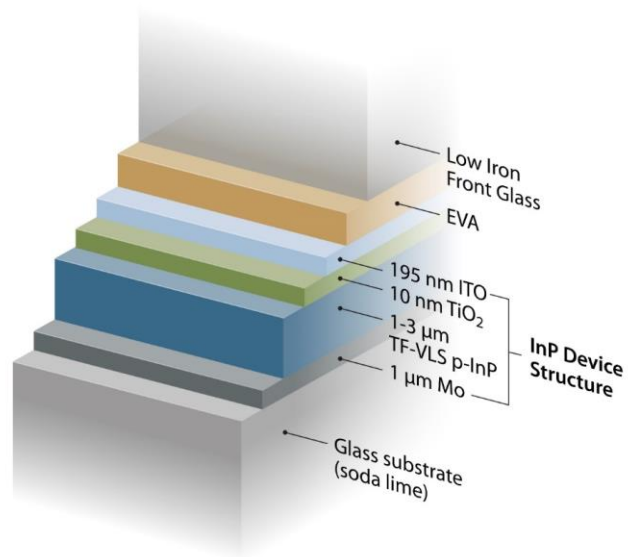


Figure 13. Schematic of proposed module for cost analysis of manufacturing TF-VLS InP modules .

REFERENCES

1. Perez, R. and M. Perez, (2009): A fundamental look at energy reserves for the planet. <http://www.asrc.cestm.albany.edu/perez/Kit/pdf/a-fundamental-look-at%20the-planetary-energy-reserves.pdf>
2. U.S. Energy Information Administration. Levelized Cost and Levelized Avoided Cost of New Generation Resources in the Annual Energy Outlook 2014. http://www.eia.gov/forecasts/aeo/electricity_generation.cfm
3. X. Wang, L. Kurdgelashvili, J. Byrne and A. Barnett, *Renewable and Sustainable Energy Reviews*, 2011, **15**, 4248–4254.
4. <http://www.greentechmedia.com/articles/read/Its-Solar-Balance-of-System-Innovation-That-Will-Drive-Cost-Reduction>
5. International Renewable Energy Agency. Renewable Power Generation Costs in 2014. http://www.irena.org/DocumentDownloads/Publications/IRENA_RE_Power_Costs_2014_report.pdf
6. http://en.wikipedia.org/wiki/Growth_of_photovoltaics
7. <http://www.solarnews.es/2015/03/31/global-solar-installations-to-grow-by-30-to-reach-57-gw-in-2015/>
8. <http://pv.energytrend.com/>
9. http://www.pv-tech.org/news/has_first_solar_retaken_the_lowest_cost_pv_manufacturer_mantle
10. M. A. Green, K. Emery, Y. Hishikawa, W. Warta and E. D. Dunlop, *Prog. Photovolt: Res. Appl.*, 2015, **23**, 1–9.
11. M. Bosi and C. Pelosi, *Progress in Photovoltaics: Research and Applications*, 2007, **15**, 51–68.
12. http://www.nrel.gov/ncpv/images/efficiency_chart.jpg
13. X. Y. Lee, A. K. Verma, C. Q. Wu, M. Goertemiller, E. Yablonovitch, J. Eldredge and D. Lillington, in *Conference Record of the Twenty Fifth IEEE Photovoltaic Specialists Conference, 1996*, IEEE, 1996, pp. 53–55.
14. M. Woodhouse, A. Goodrich. Manufacturing Cost Analysis Relevant to Single-and Dual-Junction Photovoltaic Cells Fabricated with III-Vs and III-Vs Grown on Czochralski Silicon. National Renewable Energy Laboratory 2014. <http://www.nrel.gov/docs/fy14osti/60126.pdf>
15. B. M. Kayes, H. Nie, R. Twist, S. G. Spruytte, F. Reinhardt, I. C. Kizilyalli and G. S. Hignashi, in 2011 37th IEEE Phot. Spec. Conf. (PVSC), 2011, pp. 000004–000008.
16. L. S. Mattos, S. R. Scully, M. Syfu, E. Olson, L. Yang, C. Ling, B. M. Kayes and G. He, in 2012 38th IEEE Phot. Spec. Conf. (PVSC), 2012, pp. 003187–003190.
17. T. Nakamura and T. Katoda, *Journal of Applied Physics*, 1984, **55**, 3064–3067.
18. Y. Rosenwaks, Y. Shapira and D. Huppert, *Phys. Rev. B*, 1991, **44**, 13097–13100.

19. R. K. Ahrenkiel, D. J. Dunlavy and T. Hanak, *Journal of Applied Physics*, 1988, **64**, 1916–1921.
20. R. K. Ahrenkiel, D. J. Dunlavy and T. Hanak, *Solar Cells*, 1988, **24**, 339–352.
21. Y. Rosenwaks, Y. Shapira and D. Huppert, *Phys. Rev. B*, 1992, **45**, 9108–9119.
22. S. Bothra, S. Tyagi, S. K. Ghandhi and J. M. Borrego, *Solid-State Electronics*, 1991, **34**, 47–50.
23. D. D. Nolte, *Solid-State Electronics*, 1990, **33**, 295–298.
24. L. Jastrzebski, J. Lagowski and H. C. Gatos, *Applied Physics Letters*, 1975, **27**, 537–539.
25. R. Venkatasubramanian, B. C. O’Quinn, J. S. Hills, P. R. Sharps, M. L. Timmons, J. A. Hutchby, H. Field, R. Ahrenkiel and B. Keyes, in *Conference Record of the Twenty Fifth IEEE Photovoltaic Specialists Conference, 1996*, IEEE, 1996, pp. 31–36.
26. Y. C. M. Yeh and R. J. Stirn, *Applied Physics Letters*, 1978, **33**, 401.
27. T. Saitoh, S. Matsubara and S. Minagawa, *Thin Solid Films*, 1978, **48**, 339–344.
28. T. Saitoh, S. Matsubara and S. Minagawa, *Japanese Journal of Applied Physics*, 1976, **15**, 893–894.
29. T. Saitoh, S. Matsubara and S. Minagawa, *J. Electrochem. Soc.*, 1976, **123**, 403–406.
30. T. Saitoh and S. Matsubara, *J. Electrochem. Soc.*, 1977, **124**, 1065–1069.
31. T. Saitoh, S. Matsubara and S. Minagawa, *Japanese Journal of Applied Physics*, 1977, **16**, 807–812.
32. K. J. Bachmann, E. Buehler, J. L. Shay and S. Wagner, *Applied Physics Letters*, 1976, **29**, 121.
33. M. Zheng, Z. Yu, T. J. Seok, Y.-Z. Chen, R. Kapadia, K. Takei, S. Aloni, J. W. Ager, M. Wu, Y.-L. Chueh and A. Javey, *J. Applied Physics*, 2012, **111**, 123112.
34. D. Kiriya, M. Zheng, R. Kapadia, J. Zhang, M. Hettick, Z. Yu, K. Takei, H.-H. Hank Wang, P. Lobaccaro and A. Javey, *Journal of Applied Physics*, 2012, **112**, 123102–123102–6.
35. R. Kapadia, Z. Yu, H.-H. H. Wang, M. Zheng, C. Battaglia, M. Hettick, D. Kiriya, K. Takei, P. Lobaccaro, J. W. Beeman, J. W. Ager, R. Maboudian, D. C. Chrzan and A. Javey, *Sci. Rep.*, 2013, **3**, 2275.
36. R. Kapadia, Z. Yu, M. Hettick, J. Xu, M. S. Zheng, C.-Y. Chen, A. D. Balan, D. C. Chrzan and A. Javey, *Chem. Mater.*, 2014, **26**, 1340–1344.

CHAPTER 2

POLYCRYSTALLINE INP GROWN BY MOCVD*

2.1 INTRODUCTION

Here we report on high optical quality poly-InP thin films grown on molybdenum thin film and foil substrates, by metalorganic chemical vapor deposition (MOCVD). The materials and optical characteristics of the grown films are systematically explored as a function of growth conditions. Poly-InP films grown at the optimal temperature exhibit highly promising properties with the photoluminescence spectra closely matching that of a single-crystalline InP. Crystal quality was evaluated as the absence of defects and dislocations, as well as grain size and XRD line width.

2.2 EXPERIMENTAL DETAILS

2.2.1 MOCVD Growth

The MOCVD system used was a Thomas Swann 3x2 CCS MOCVD. The chamber was a vertical cold-wall showerhead configuration. The susceptor held 3" wafers and the rotation rate was fixed at 30 RPM. The precursors were Trimethylindium (TMIn) from Akzo Nobel and Tert-butylphosphine (TBP) from Dockweiler Chemicals. They were held at 20 °C and 10 °C, respectively. TMIn was flowed at $\sim 1.2\text{E-}5$ mol/min and TBP at $\sim 2.4\text{E-}3$ mol/min, giving a [V]/[III] molar ratio of ~ 200 . Total flow of H₂ and precursors was 11.5 L/min. Growth temperatures ranged from 445 °C to 545 °C. Growth times explored were 5-75 minutes, with 75 minutes used for the data in this paper. The chamber pressure was fixed at 76 Torr.

* This chapter has been published in similar form as Zheng, *et al. Journal of Applied Physics* 2012, **111**, 123112. Permission has been granted to include it here.

2.2.2 Characterization

SEM images were taken on a Zeiss Gemini Ultra-55. TEM was performed using a JEOL-3000F. The XRD was taken on a Bruker AXS D8 Discover GADDS XRD Diffractometer system. The PL excitation source was a 785 nm laser with ~ 30 μm spot size, and the detector was a silicon CCD. Note that at this excitation, the penetration depth is ~ 290 nm, so carriers are being generated mainly in the top quarter of the films. The reference InP sample was (100) orientation n-type doped with zinc to $\sim 10^{17}/\text{cm}^3$. The excitation source for the backscatter Raman data was the 488 nm line from an Ar ion laser. The uncertainty of the Raman data is limited to ± 0.3 cm^{-1} .

2.3 RESULTS AND DISCUSSION

2.3.1 Choice of Substrate

The choice of substrate metal is critical for obtaining high quality poly-InP films. At the growth temperature, it should have low solubility of both indium and phosphorus. Ideally, it should either not form indium alloys or metal phosphides, or if it does, the reaction should be self-limiting. In addition, it should have a similar thermal expansion coefficient as InP.¹ From metal-P and metal-In phase diagrams, Mo and W meet the above criteria the best. For Mo in particular, there are no intermetallics at the growth temperature, and the solubility of In is very low. There are few Mo-P compounds, and no solid solutions; this suggests the loss of phosphorous into the substrate will be minimal. Here, we have chosen to focus on Mo, both in the form of thin foils and thin films. The Mo foils used were 25 μm thick and cleaned with acetone and isopropanol prior to growth. In parallel, Si/SiO₂ (thermal oxide, 50 nm thickness) handling wafers with a sputtered Cr (5 nm thickness) adhesion layer and Mo (50 nm thickness) top film were explored as a growth substrate. Subsequently, InP thin films were grown on top of these Mo substrates by MOCVD as schematically illustrated in Figure 1a. Optical images of InP thin films (~ 2 μm thickness) grown on flexible Mo foil and sputtered Mo thin film substrates (510 °C and 75 minutes) are shown in Figures. 1b and 1c, respectively. Thus far, we have grown uniform films over ~ 40 cm^2 foils and 3" diameter wafers, limited only by the sample holder size of the MOCVD equipment used in this study. As evident from visual inspection, the grown InP films exhibit large area uniformity and continuity. In general, the growth properties were found to be similar between the two types of substrates. Thus, from here on we primarily present the growth data on the Mo thin film substrate.

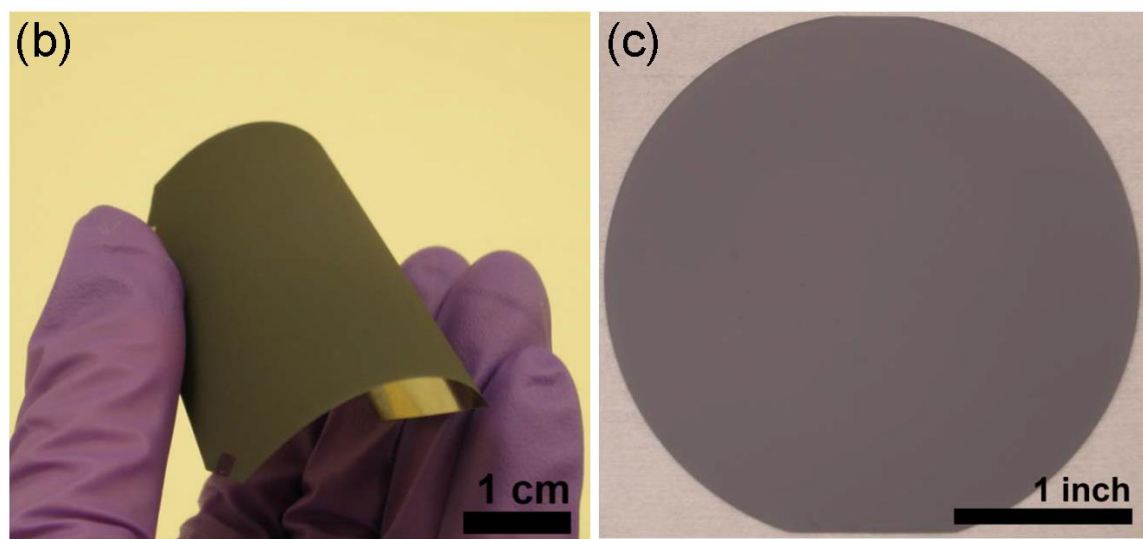
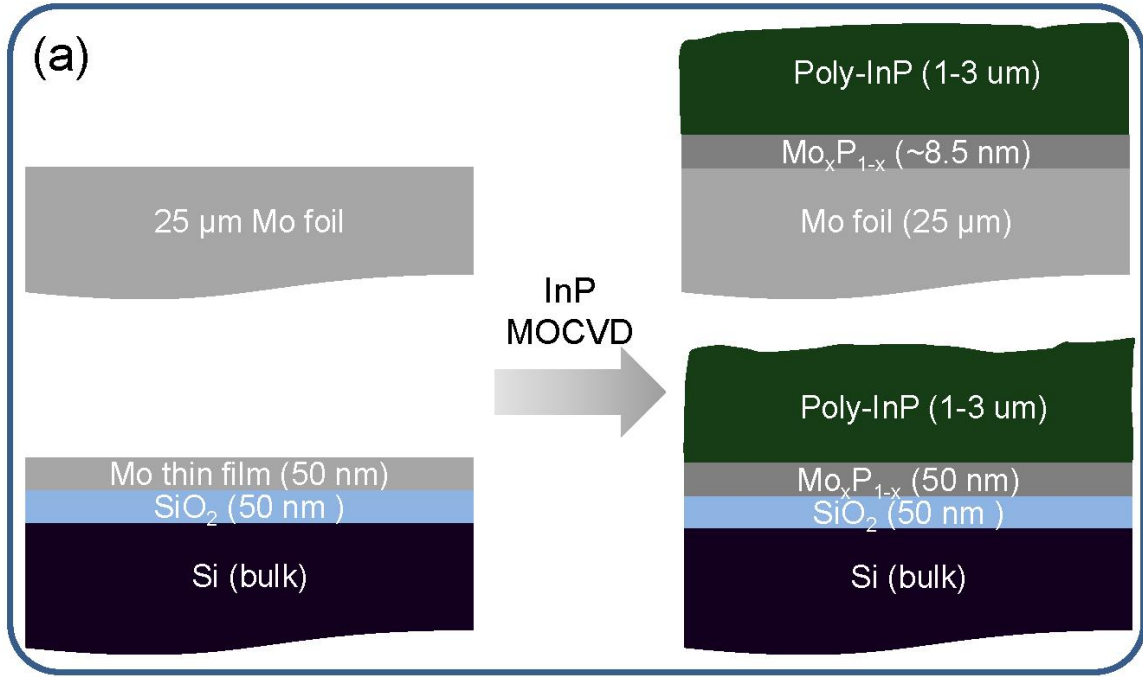


Figure 1. (a) Poly-InP fabrication scheme. (b) Poly-InP on flexible molybdenum foil. (c) Poly-InP on sputtered Mo on 3" wafer. Lighter ring is due to edge effects from the susceptor.

2.3.2 SEM/TEM

In this work, we primarily focus on the effects of growth time and temperature. Figures 2a,b show top-and side-view SEM images of a representative InP thin film ($\sim 3 \mu\text{m}$ thickness) grown on a Mo thin film. The growth temperature and time were $520 \text{ }^\circ\text{C}$ and 75 min, respectively, which were optimal given the opposing constraints of surface coverage and crystal quality. The grown InP films are poly-crystalline and continuous (Figure 2a,b). The grains generally extend from the surface to the substrate, but are oriented randomly. The average grain size and surface roughness of the thin film for this growth condition are $\sim 2 \mu\text{m}$ and $\sim 200 \text{ nm}$, respectively – both of which highly depend on the growth temperature.

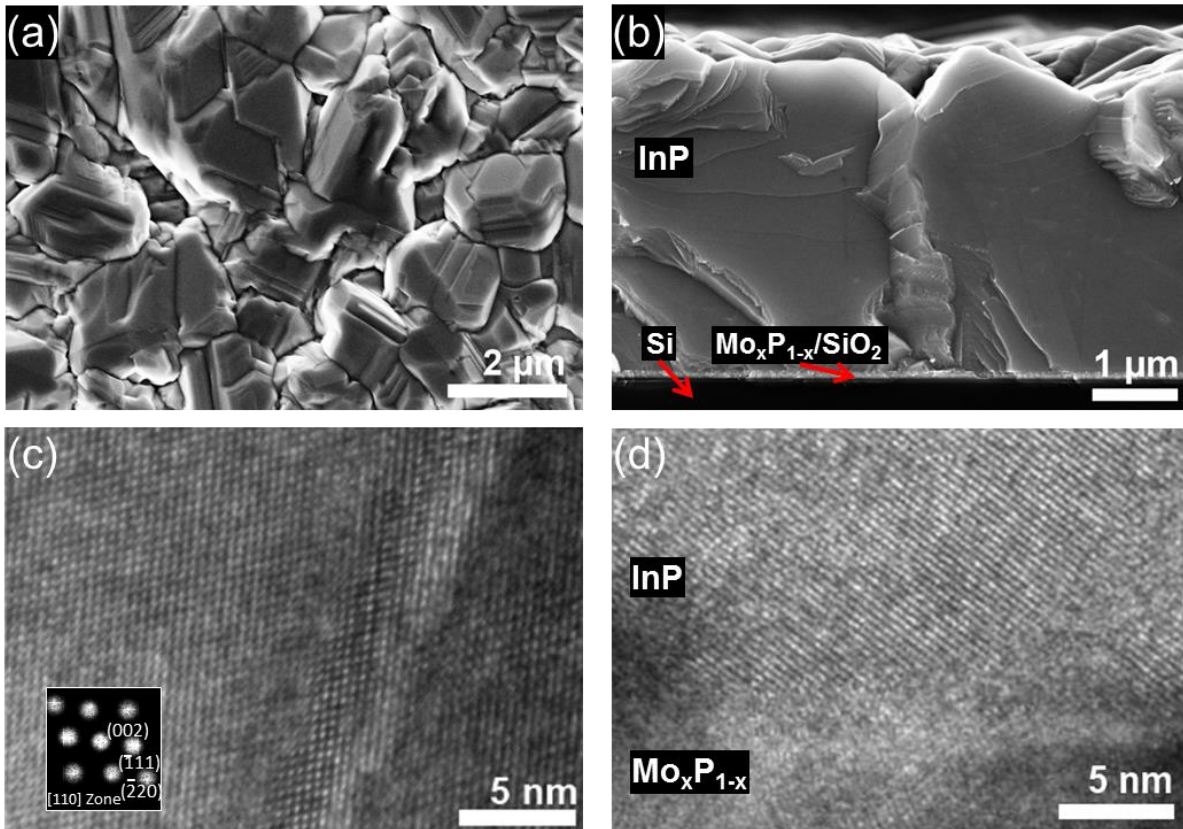


Figure 2. (a) SEM top view of poly-InP grown at $520 \text{ }^\circ\text{C}$ for 75 minutes. (b) Cross-sectional SEM image of poly-InP grown on a Mo thin film at $520 \text{ }^\circ\text{C}$ for 75 minutes. The InP is on top of $\sim 50 \text{ nm}$ $\text{Mo}_x\text{P}_{1-x}/50 \text{ nm}$ SiO_2/Si . (c) TEM image at a grain boundary. Inset shows FFT from within the left grain. (d) TEM of interface between InP and Mo/ $\text{Mo}_x\text{P}_{1-x}$.

From SEM and TEM analyses, the grain sizes range from $\sim 0.5 \mu\text{m}$ for $445 \text{ }^\circ\text{C}$ growth temperature to $\sim 10 \mu\text{m}$ for $545 \text{ }^\circ\text{C}$ (Figure 3). While the grain size increases with temperature, the grown InP is not continuous at $\geq 545 \text{ }^\circ\text{C}$ for a fixed growth time of 75 min. Higher substrate temperatures increase the desorption rate of precursors from the substrate, which causes a reduced number of nucleation sites. In addition, the existing nucleation sites grow and deplete the local environment

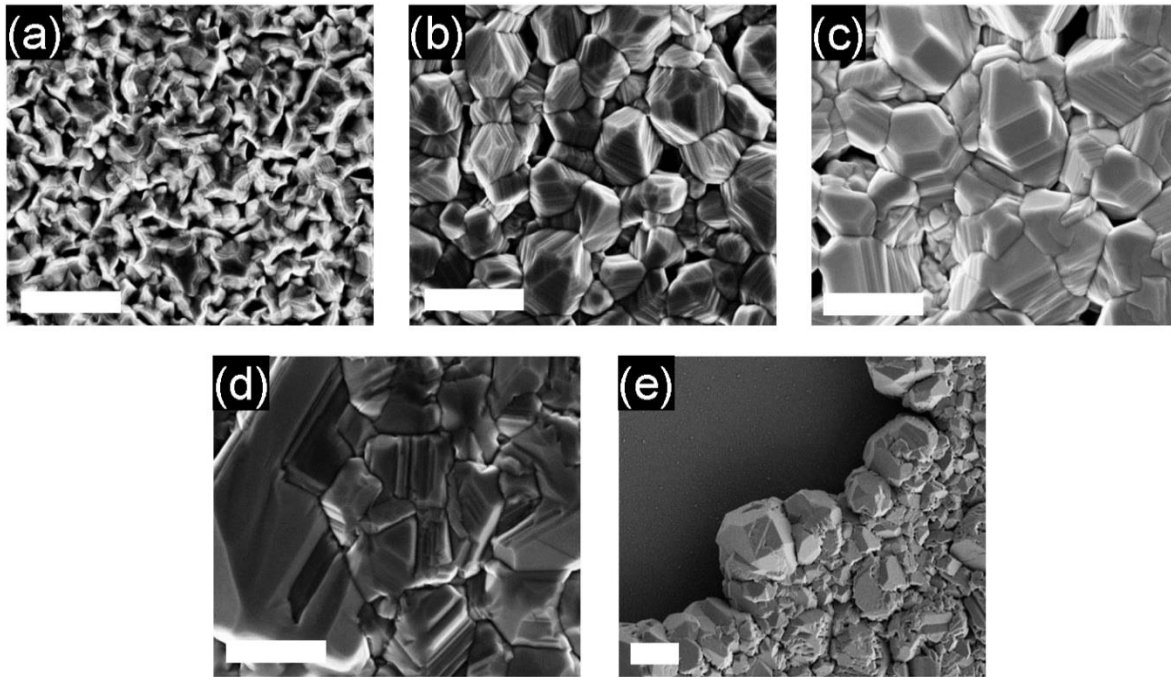


Figure 3. Growth temperature series showing increasing grain size with growth temperature. Samples shown are all grown on sputtered Mo thin films. (a) 445 °C. (b) 480 °C. (c) 500 °C. (d) 520 °C. (e) 545 °C. Scale bars in (a-d) are 2 μm , scale bar in (e) is 10 μm .

of precursors at the expense of additional nucleation, which results in a discontinuous film. At growth temperatures of ≤ 500 °C, striations are clearly present within each grain oriented parallel to the substrate based on SEM inspection (Figure 4). From TEM analysis, the striations correspond to stacking faults (Figure 4). Each layer appears to consist of ~ 10 -100 close packed planes. Similar stacking faults and twinning have been observed in metalorganic vapor phase epitaxy grown InP nanowires in the [111] direction.^{2,3} The data is also consistent with the known low stacking fault energy of InP.⁴ However, at growth temperatures of ≥ 520 °C, the density of stacking faults are drastically reduced with only a minimal number of such defects being evident in TEM analysis (Figure 2c). The appearance of stacking faults suggests the growth mechanism after nucleation is layer-by-layer of close packed planes ([111] direction in a zincblende lattice). This is similar to the traditional growth of epitaxial layers, where the underlying substrate is cut slightly off axis to facilitate layer-by-layer growth at terraces. Altogether, crystal quality appears to be higher at higher growth temperatures. Considering both crystal quality and film continuity constraints, 520 °C is found to be the optimal growth temperature for a fixed growth time of 75 minutes.

Further, TEM study indicates the interface between InP and Mo is continuous and free of voids, as seen in Figure 2d. Composition analysis reveals significant phosphorus content throughout the initial 50 nm Mo layer. It appears to be composed of a mixture of Mo and $\text{Mo}_x\text{P}_{1-x}$ phases, where x ranges from ~ 0.8 to ~ 0.5 from low to high growth temperatures as confirmed by EDS/TEM analysis. In contrast, InP on Mo foil samples showed a similar $\text{Mo}_x\text{P}_{1-x}$ layer, where x ranged from ~ 0.6 to ~ 0.4 . However, this layer was self-limited to a thickness of only ~ 8.5 nm (Figure 5). This is attributed to the larger grain sizes of the foil vs. the sputtered Mo, and corresponding lower

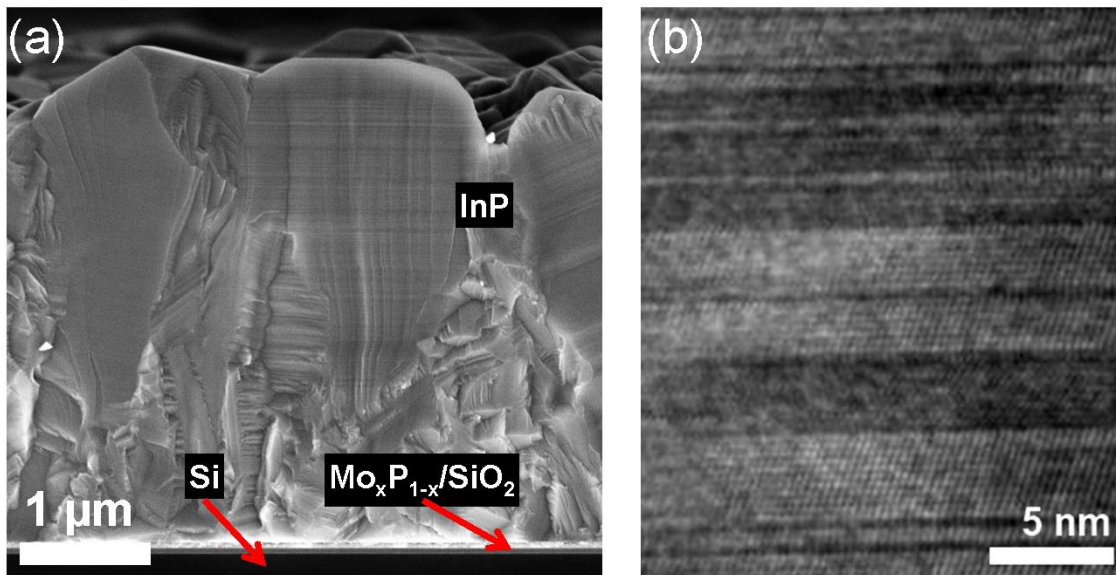


Figure 4. (a) Side view SEM image of sample grown on a Mo thin film at 500 °C for 75 minutes. A grain without striations (left) is shown next to two with horizontal striations (right). (b) TEM image of same sample showing stacking faults.

reactivity. Close examination reveals that in some locations, the InP lattice matches that of the underlying Mo_xP_{1-x}, suggesting a high quality interface. Note that in contrast to the results here, Ni foil substrates in the same growth conditions showed uncontrollable reactions with phosphorus

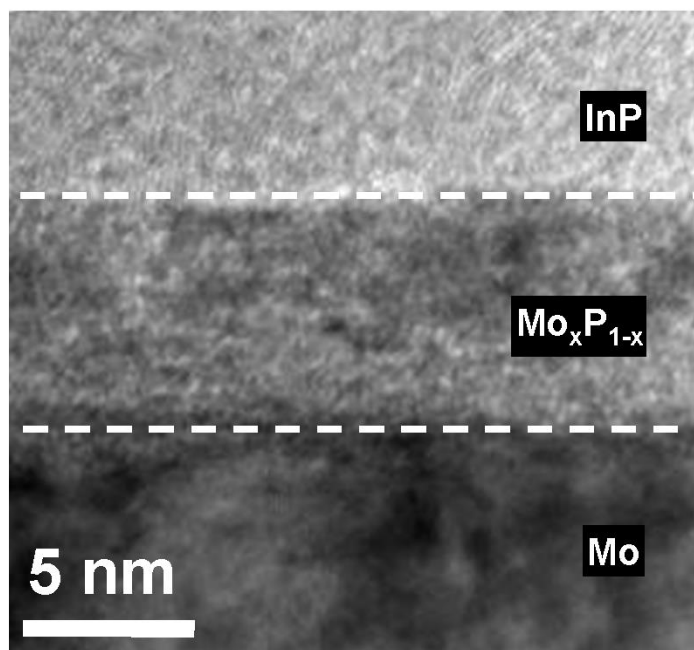


Figure 5. TEM image of the ~8.5 nm transition layer of Mo_xP_{1-x} between InP (top) and Mo foil (bottom).

and indium. This is consistent with presence of solid solutions at the growth temperatures in the In-Ni and Ni-P phase diagrams. The surface of the foils becomes pitted and cracked and no InP film was able to grow.

2.3.3 XRD

The grown InP films were characterized by XRD (Figure 6). The XRD analysis further shows texture at lower growth temperatures, with only the (111) and (222) peaks noticeable. The peak positions match those of zincblende InP.^{5,6} As the growth temperature increases, additional peaks appear, indicating the grains become more randomly oriented. This implies that at lower growth temperatures there is a preferential orientation for nucleation sites, and at higher temperatures there is not. Growth after nucleation naturally follows the orientation of the nuclei. At the highest growth temperature of 545 °C, the relative peak intensities are a close match to the ICDD powder reference.⁶ In addition, the line widths of the (220) and (311) peaks get progressively narrower as growth temperature increases, indicating a greater level of crystallinity. There is no evidence of wurtzite InP peaks,⁵ especially the (0002) peak which would show up close to (111) zincblende peak, indicating that the stacking faults do not result in a phase change from zincblende to wurtzite.

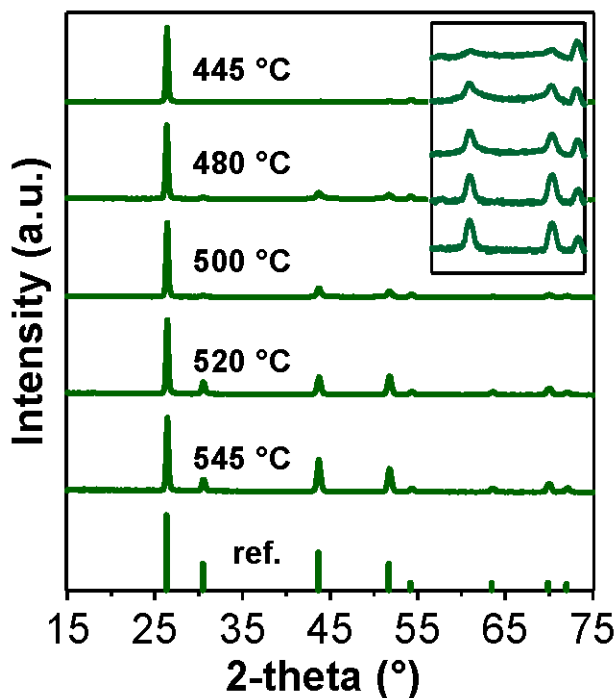


Figure 6. XRD spectra as a function of growth temperature. Curves are normalized to the (111) peak and offset. Inset, log scale, shows the gradual narrowing of the (220) and (311) peaks. Reference data are from the ICDD PDF. From left to right the first five peaks are: (111), (200), (220), (311), and (222).

2.3.4 Raman

Raman spectra (Figure 7) for films grown at all temperatures (445 °C – 545 °C) match well with that reported in the literature for a single-crystalline InP substrate.⁷⁻⁹ The first order anti-Stokes Γ TO and Γ LO peaks show up at $\sim 303 \text{ cm}^{-1}$ and $\sim 344 \text{ cm}^{-1}$ respectively. The data are all normalized to the Γ TO peak intensity. The relative intensity of the Γ LO peak increases slightly with growth temperature. In addition, the Γ LO peak shows a pronounced asymmetry towards lower energy. Second order features corresponding to the XLO + XTO, 2Γ TO, and Γ LO + Γ TO interactions also appeared.^{7,9} Of these, only the XLO + XTO feature intensity showed a strong correlation with growth temperature, which may be related to the stacking fault density. While the intensity increases with growth temperature, the shape remains unchanged. From the zincblende symmetry selection rules, the LO phonon peak appears if the surface is (100) or (111), while the TO phonon peak appears if the surface is (110) or (111). The presence of both peaks is consistent with the (111) texture seen at lower growth temperatures and the randomly oriented grains at higher growth temperatures. There are no indications of stress in the films as indicated by peak positions.

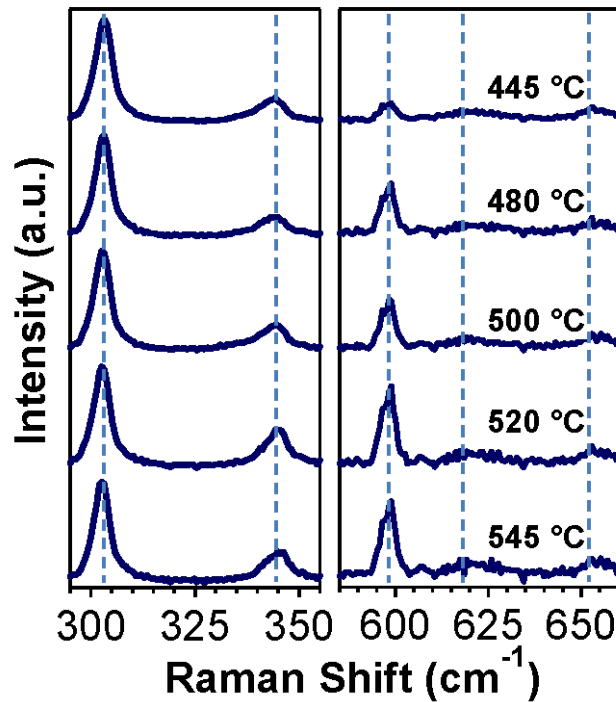


Figure 7. Room temperature Raman. Data is normalized to the Γ TO peak and offset. The left graph shows the first order peaks, Γ TO and Γ LO, from left to right. The right graph shows second order peaks, XLO + XTO, 2Γ TO, and Γ LO + Γ TO, from left to right. Intensity of data in right graph is 5x.

2.3.5 Photoluminescence

Room temperature micro-PL data also shows a clear trend of increasing quality with growth temperature (Figure 8). As a metric, we compare our poly-InP PL spectra to a non-degenerately doped single crystal InP reference, as well as previously reported values in the literature. At the two highest growth temperatures (520 °C and 545 °C), the peak position, full-width-at-half-maximum (FWHM), and shape are nearly identical to a single-crystal reference sample. Although the level of unintentional doping is unknown, this is evidence that the optical qualities of poly-InP are comparable to single crystal InP. At lower growth temperatures, the spectra are blue-shifted, FWHM is broad, and the shape is symmetric. The trend is summarized in Table 1. Note that the 520 °C and 545 °C peaks at ~922 nm correspond to the direct band gap energy of ~1.34 eV,^{10,11} matching closely the expected band-gap of InP, whereas the 445 °C peak at ~898.5 nm corresponds to ~1.38 eV. Such blue-shifts have been observed for InP nanowires with stacking faults, and have been attributed to the presence of the wurtzite phase or quantum confinement, both of which increase the band gap.^{2,12} While there is clearly a correlation between stacking fault prevalence due to growth temperature and PL characteristics in our InP, the SEM and XRD data do not indicate the presence of a wurtzite phase.

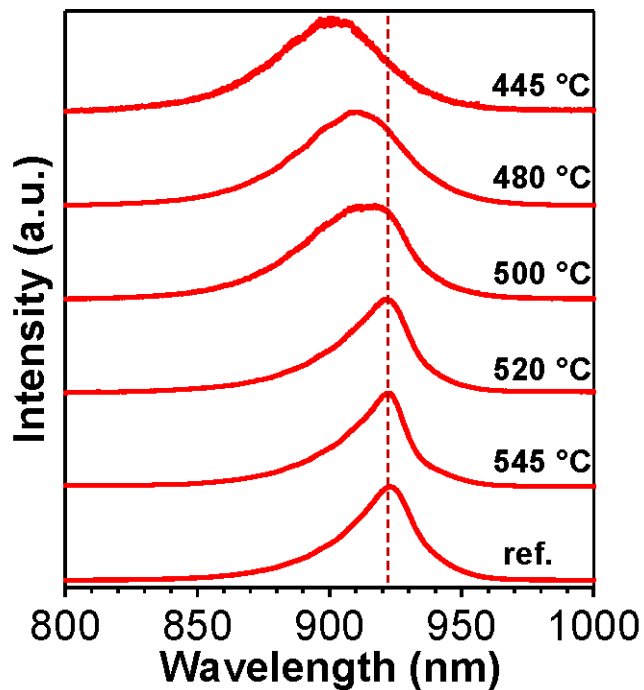


Figure 8. Room temperature PL change with growth temperature. Higher growth temperatures exhibit near identical shape and position as a single crystal reference. Curves are normalized and offset.

Also important to note is that the PL feature from the 500 °C sample is plainly composed of two overlapping peaks, as can be seen by the asymmetry and flat top. Moreover, the relative intensities of the two contributions varied as the sample was scanned laterally (not shown). This is consistent

with the SEM/TEM analyses, which shows grains with stacking faults next to those without such defects. There is also a clear transition temperature between 500 °C and 520 °C where the optical transitions corresponding to the higher energy peak are totally suppressed, leaving only the peak corresponding to bulk zincblende InP. This possibly corresponds to the elimination of stacking faults. There is a strong correlation between the presence of stacking faults and the higher energy PL feature. However, without conclusive evidence and a satisfactory model for this hypothesis, we cannot establish a causal relationship. The possibility of other defects introduced at low growth temperatures cannot be ruled out as the source of the PL trend. Based on the PL characteristics, the optimal growth temperature is 520 °C. At this growth temperature, there are no PL features remaining that do not appear in the single crystal reference.

Growth temperature (°C)	Peak Position (nm)	FWHM (nm)
445	898.5	46
480	908.8	46
500	917.0	45
520	921.6	30
545	922.4	26
Ref [a]	923.4	28

[a] Single crystal sample

Table 1. PL peak positions and FWHMs as a function of growth temperature.

2.4 CONCLUSIONS

To summarize, we have demonstrated high optical quality InP grown on metal substrates. The resulting films are composed of micron-sized grains, and importantly show nearly identical PL and Raman spectral shape and position as those of a single-crystal reference. In the future, further characterization of the minority carrier lifetime, mobility, and diffusion length are needed. Doping and the particulars of full device fabrication need to be worked out as well. Our growth scheme avoids using expensive single-crystal substrates and associated complex epitaxial structures, which have thus far hindered the market success of III-V solar cells. Metal foil substrates not only reduce cost at the material growth step, but also at downstream processing steps. For example, flexible foil substrates are a natural fit for roll-to-roll processing.¹³ They are robust, light-weight, and act as excellent barriers to the environment. Poly-InP grown using our technique shows great promise for high-efficiency, low-cost solar cells.

REFERENCES

1. K.J. Bachmann, E. Buehler, J.L. Shay, S. Wagner, *Appl. Phys. Lett.* **29**, 121 (1976).
2. R.L. Woo, R. Xiao, Y. Kobayashi, L. Gao, N. Goel, M.K. Hudait, T.E. Mallouk, R.F. Hicks, *Nano Lett.* **8**, 4664 (2008).
3. R.E. Algra, M.A. Verheijen, M.T. Borgstrom, L.-F. Feiner, G. Immink, W.J.P. van Enkevort, E. Vlieg, E.P.A.M. Bakkers, *Nature* **456**, 369 (2008).
4. H. Gottschalk, G. Patzer, H. Alexander, *Phys. Status Solidi A* **45**, 207 (1978).
5. P.I. Gaiduk, F.F. Komarov, V.S. Tishkov, W. Wesch, E. Wendler, *Phys. Rev. B* **61**, 15785 (2000).
6. ICDD PDF-2. Entry 00-032-0452. **2003**.
7. G.F. Alfrey, P.H. Borchers, *J. Phys. C: Solid State Phys.* **5**, L275 (1972).
8. A. Mooradian, G.B. Wright, *Solid State Commun.* **4**, 431 (1966).
9. L. Artús, R. Cuscó, J.M. Martín, G. González-Díaz, *Phys. Rev. B* **50**, 11552 (1994).
10. W.J. Turner, W.E. Reese, G.D. Pettit, *Phys. Rev.* **136**, A1467 (1964).
11. M. Bugajski, W. Lewandowski, *J. Appl. Phys.* **57**, 521 (1985).
12. G. Perna, V. Capozzi, V. Augelli, T. Ligonzo, L. Schiavulli, G. Bruno, M. Losurdo, P. Capezzuto, J.L. Staehli, M. Pallara, *Semicond. Sci. Technol.* **16**, 377 (2001).
13. M.H. Lee, N. Lim, D.J. Ruebusch, A. Jamshidi, R. Kapadia, R. Lee, T.J. Seok, K. Takei, K.Y. Cho, Z. Fan, H. Jang, M. Wu, G. Cho, A. Javey, *Nano Lett.* **11**, 3425 (2011).

CHAPTER 3

POLYCRYSTALLINE INP GROWN BY CSS*

3.1 INTRODUCTION

Here we report a scalable growth method for producing InP crystals directly on metal foils that allows both spatial control (e.g., polycrystalline thin film and selective area growth of crystalline arrays) and morphology control (e.g., from nanowires to faceted crystals) using the close-spaced sublimation (CSS) technique. The CSS technique¹ provides a small precursor transport distance, which allows efficient transfer of source material to the substrate. Consequently, CSS allows a high crystalline growth rate and potentially high throughput with minimal source material loss.² CSS is a well-established method for making polycrystalline thin-film solar cells, especially for CdTe with reported device efficiencies of 17.3%,³ which highlights its ability to yield high quality crystal growth. In this research, we further reveal that the enclosed space facilitates saturated vapor phases of the source materials, thereby enabling nucleation and growth of high quality InP crystals with promising optical properties as examined by steady-state and time-resolved photoluminescence analyses. Thus CSS growth of InP should be a promising candidate for use in thin film III-V solar cells applications.

3.2 EXPERIMENTAL DETAILS

3.2.1 CSS system and growth procedures

The CSS system used here was built by Engineered Science. The glass chamber size was about 10-inch long and 5-inch diameter. The glass folder held graphite blocks. Inside the graphite blocks precursor InP powder (99.999%, China Rare Metal Co.) and molybdenum (Mo) foil (99.95%) were sandwiched. The spacer thickness was ~2 mm. The chamber was evacuated and purged with N₂

* This chapter has been published in similar form as Kiriya and Zheng, *et. al. Journal of Applied Physics*. 2012, **112**, 123102. Permission has been granted to include it here.

gas. Growth substrate (T_{sub}) and source (T_{so}) temperatures ranged from $T_{\text{sub}} = 485$ to 700 °C and $T_{\text{so}} = 650$ to 800 °C, respectively. Growth times explored were 15 – 60 minutes and pressure (P) range was 0.1 to 40 Torr. The Mo foils used were 25 μm thick and cleaned with acetone and isopropanol prior to growth.

3.2.2 Fabrication of patterned Mo substrates

Mo dots on silicon oxide were fabricated as follows: 50 nm thick, 1.5 μm diameter Mo circles on silicon oxide/silicon wafer were fabricated using a standard lift-off process. The thickness of silicon oxide was 50 nm, and the Mo was deposited via sputtering. The Mo holes were fabricated as follows: 15 nm silicon oxide (SiO_x) was deposited on Mo foil by electron-beam evaporation. A photoresist (PMMA 495 C2) was spin coated (3000 rpm, 1 min) on the Mo foil (25 μm). The foil was baked for 1 min at 180 °C on a hotplate. Acetone was then poured onto a patterned polydimethylsiloxane (PDMS, same dot pattern as shown in Figure 4a), and the PDMS put onto the foil for 1 h. The PDMS dot pattern was subsequently transferred to the foil. Finally, the SiO_x was etched using 0.2% hydrofluoric acid, and the photoresist removed by remover-PG.

3.2.3 Physical measurements

The X-ray diffraction (XRD) was taken on a Bruker AXS D8 Discover GADDS XRD Diffractometer system. The photoluminescence (PL) excitation source was a 785 nm laser with ~ 5 μm spot size, and the detector was a silicon CCD. The time-resolved photoluminescence (TRPL) excitation source was a tunable Mira 900-F Ti-sapphire laser set to 800 nm, producing 200 fs pulses at 75.3 MHz. The detector was a Si APD (id-100) produced by id Quantique hooked up to a TCSPC module (SPC-130) from Becker & Hickl. The sample (InP crystals on Mo dots shown in Figure 4b) for PL and TRPL measurements was treated by 2 min 1% hydrochloric acid (HCl) and 2 min 15% nitric acid (HNO_3) in advance. These treatments removed surface oxides and passivated the InP crystals.^{4,5} Scanning electron microscope (SEM) images were taken on a Zeiss Gemini Ultra-55 and JEOL 6340F. Mott-Schottky measurements were performed with a SP-300 Potentiostat set-up (BioLogic, France) for the InP polycrystalline film ($T_{\text{sub}} = 600$ °C (15 min), 680 °C (30 min) then 600 °C (15 min), $T_{\text{so}} = 800$ °C, $P = 0.2$ Torr) in 3.0 M potassium chloride (KCl) solution. Before the measurement, the InP polycrystalline film was transferred to a glass substrate by peeling it off from the Mo foil using glue. The InP polycrystalline film was covered by a glue (Advanced Formula Instant Crazy Glue, Elmer's Products, Inc), then lifted off from the Mo foil after curing of the glue. The sample was etched before the measurement by 1 M HCl for 2 min to remove any residual molybdenum phosphide (MoP) that may have peeled off. The potential scan started at -0.4 V down to 0.2 V with steps of 20 mV. The frequency range was 99 to 100 kHz. The carrier concentration was calculated from the slope of the $1/C^2$ vs potential plot, where C is the capacitance of the space charge layer. According to the frequency dispersion data, the free electron concentration was $0.8\text{-}4.6 \times 10^{18} \text{ cm}^{-3}$.

3.3 RESULTS AND DISCUSSION

Figure 1a illustrates an overview of the CSS system. It includes two graphite blocks encapsulated in a glass chamber. The top and bottom graphite blocks partially enclose a substrate and the InP

source powder, respectively, and these are separated by a spacer (thickness ~ 2 mm). The temperature of each graphite block is controlled by separate halogen lamps and monitored by separate thermocouples. The important parameters in a CSS system are i) the temperatures of the source material (T_{so}) and the growth substrate (T_{sub}), ii) chamber pressure (P), iii) and growth time (Figure 1b). Thus, these parameters were explored to optimize the growth conditions. Additionally proper substrate choice is critical. Here Mo foil is chosen due to: i) a lack of any In-Mo intermetallics up to the growth temperature, and ii) low solubility of In in Mo at the growth temperature. Additionally, the thermal expansion coefficient of Mo is similar to InP.⁶

By sublimation of InP powder, polycrystalline InP was grown on Mo foil as illustrated in Figure 2a. From visual inspection, the grown InP films exhibited large area ($2\text{ cm} \times 2\text{ cm}$) uniformity (Figure 2b). Figures 2c, d show the top- and side-view SEM images of a representative polycrystalline InP thin film ($\sim 7\text{ }\mu\text{m}$ thickness) grown on Mo foil. The average grain size for this growth condition is $\sim 5\text{ }\mu\text{m}$. The crystalline size and morphology are highly dependent on the

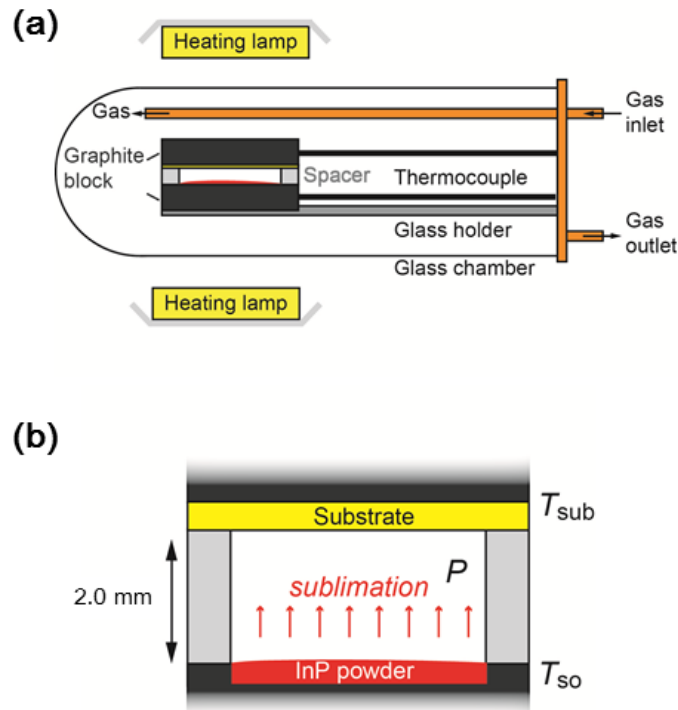


Figure 1. Schematic illustration of the CSS system. (a) Overview of the CSS instrument. A glass chamber contains two graphite blocks. The substrate and precursor powder are located inside the graphite top and bottom blocks, respectively. Graphite blocks are heated using halogen lamps while the temperature of the blocks is monitored using thermocouples. Atmosphere of the chamber is exchanged using gas inlet and outlet. Here we used N_2 gas. Pressure inside the chamber is also controlled by adjusting the N_2 gas flow. (b) An enlarged image of the sublimation component of the chamber. Controlled parameters are substrate temperature (T_{sub}), source InP powder temperature (T_{so}), pressure of the system (P) and growth time.

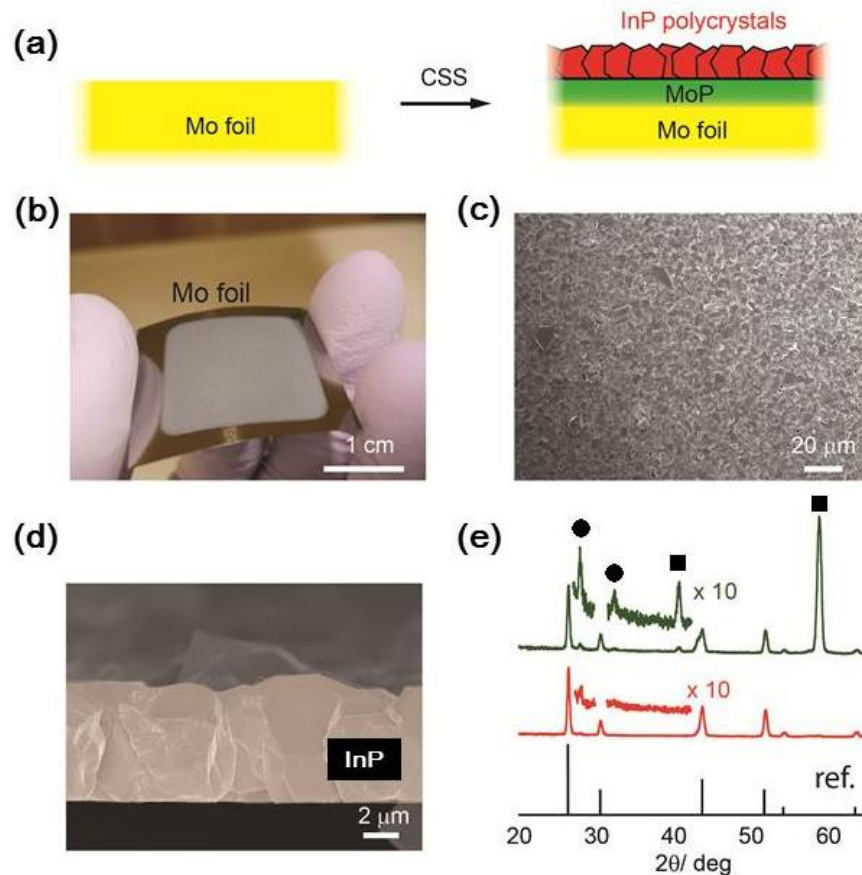


Figure 2. Polycrystalline InP growth on a Mo foil. (a) Illustrative image before (left) and after (right) the growth of a polycrystalline InP film on a Mo foil. (b) Macroscopic picture of uniform InP polycrystalline film fabricated on a Mo foil. (c) SEM image of the InP polycrystalline film growth with the condition of ($T_{\text{sub}} = 600$ °C (15 min), 680 °C (30 min) then 600 °C (15 min), $T_{\text{so}} = 800$ °C, $P = 0.2$ Torr). The crystalline size is 5-7 μm . (d) Cross-sectional SEM image of a free-standing InP polycrystalline film which delaminated after cutting the foil. The film thickness is estimated to be ~ 7 μm . (e) XRD patterns for InP crystals. Curves are normalized to the (111) peak of InP ($2\theta = 26.3$ °) and offset. (top) Dispersed InP crystals fabricated on Mo foil ($T_{\text{sub}} = 700$ °C, $T_{\text{so}} = 750$ °C, $P = 1$ Torr, 30 min growth). (110) and (200) of Mo peaks (■) and (100) of MoP peaks (●) were labelled. (middle) InP polycrystalline continuous film on a Mo foil ($T_{\text{sub}} = 685$ °C, $T_{\text{so}} = 800$ °C, $P = 1$ Torr, 30 min growth). (bottom) Reference InP peaks. Peaks from left to right: (111), (200), (220), (311), (222), and (400).

growth condition (*vide infra*) and the most continuous polycrystalline film was obtained using $T_{\text{sub}} = 600$ °C (15 min), 680 °C (30 min), then 600 °C (15 min) and $T_{\text{so}} = 800$ °C and $P = 0.2$ Torr in the growth procedure (Figure 2c, d). The initial lower temperature growth ($T_{\text{sub}} = 600$ °C) is used to promote uniform nucleation of InP, enabling continuous film growth, while the higher temperature growth ($T_{\text{sub}} = 680$ °C) is used to promote larger grain sizes. The final low temperature step is necessary to minimize pinholes in the film. XRD characterization shows the InP crystalline peaks (Figure 2e) match those of zincblende InP.⁷ No preferential orientation was observed. By reducing the source temperature, lower flux growth conditions (e.g., $T_{\text{sub}} = 700$ °C, $T_{\text{so}} = 750$ °C, $P = 1$ Torr, and 30 min growth) were obtained with low surface coverage of InP crystals on the substrate. From the resulting samples, both Mo and MoP peaks^{8,9} were observed. This result is consistent with the previous InP growth using MOCVD. Note that from our previous study of InP

MOCVD growth on Mo, a self-limiting thin layer (~ 50 nm thickness) of MoP is found to form at the Mo/InP interface during the growth. Here, the Mo surface is also phosphorized during the CSS growth as illustrated in Figure 2a. We note here that the use of flexible metal foil substrates is attractive given its compatibility with large-scale industrial processes such as roll-to-roll fabrication.

Mott-Schottky measurements were performed to characterize the carrier concentration of the CSS grown InP films. The results indicate that the grown InP is *n*-type, with an electron carrier concentration in the range of $\sim 0.8\text{--}4.6 \times 10^{18} \text{ cm}^{-3}$. This relatively high electron concentration could be due to carbon incorporation¹⁰ from the graphite blocks used in the set-up or phosphorous vacancies near the surface, both of which are known to be donors in InP. These unintentional doping sources can be mitigated in the future by coating the graphite blocks with an inert material and/or by mixing in additional phosphorous to the source InP powder. It is also possible for impurities in the source powder to cause doping.

Additionally, the temperature and pressure dependence of InP structures were systematically explored. The morphology of the InP crystals as shown in Figure 3 are highly dependent on T_{sub} and P . Specifically, in the range of T_{sub} between 485 °C to 650 °C with P greater than 1 Torr, we obtained self-catalyzed InP nanowires (NWs). The NW morphologies can be categorized into two types depending on the conditions: i) NWs with In-rich tips and ii) NWs without tips. The vapor-liquid-solid (VLS) growth mechanism¹¹ is well established for NW growth, and it appears the NWs with In-rich tips grow via a VLS mechanism, where an indium droplet first forms on the substrate, followed by absorption of phosphorous from the environment and finally precipitation of InP. On the other hand, the NWs without tips are observed at higher temperatures (above 500 °C). This morphology suggests that both VLS and vapor-solid-solid (VSS) mechanisms are at work. This agrees well with previous reports of NWs fabricated by metal organic vapor phase epitaxy.¹¹ At

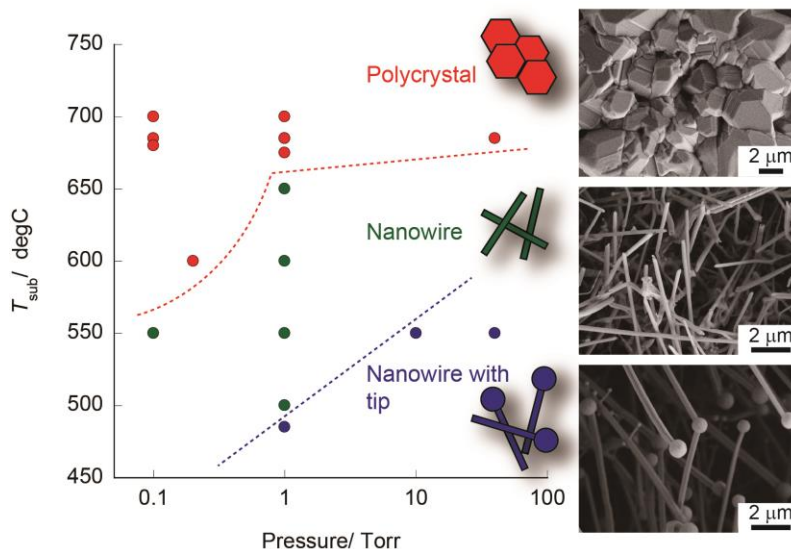


Figure 3. Temperature (T_{sub})–pressure (P) dependence of the InP morphologies grown by CSS. The SEM images from top to bottom are as follows: polycrystalline film ($T_{\text{sub}} = 685$ °C, $T_{\text{so}} = 800$ °C, $P = 1$ Torr, 30 min growth), nanowires ($T_{\text{sub}} = 550$ °C, $T_{\text{so}} = 700$ °C, $P = 0.1$ Torr, 30 min growth), and nanowires with In-rich tips ($T_{\text{sub}} = 550$ °C, $T_{\text{so}} = 700$ °C, $P = 10$ Torr, 30 min growth).

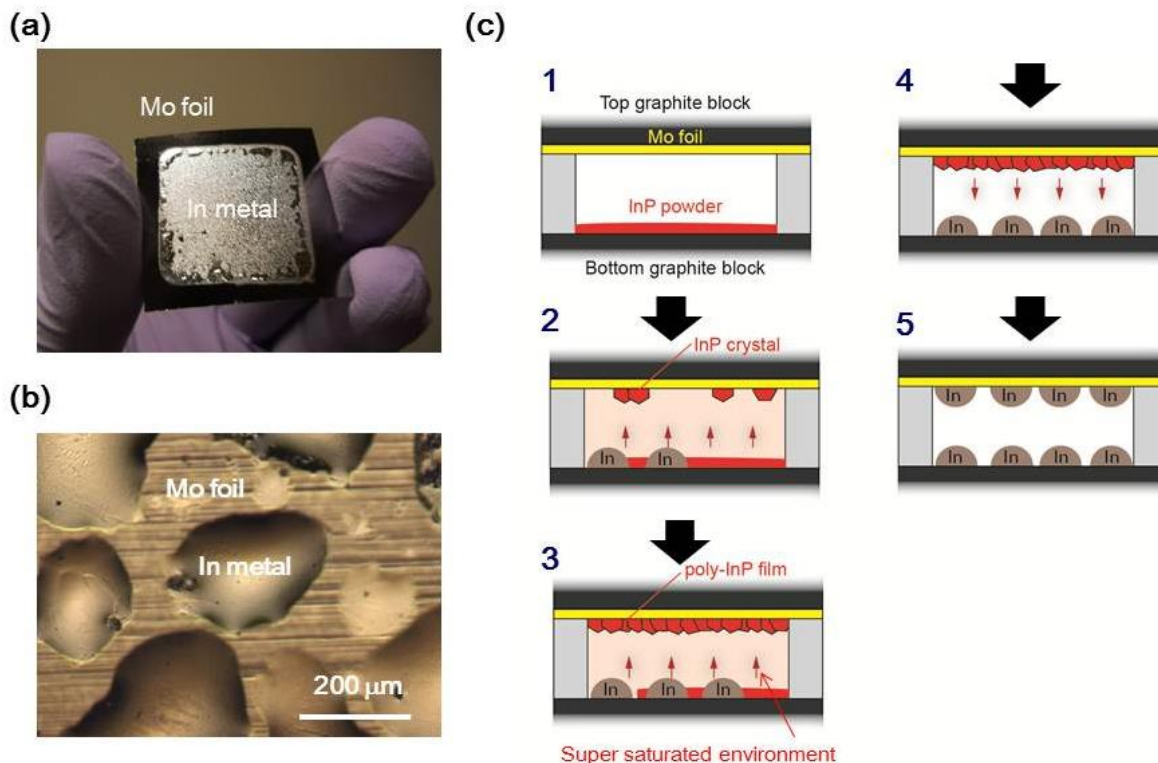


Figure 4. Mechanism for the growth of polycrystalline InP film in the confined space of CSS. (a, b) The growth time of 60 min produces indium metal bumps on Mo foil, not InP. The condition is as follows: $T_{\text{sub}} = 685\text{ }^{\circ}\text{C}$, $T_{\text{so}} = 800\text{ }^{\circ}\text{C}$, $P = 0.1\text{ Torr}$, and 60 min annealing time. The time it takes for phosphorous to run out depends on the amount of InP source. (c) The mechanism of the InP polycrystalline film growth and decomposition process in CSS system.

higher temperature ($T_{\text{sub}} > 650\text{ }^{\circ}\text{C}$ and $P > 1\text{ Torr}$), we obtained faceted (polycrystalline) InP crystals as shown in Figures 2c, d and Figures S4-6. Though not exhaustive, this study clearly shows CSS can controllably produce morphologies ranging from NWs to polycrystalline films by varying the growth conditions. Therefore, application-specific structures can be engineered. For example, water-splitting and catalysis may benefit from the NW structures¹² because of the large surface area, while faceted crystals may be better for fabricating high efficiency solar cells.

Next the time dependence of the CSS InP growth mechanism was studied. 30 min and 60 min growths were performed with all other conditions held constant ($T_{\text{sub}} = 685\text{ }^{\circ}\text{C}$, $T_{\text{so}} = 800\text{ }^{\circ}\text{C}$, $P = 0.1\text{ Torr}$ and 0.5 g InP source). Figure 4 shows the results for 60 min sublimation time; silver-colored In bumps were obtained on the Mo foil without InP. On the other hand, the 30 min growth at the same conditions produced the InP crystalline phase (Figure 2e and Figure S5). These results enable postulation of the CSS growth mechanism (Figure 4). During the initial sublimation processes (Figure 4c step 1 to 2), both indium and phosphorous sublime resulting in a net flux towards the substrate and InP crystals growth. Given the higher vapor pressure of P as compared to In, after some time (step 3), further annealing leads to a net phosphorous loss from the chamber, causing the InP crystals on the substrate to decompose (step 4). Eventually, indium bumps on Mo foil are obtained (step 5) if the samples are heated for too long. We note that we kept T_{sub} the same in all steps 1 to 5, revealing that $T_{\text{sub}} = 685\text{ }^{\circ}\text{C}$ is high enough to decompose InP. Therefore, the

InP crystals are grown at higher temperature than their decomposition temperature; this indicates that both phosphorous and indium are “super-saturated” during the growth process when the growth time is not too long. This super-saturation pushes the equilibrium shown in eqn. (1)¹³ towards formation of InP crystals.



The super-saturated environment, facilitated by the confined space in a CSS system, also enables us to operate above the disassociation temperature. Therefore, crystals are synthesized at a higher temperature, which potentially allows the growth of higher quality crystals.

Spatial control of the crystalline growth is important for a variety of applications. Primarily, for solar cells the benefits include reducing grain boundaries¹⁴ which act as recombination centers and shunt paths^{14,15}. In this context, we examined the selective growth of InP crystals using the CSS technique. Two types of substrates were examined by patterning Mo with a silicon oxide masking layer as shown in Figure 5. In the first type of sample, Mo holes (1.5 μm diameter) are made by depositing a 15 nm SiO_x layer via electron beam evaporation on a Mo foil, followed by patterned etching of SiO_x . InP growth only occurred on the Mo holes; each crystal (about 5 μm diameter) sat on the Mo holes without any InP nucleation on the SiO_x surface (Figure 5a). The reason for this is that InP growth is strongly inhibited on silicon oxide surfaces.¹⁶ In the second type of substrate, 50 nm thick sputtered Mo dots (1.5 μm diameter) were patterned on a silicon oxide/silicon wafer (thermal oxide, 50 nm thickness) using traditional photolithography and lift-off processes. 5 to 7 μm InP crystals were then selectively grown on the Mo dots. The InP crystals

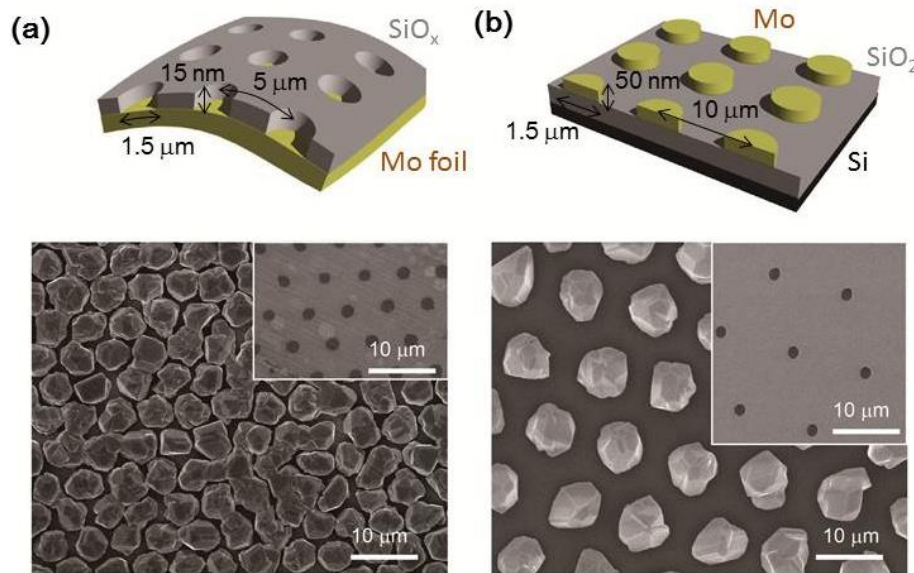


Figure 5. Spatial control of InP crystal growth. (a) (Top) Illustrative image of Mo holes on the foil covered with silicon oxide. (Bottom) SEM images of the InP crystal growth on the Mo holes and (Inset) the patterned foil before the CSS growth. (b) (Top) Illustrative image of Mo dots on a silicon substrate covered with silicon oxide. (Bottom) SEM images of the InP crystal growth on the Mo dots and (Inset) the patterned substrate before the CSS growth. Scale bars are 10 μm .

are separate from each other and nearly all look like single crystals, which can be seen from a cross-sectional SEM view. Each crystal was about 7 μm in height. As demonstrated here, selective area growth of InP crystals on both Mo holes and dots is possible, which can facilitate the use of CSS for making precise optoelectronic devices.

We further analyzed the optoelectronic properties of InP crystals. Room temperature steady-state photoluminescence (PL) spectra (Figure 6a) of InP crystals on Mo dots show an asymmetric feature with the peak at ~ 1.34 eV. Compared to an $8 \times 10^{15} \text{ cm}^{-3}$ *n*-type InP single-crystal wafer, the peak position is nearly the same and the full-width-at-half-maximum (FWHM) is slightly broader (0.060 eV vs. 0.045 eV). This result shows the high optical quality of our CSS grown InP. The slight peak broadening can be explained by a higher carrier concentration in our material,¹⁷ which is corroborated by the doping levels ($0.8\text{-}4.6 \times 10^{18} \text{ cm}^{-3}$) extracted from Mott-Schottky measurements on thin films. To further analyze the quality of the crystals from the underlying recombination processes, a study of the photoluminescence intensity as a function of incident laser power was performed (Figure 6b). The result suggests that exciton recombination dominates. This relationship can be seen in a log-log plot, for which the relation is given by $I_{\text{PL}} = CI_L^k$, where I_{PL} is the PL intensity, I_L is the illumination power, C is a proportionality constant, and k is the power dependence of the PL intensity.¹⁸ For a direct band gap material, a value of $k < 1$ is expected for free-to-bound recombination (electron to acceptor or hole to donor), $k = 1$ is expected for free or bound exciton recombination, and $k = 2$ is expected when defect state recombination dominates.¹⁸ We find $k = 1.13 \pm 0.03$ by a linear fit to the log-log plot. This result provides additional evidence for a high optical quality film, as the close value of $k \sim 1$ indicates defect (non-radiative) recombination is not significant.

To determine the carrier lifetime, time-resolved photoluminescence (TRPL) measurements were carried out for the InP crystals on Mo dots (Figure 6c). The sample was illuminated with 800 nm incident light at an illumination power of $P_0 = 440$ mW and a spot size of $A = \pi \cdot 200^2 \mu\text{m}^2$, giving an excess carrier concentration of $\sim 6 \times 10^{17} \text{ cm}^{-3}$ at the surface; the generation rate is given by $G = \alpha \cdot P_0 / (E_{\text{ph}} \cdot A)$, where absorption coefficient (α) = $3.37 \times 10^4 \text{ cm}^{-1}$, and the photon energy (E^{ph}) = 1.55 eV. The TRPL decay time ($1/e$) of our sample is 0.89 ns. The previously reported TRPL decay time in an InP single-crystalline film grown by the liquid phase epitaxial process is 0.94 ns for the doping concentration of $5.3 \times 10^{18} \text{ cm}^{-3}$.¹⁹ This provides further evidence that the CSS grown crystals have a similar optical quality as the InP single crystalline wafers.

Furthermore, the diffusion equation was solved to simulate a TRPL decay curve. The fitting parameters were bulk recombination lifetime (τ) and effective surface recombination velocity (SRV) at the top surface. Due to the thickness of the sample ($\sim 7 \mu\text{m}$), the lifetime was insensitive to back surface recombination, which was therefore not considered. The simulated decay curve was then convolved with the measured instrument response and fit to the experimentally measured curve (Figure 6c). Using an ambipolar diffusion coefficient of $5.2 \text{ cm}^2 \text{ s}^{-1}$, and a bulk electron concentration of $3 \times 10^{18} \text{ cm}^{-3}$, τ and effective SRV were extracted to be 3.0 ns and $1.9 \times 10^5 \text{ cm s}^{-1}$, respectively. This SRV value is higher than previous TRPL results for *n*-type InP;²⁰⁻²³ however, it should be possible to reduce this with appropriate surface treatment. It should be noted that the ambipolar diffusion coefficient was calculated using electron and hole mobilities of single crystalline InP for the same carrier concentration. In the future, detailed Hall effect measurements need to be performed to more directly assess the diffusion coefficients and thereby the carrier

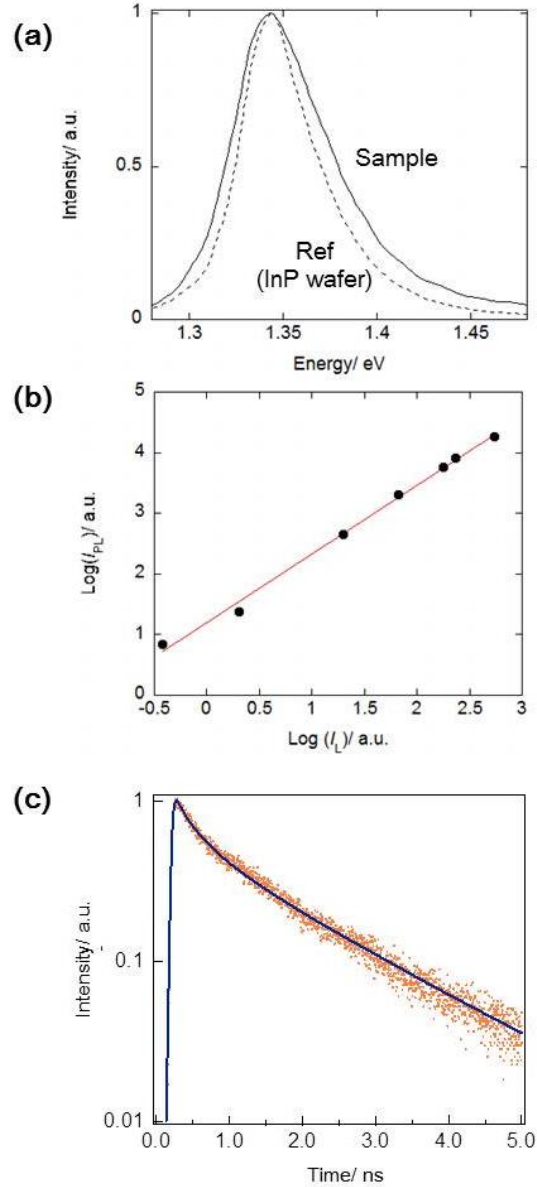


Figure 6. Optical properties of the InP crystals on the Mo dots. (a) PL spectra of CSS grown InP sample (solid line) and an InP reference wafer (dashed line, electron concentration is $8 \times 10^{15} \text{ cm}^{-3}$). (b) Laser power (I_L) vs. PL intensity (I_{PL}) plot. The red line is a linear fit with a slope of ~ 1.13 . (c) TRPL plot and the simulated curve (solid line) of the InP crystals on Mo dots. The sample was treated by 2 min 1% HCl and 2 min 15% HNO_3 in advance.

lifetimes. TRPL studies on single crystal *n*-InP with similar concentrations have not extracted the bulk recombination time in the past.

3.4 CONCLUSIONS

We have demonstrated morphology and spatial control of InP grown on Mo foils using the CSS technique. The crystals grown using this technique are composed of micron-sized grains, and show

respectable carrier lifetimes as measured by TRPL characterization. The confined space of CSS produces supersaturation of the source gases enabling growth at higher temperatures, which promotes high optical quality InP crystals. In the future, further characterization of the minority carrier lifetime, mobility, and diffusion lengths are needed. Appropriate dopants, substrates and surface modifications will also need to be explored for making high quality opto-electronic devices. This simple growth scheme relies only on sublimation of a solid powder inside the growth chamber, removing the need for expensive systems and single-crystalline substrates, which are limiting factors in the current III-V growth technologies for low-cost devices. The use of metal foil substrates is important to not only reduce cost at the material growth step, but also at the downstream processing steps given its mechanical properties. Consequently, CSS grown InP shows high promise for high-efficiency and low-cost solar cells.

REFERENCES

1. H. Nicoll, *J. Electrochem. Soc.* **110**, 1165 (1963).
2. J. Mimila-Arroyo, J. Diaz, A. Lusson, C. Grattapain, R. Bisaro, J. C. Bourgoin, *Mater. Sci. Technol.* **12**, 178 (1996).
3. First Solar, July 26, 2011 (<http://investor.firstsolar.com/releasedetail.cfm?ReleaseID=593994>).
4. S. K. Krawczyk, G. Hollinger, *Appl. Phys. Lett.* **45**, 870 (1984).
5. P. A. Bertrand, *J. Vac. Sci. Technol.* **18**, 28 (1981).
6. K. J. Bachmann, E. Buehler, J. L. Shay, S. Wagner, *Appl. Phys. Lett.* **29**, 121 (1976).
7. ICDD PDF-2, Entry 00-032-0452, 2003.
8. ICDD PDF-2, Entry 00-065-6024, 2003.
9. ICDD PDF-2, Entry 00-089-5156, 2003.
10. W. K. Lili, D. I. Lubyshev, P. Specht, R. Zhao, E. R. Weber, J. Gebauer, A. J. SpringThorpe, R. W. Streater, S. Vijarnwannaluk, W. Songprakob, R. Zallen, *J. Vac. Sci. Technol. B*, **18**, 1594 (2000).
11. R. L. Woo, L. Gao, N. Goel, M. K. Hudait, K. L. Wang, S. Kodambaka, R. F. Hicks, *Nano Lett.* **9**, 2207 (2009).
12. M. H. Lee, K. Takei, J. Zhang, R. Kapadia, M. Zheng, Y.-Z. Chen, J. Nah, T. S. Matthews, Y.-L. Chueh, J. W. Ager, A. Javey, *Angew. Chem. Int. Ed.*, in press, 2012 (DOI 10.1002/ange.201203174).
13. K. Weiser, *J. Phys. Chem.* **61**, 513 (1957).
14. D. Zubía, C. López, M. Rodríguez, A. Escobedo, S. Oyer, L. Romo, S. Rogers, S. Quiñónez, J. McClure, *J. Elect. Mater.* **36**, 1599 (2007).
15. P. N. Gibson, M. A. Baker, E. D. Dunlop, M. E. Özsan, D. Lincot, M. Froment, G. Agostinelli, *Thin Solid Films*, **387**, 92 (2001).
16. K. Araki, J. U. Seo, S. Hasegawa, H. Asahi, *Phys. Stat. Sol. C*, **9**, 2766 (2008).
17. M. Bugaiski, W. Lewandowski, *J. Appl. Phys.* **57**, 521 (1985).
18. T. Schmidt, K. Lischka, W. Zulehner, *Phys. Rev. B*, **45**, 8989 (1992).
19. G. Augustine, B. M. Keyes, N. M. Jokerst, A. Rohatgi, R. K. Ahrenkiel, *Proc. 5th Int. Conf. Indium Phosphide Related Mater.*, 636–639 (1993).
20. T. Nakamura, T. Katoda, *J. Appl. Phys.* **55**, 3064 (1984).
21. Y. Rosenwaks, Y. Shapira, D. Huppert, *Phys. Rev. B*, **44**, 13097 (1991).
22. Y. Rosenwaks, Y. Shapira, D. Huppert, *Phys. Rev. B*, **45**, 9108 (1992).
23. S. Bothra, S. Tyagi, S. K. Ghandhi, J. M. Borrego, *Solid-State Electron.* **34**, 47 (1991).

CHAPTER 4

POLYCRYSTALLINE THIN-FILM INP SOLAR CELLS*

4.1 INTRODUCTION

In this chapter we describe the design and fabrication of one proof-of-principle cell structure using TF-VLS grown *p*-InP absorber layers on Mo back contact substrates. The top window layer is an electron-selective titanium dioxide (TiO₂) film along with indium tin oxide (ITO) as the transparent conducting oxide. This forms a complete PV device stack of Mo/*p*-InP/*n*-TiO₂/ITO. The optoelectronic uniformity and effect of grain boundaries was examined by photoluminescence (PL) imaging and electron beam-induced current (EBIC) mapping. We also discuss the *ex-situ* doping of these films from as-grown *n*-type to Zn-doped *p*-type. The first generation cells exhibit a power conversion efficiency of 12.1% under simulated 1 sun illumination with a V_{OC} of 692 mV. Furthermore, PL efficiency measurements show we have not reached the full optoelectronic potential of the material and higher device efficiency can be unlocked by improved device design.

4.2 POLYCRYSTALLINE INP GROWN BY THE TF-VLS METHOD

Recently we have developed the thin-film vapor-liquid-solid (TF-VLS) growth technique to produce high optoelectronic quality InP absorber layers directly on molybdenum (Mo) substrates. In this implementation of the technique, a layer of In confined between a Mo substrate and silica (SiO_x) cap is heated to a temperature where the In is a liquid. Then, a phosphorus vapor is introduced and diffuses through the SiO_x into the In liquid, causing precipitation of solid InP. The InP grows into a polycrystalline film with large (>100 μm) lateral grain sizes.^{1,2} The benefits of TF-VLS growth over traditional metalorganic chemical vapor deposition (MOCVD) growth are

* This chapter has been submitted for publication in a similar form.

high throughput, high materials utilization efficiency, and non-epitaxial substrates. The absorber layer is also grown directly on the back contact, simplifying the fabrication process.

TF-VLS growth has so far been demonstrated with InP as a model material system.¹ InP has a direct band gap of 1.34 eV, with a Shockley-Queisser efficiency limit of ~33% under AM1.5G. Additionally, the high absorption coefficient allows a thin layer, ~1-2 μm , to efficiently absorb incoming light. With these properties in mind, TF-VLS-grown InP is an ideal material for the absorber layer in a single junction solar cell. The TF-VLS process is shown in Fig. 1.

First, the non-epitaxial substrate is prepared, where we have used ~1 μm of sputtered molybdenum (Mo) on a glass substrate. Then ~1 μm thick indium (In) is deposited by a physical vapor deposition process along with a ~50 nm silicon oxide (SiO_x) cap. The entire stack is heated to a temperature of 450-750 $^\circ\text{C}$. In this temperature range, the In is liquid and the SiO_x cap confines it and prevents it from dewetting. Phosphine (PH_3) gas is then introduced. After it decomposes, the phosphorus (P) vapor diffuses through the SiO_x cap and into the In liquid. Upon supersaturating the In liquid, InP solid precipitates out of the solution. Each InP nuclei then grows rapidly in the lateral direction until the entire In film is converted to InP. Crucially, the InP nuclei are spaced hundreds of microns apart, which determines the lateral grain size. The large nuclei spacing enabled in the TF-VLS process arises from the creation of large P depletion zones around each nuclei.²

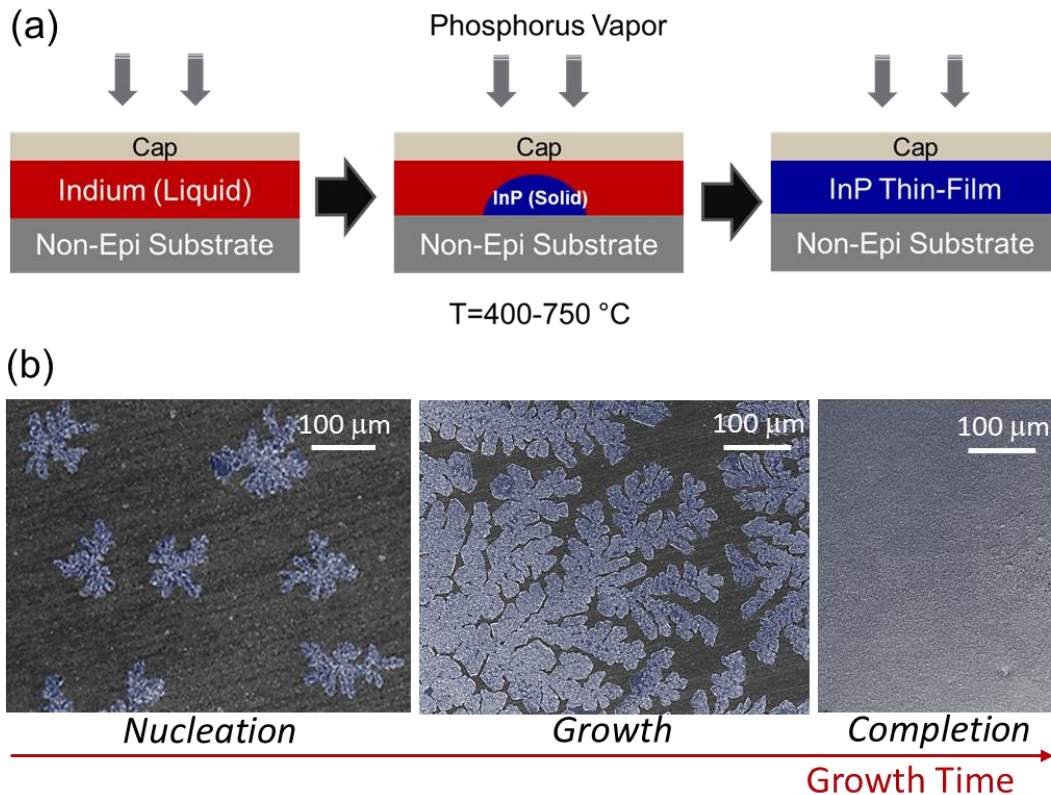


Figure 1. (a) Schematic of the TF-VLS growth process for InP. (b) SEM images at various stages in the TF-VLS growth process: nucleation, grain growth, and complete thin film formation. (Panel (b) reproduced from Kapadia and Yu, et. al. *Sci. Rep.* 2013.)

Once an InP nucleus is formed, it rapidly consumes the phosphorous atoms in its spatial proximity due to the rapid diffusion of P atoms in liquid In (as compared to the flux of incoming P atoms through the solid-state SiO_x cap). This P depletion zone prevents further nucleation events in the surrounding area and thus results in large grain sizes. This process results in homogenous polycrystalline thin-films with $\sim 2 \mu\text{m}$ thickness (determined by the thickness of initial In film) and lateral grain sizes of 50-1000 μm . Further, patterning a nucleation promoter can selectively control where the InP nucleates.² As-grown InP is *n*-type due to native defects that stabilize the Fermi level closer to the conduction band. It has an electron Hall concentration of $\sim 5\text{-}8 \times 10^{16} \text{ cm}^{-3}$, not strongly dependent on the growth temperature. But the Hall mobility does strongly depend on the growth temperature, reaching $\sim 500 \text{ cm}^2/\text{Vs}$ for a growth temperature of 750 °C (Fig. 2a). The TRPL lifetime is $\sim 2 \text{ ns}$ at the same growth temperature (Fig. 2b), longer than that achieved in CSS InP.

The grown InP can also be doped *p*-type *in-situ* or *ex-situ*. In an *in-situ* process, a *p* dopant such as Zn, Cd, or Mg can be introduced in the vapor phase along with the PH_3 . *Ex-situ* doping can be accomplished similarly using a gas phase diffusion process. Due to the fast diffusion of P inside liquid In, the rate-limiting step is diffusion of P through the SiO_2 cap layer. So, for a given cap thickness, the growth rate is controlled by the partial pressure of P vapor. Growth times are < 5 minutes at 10 Torr PH_3 partial pressure and 750 °C, and this can be shortened at industrial scale with higher PH_3 partial pressures. From this process overview, TF-VLS growth clearly addresses the three main cost components of traditional III-V manufacturing: sputtered Mo replaces the epitaxial wafer substrate, physical vapor deposition uses In efficiently, and the growth throughput can be much higher.

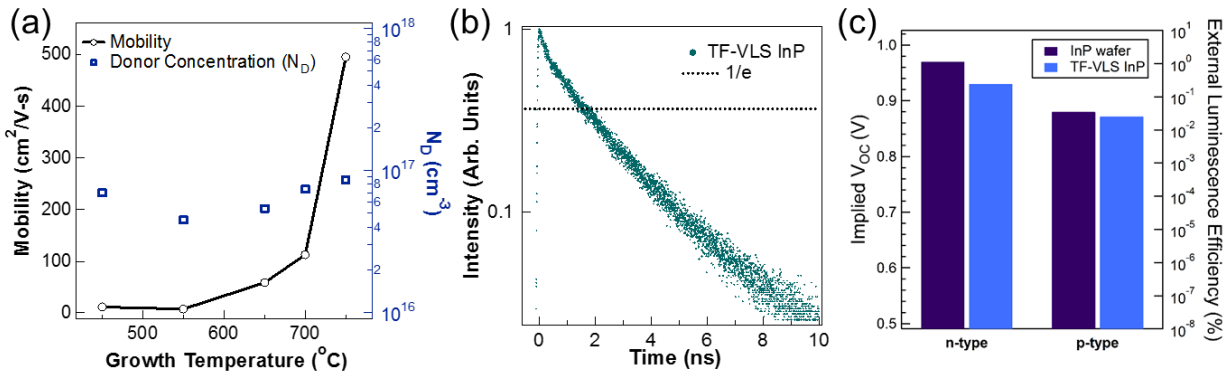


Figure 2. Implied V_{OC} and external luminescence efficiency at 1-sun equivalent illumination ($1,000 \text{ W}/\text{m}^2$). (Panel (a) and (b) reproduced from Kapadia and Yu, et. al. *Sci. Rep.* 2013.)

The optoelectronic quality of TF-VLS-grown InP approaches that of single crystal.¹ Fig. 2c shows the 1 sun implied open-circuit voltage (V_{OC}) and external luminescence efficiency of *n*-type and *p*-type VLS InP compared to single crystal wafers of comparable doping. The measured implied V_{OC} represents the maximum open-circuit voltage attainable given perfect contacts.¹ For as-grown TF-VLS *n*-InP, the measured implied V_{OC} is $\sim 930 \text{ mV}$, which is only 40 mV below the value obtained for a single crystal InP reference of similar doping concentration. This large implied V_{OC} can be expected to be even higher in material grown in industrial settings with better process control. For *ex-situ* Zn doped TF-VLS *p*-InP, the implied V_{OC} currently reaches $\sim 870 \text{ mV}$ (Figure

2). With a short-circuit current density (J_{sc}) of 32 mA/cm² and fill factor of 81%, which are close to what we have achieved on reference solar cells made from single crystal *p*-InP,³ the projected maximum efficiencies for *n*-type and *p*-type TF-VLS InP are 24.1% and 22.6%, respectively.

4.3 FABRICATION AND DEVICE STRUCTURE

The cell fabrication process shown in Fig. 3a begins with growth of the InP absorber layer on either sputtered Mo (~2 μm) on SiO₂/Si wafers or on Mo foil (50-500 μm). On top of the Mo, a 1-3 μm thick layer of In is evaporated. This is then capped with a 30 nm layer of evaporated SiO₂. The entire stack is put into a tube furnace and heated in H₂ gas. Upon reaching the growth temperature of 750 °C, 10% phosphine (diluted in H₂) is introduced at 100 Torr for 10 minutes during which InP is grown. The thickness of the grown InP is ~2x the initial In thin film. Following the growth, the InP is *n*-type due to donor-like native defects. The as-grown InP is then converted to *p*-type through a solid-source gas-phase diffusion process using either zinc or zinc phosphide in a sealed ampoule or a close spaced sublimation configuration, which takes 1 hour at 425 °C. Subsequently, the SiO₂ cap is removed using a 1 minute neat HF etch. Then a 15 nm *n*-TiO₂ window layer is deposited by atomic layer deposition using titanium isopropoxide and water precursors at a temperature of 120 °C. A 55 nm ITO layer is sputtered on top of the TiO₂ as the transparent electrode. Sputtering was done at room temperature at 0.9 mTorr Ar pressure with a resulting sheet resistance of ~180 Ω/sq. The thickness of the combined TiO₂/ITO layers was optimized to minimize the reflectance, as described previously.³ The ITO is then patterned by photolithography

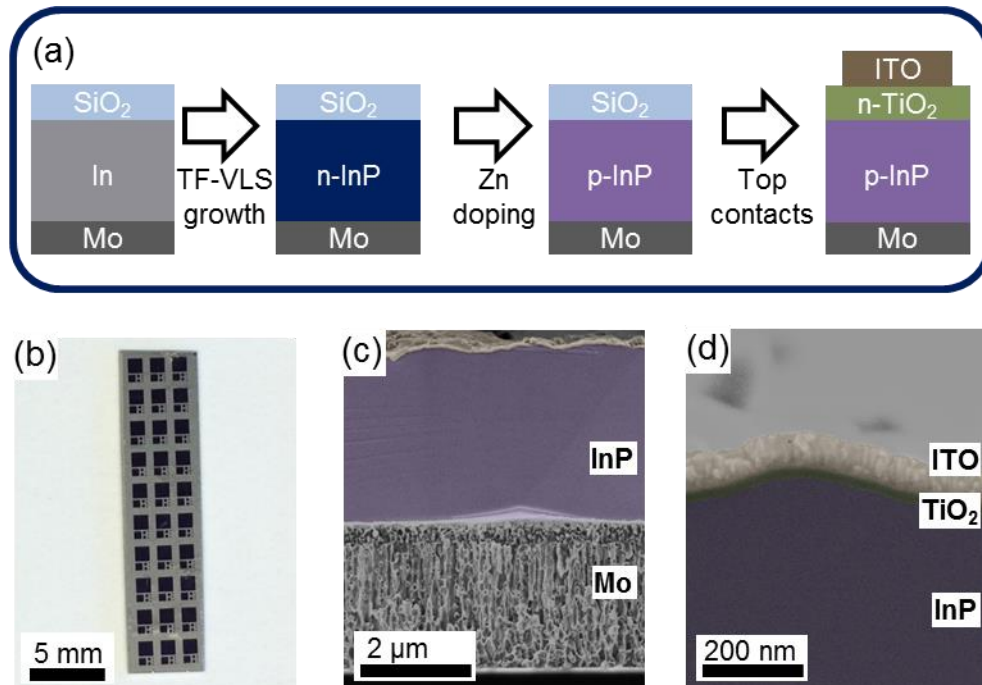


Figure 3. (a) Schematic showing the cell fabrication process. (b) Photograph of a completed chip with array of varying cell sizes. Dark areas are active cell regions. Cells are square with side lengths of 1 mm, 500 μm, 200 μm and 100 μm. (c) Cross section SEM image of a completed cell. (d) Higher magnification cross section SEM image of the near surface region of a completed cell. SEM images are false colored.

and etched using 1:3 HCl:H₂O into 1x1 mm² and smaller pads. Fig. 3b shows a representative finished chip, where the darker regions are the patterned ITO. The TiO₂ layer is highly resistive and the *p*-InP minority carrier diffusion length is in the range of 1-3 μm (discussed below), thus allowing the ITO pad to effectively define the active cell area resulting in a relative error on the current density of less than 2%. A cross section scanning electron microscope (SEM) image of a completed cell on sputtered Mo is shown in Fig. 3c, with a closer look at the front surface region shown in Fig. 3d.

4.4 OPTOELECTRONIC STRUCTURE

The optoelectronic uniformity of the InP thin film was examined by large-area PL imaging. Fig. 4a shows a top view optical microscope image of an as-grown *n*-InP layer. The surface roughness appears uniform overall with no features >1-2 μm. However in Fig. 4b, the PL image over the same area reveals a dendritic microstructure. Earlier studies have shown that in TF-VLS growth each individual nuclei undergoes dendritic growth.^{1,2} During the growth process, impurity segregation or accumulation of defects at the dendritic interfaces is believed to result in the observed contrast in luminescence. The PL intensity increases ~7× from the dark extremities to the bright backbone of the dendrites in the area depicted. The PL images were acquired using a 635 nm LED as the excitation source, double-polished GaAs as the long-pass filter, and an Andor Luca R camera.

After full fabrication of the device, EBIC was used to extract electrical properties of the InP layer. An electron beam is scanned over a device, and the local current collected is mapped to reveal the presence of defects and junctions. EBIC is frequently used to extract the depletion width and the minority carrier diffusion length in solar cells.^{4,5} Fig. 4c and 4d show a top view SEM image and the corresponding EBIC map over the same area, where darker regions correspond to a lower collection current. The surface roughness appears uniform with some ~3 μm features resulting from the growth, but EBIC reveals the underlying electronic structure. Here we used an accelerating voltage of 10 kV and a beam current of ~100 pA. Monte Carlo simulations using CASINO were used to determine the penetration depth and generation volume.⁶ We observe dark lines (lower current) that correspond to grain boundaries, as well as spatial variation in current collection within grains.

The EBIC line profiles across a grain boundary can be fit with a model to extract the local grain boundary recombination velocity (GBRV) and diffusion length (L_D).⁶ The model assumes a geometry where the grain boundary is perpendicular to the junction, which is assumed to be the case here. It also assumes L_D is much greater than the depletion width (W_D), an assumption justified from capacitance-voltage (CV) measurements discussed below. In the planar configuration, a perpendicular EBIC line scan across a grain boundary as shown in Fig. 5a will result in a profile like the example in Fig. 5b. This EBIC signal profile can then be modeled to extract the local minority carrier diffusion length (L_D) and the grain boundary recombination velocity (GBRV). In the model published by Romanowski and Buczkowski,⁷ the current ratio near a grain boundary is defined as

$$i = \frac{\Delta I}{I_0} = \frac{2}{\pi} S e^R \int_1^\infty \frac{\sin(R\sqrt{x^2 - 1})}{x(x + S)} e^{-\delta x} dx$$

$$S = v_s \frac{L_D}{D}$$

$$R = \frac{r}{L_D}$$

ΔI , I_0 , and δ are respectively the variation in current near a grain boundary, the background current, and the distance from the grain boundary to the center of the generation volume, as shown in Fig.

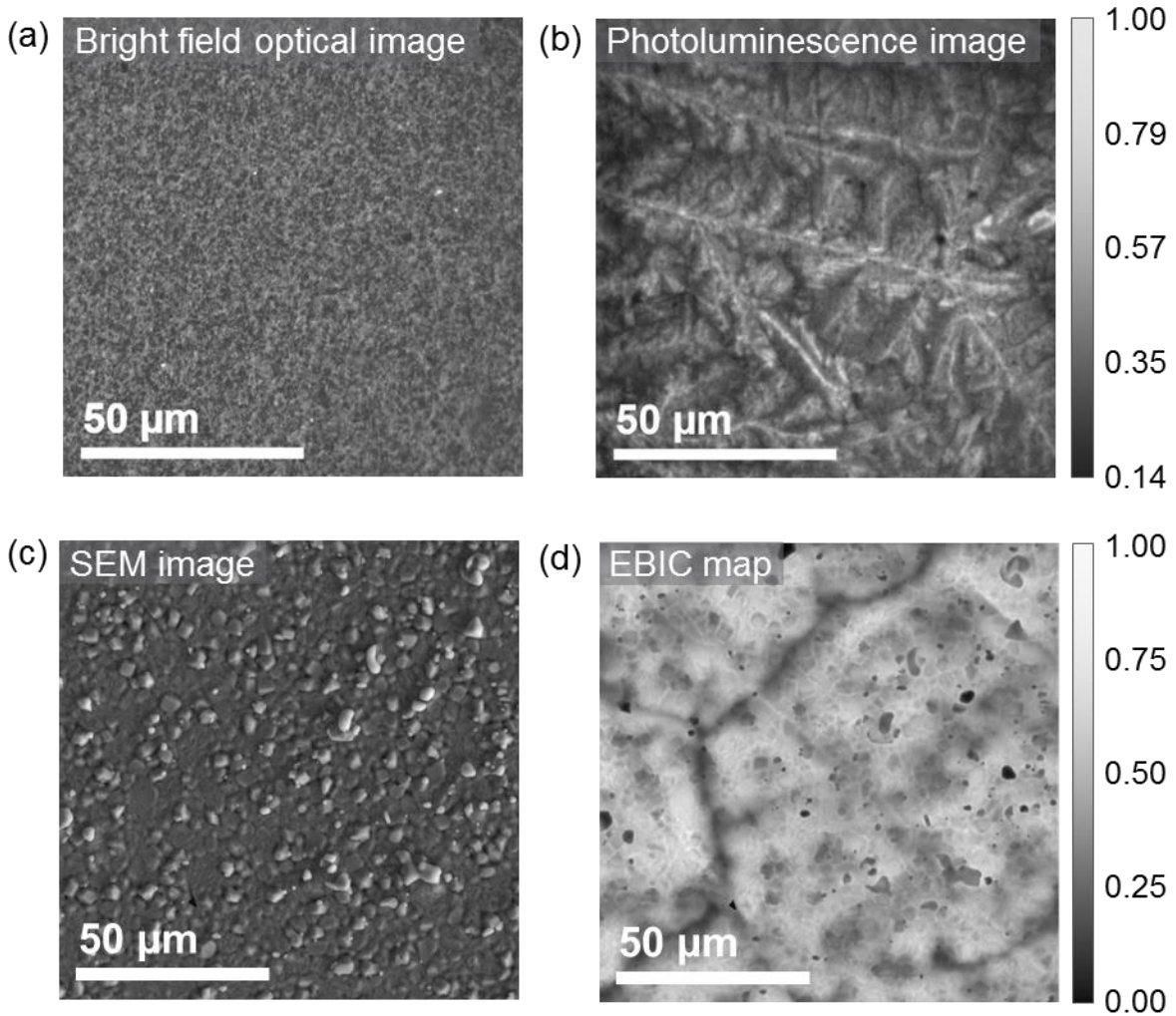


Figure 4. (a) and (b) show bright field optical and PL images from the same area for an as-grown n-InP sample. The surface roughness looks very uniform, but PL reveals a dendritic optoelectronic structure that mirrors known growth patterns. (c) and (d) show SEM and EBIC images from the same area (but different from (a) and (b)) of a Zn-doped device. Again the surface roughness is uniform but variation in the underlying electronic structure is visible. Grain boundaries are visible as dark lines and some surface occlusions can be seen. Intensity scale bars are in arbitrary units and normalized to the maximum intensity.

5b. L_D is minority carrier diffusion length, D is minority carrier diffusivity, v_s is grain boundary recombination velocity, and r is the radius of the generation volume (half of the penetration depth). The model assumes the generation volume is spherical with diameter equal to the penetration depth, the grain boundary is perpendicular to the surface, and the grain sizes are larger than the diffusion length. The effect of any depletion region at a grain boundary is not taken into account, which is also acceptable in our situation as the maximum possible depletion widths ($W_D \sim 100\text{-}250$ nm for $0.3\text{-}3 \times 10^{17}$ cm⁻³) are much less than extracted diffusion lengths. Fig 5c-f show representative measured and modeled current ratios across several grain boundaries, from which L_D is determined to be 1 to 3 μm with a GBRV of 1×10^5 to 4×10^6 cm/s. The accelerating voltage was 15 kV and a minority carrier diffusivity of 50 cm²/s was used. Note that in general, the two

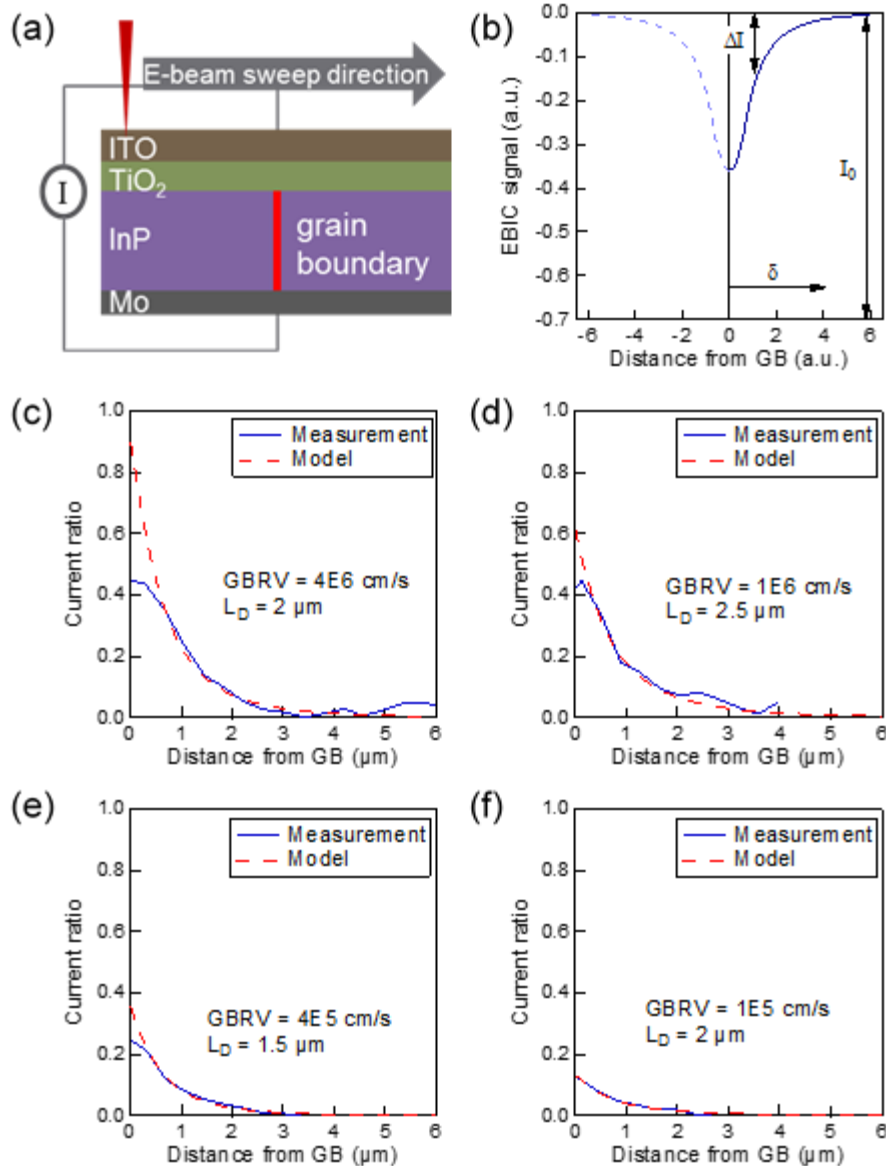


Figure 5. (a) Cross section schematic showing geometry of EBIC scan at grain boundary. (b) Example EBIC line profile taken perpendicular across a grain boundary. (c)-(f) Measured and modeled relative current ratio profiles at four different locations.

sides of a grain boundary need not have symmetrical profiles. In addition, the model does not fit the measured current ratios close to the grain boundary. This possibly stems from the geometries assumed or depletion region collection.

An alternative measurement geometry was used to confirm the L_D values, shown in Fig. 6a. In this geometry, the EBIC signal decreases as the beam is swept away from the junction region with the relation⁸

$$I_{EBIC} \propto x^a \exp(-x/L_D)$$

The factor of a depends on the surface recombination velocity as well as the junction depth below the contact.⁸ We set $a=0$ to get a lower bound on the diffusion length. Fig. 6b shows a plan view EBIC map. Line scans for the three representative locations indicated are plotted in in Fig. 6c-e. The extracted diffusion lengths are in the range 2.3-2.6 μm , which agrees well with that extracted near grain boundaries. The accelerating voltage was 20 kV.

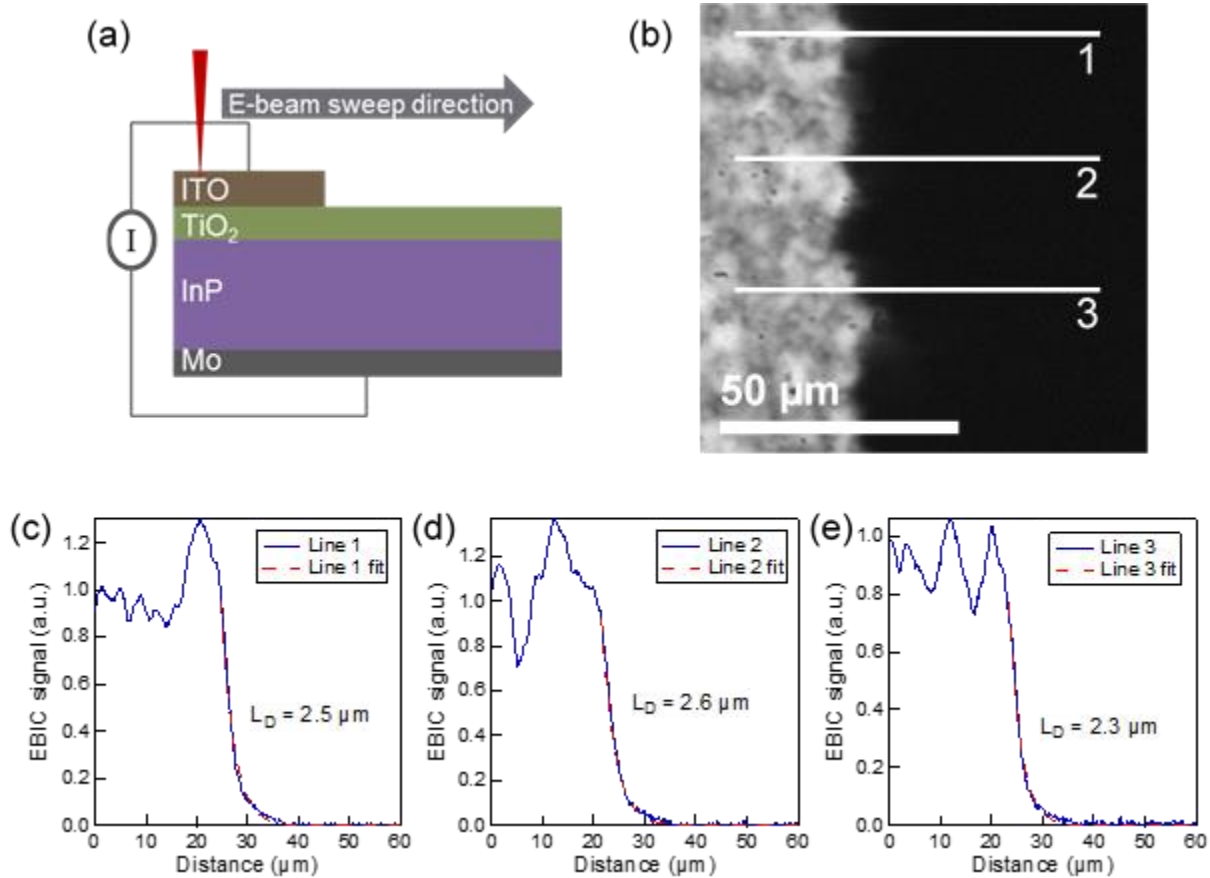


Figure 6. (a) Cross section schematic showing EBIC scan in the planar junction configuration. (b) Plan view EBIC map corresponding to geometry in (a). Bright region on the left is the ITO pad. (c)-(e) Measured line profiles and their fits from positions marked in (b).

In comparison, similarly doped single crystal p -InP has L_D of 1 to 40 μm and an untreated surface recombination velocity (SRV) of $\sim 10^3$ cm/s.⁹⁻¹¹ The doping concentration of the TF-VLS InP is discussed below. However, compared to the diffusion length in state-of-the-art CdTe (1 to 8 μm) and CIGS (0.5 to >2 μm),^{12,13} L_D values from TF-VLS InP are similar. The GBRV values are higher than the reported values for CdTe and CIGS, which are both $< 10^3$ cm/s.^{14,15} Impurity segregation at grain boundaries during the growth or doping stages can cause high defect densities and account for these differences. Additionally, the close proximity of the rear Mo contact can negatively affect the minority carrier recombination and thus the apparent diffusion length. However, due to the larger lateral grain sizes in TF-VLS InP compared to CIGS and CdTe,¹ there is a proportionately smaller density of grain boundaries and so they should have a relatively smaller effect on device performance.

To examine the nature of grain boundaries in more depth, we also looked at the ratio of at grain boundary to bulk (middle of grain) EBIC signal in the planar configuration at different accelerating voltages, shown in Fig. 7. At low voltage, electrons don't penetrate past the contact layers, so current collection is poor and the ratio is close to 1. For higher voltages the ratio is nearly constant and close to ~0.45. This is also the relative current loss at grain boundaries. The slight decrease in the ratio with increasing voltage can be attributed increasing penetration depth. Finally the ratio is <1, meaning the grain boundaries are not beneficial for collecting current, unlike in CdTe or CIGS.¹⁶⁻¹⁸

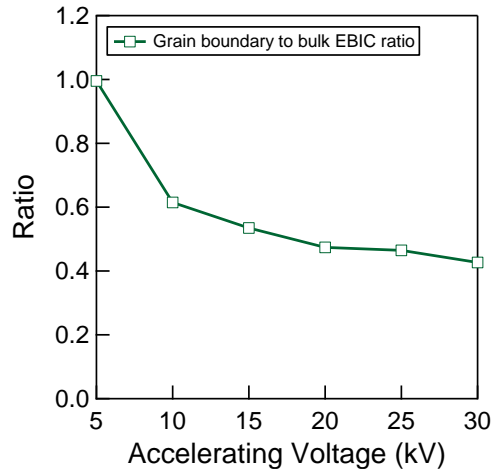


Figure 7. Ratio of EBIC signal at grain boundary to signal in the bulk grain.

4.5 *EX-SITU* P-DOPING USING ZN

The *ex-situ* Zn *p*-doping process used for TF-VLS InP was examined in detail. As an acceptor, Zn occupies substitutional indium sites,¹⁹ and is known in the literature to be a fast diffuser in InP with a substitutional-interstitial diffusion mechanism.²⁰⁻²² However, the diffusion coefficient at a given temperature also depends on the Zn concentration,²¹⁻²² phosphorous pressure²¹ and background donor concentration,²⁰ factors which all affect the vacancy concentration in the lattice. The hole concentration from Zn doped InP is reported to saturate at $\sim 1.5 \times 10^{18} \text{ cm}^{-3}$, where compensating donors and precipitates form.^{19,22-25} To obtain uniform doping in our TF-VLS InP, we chose a temperature and time regime that yields a Zn diffusion length much greater than the InP thickness. At 450 °C for 1 hour, the expected diffusion length is $\sim 4\text{-}5 \text{ }\mu\text{m}$,^{20-22,26} exceeding the InP thickness, but may be even higher due to the polycrystalline nature of our film. At temperatures lower than 400 °C, type conversion is not reliable, and at temperatures higher than 450 °C,

significant thermal decomposition occurs. The presence of phosphorus in the doping source helps prevent InP surface decomposition.

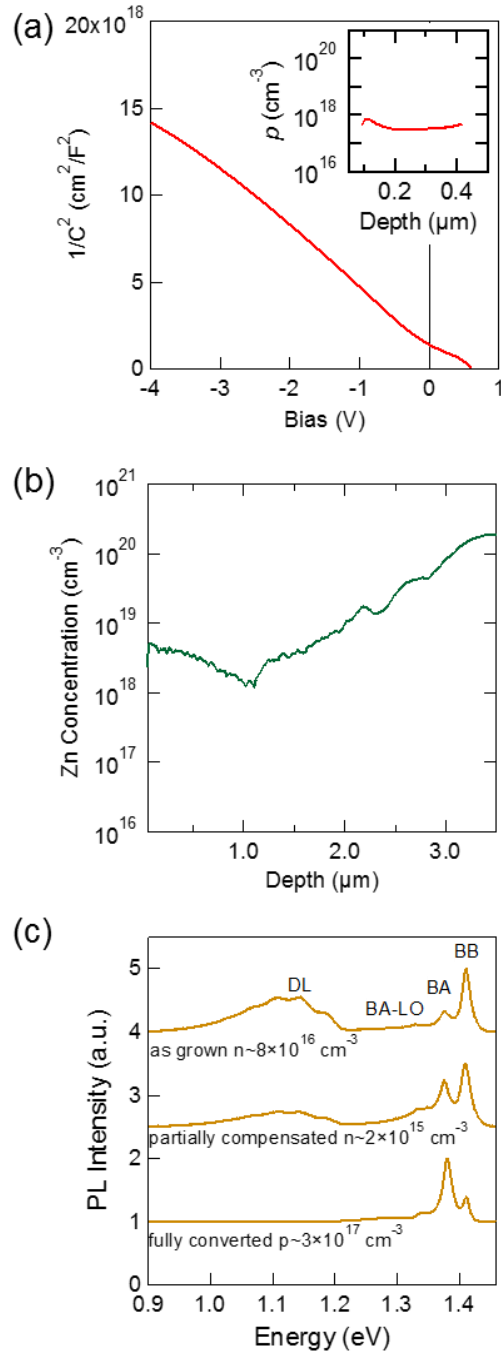


Figure 8. (a) Representative $1/\text{capacitance}^2$ -voltage measurement on a completed device. Inset shows the extracted hole concentration. (b) SIMS depth profile of Zn concentration. (c) PL spectra taken at 8 K. Top curve is from an as-grown sample ($n \sim 8 \times 10^{16} \text{ cm}^{-3}$), middle curve is from partially compensated sample ($n \sim 2 \times 10^{15} \text{ cm}^{-3}$), bottom curve is fully converted to p-type ($p \sim 3 \times 10^{17} \text{ cm}^{-3}$). Peak assignments are discussed in the text.

CV measurements of completed devices were carried out to determine the depletion width and net hole concentration near the surface after doping. 100 nm thick Au was deposited on top of the ITO to reduce series resistance. The net hole concentration vs. depth is extracted from the slope of the $1/C^2$ curve using the Mott-Schottky equations with the assumption of a one-sided junction.²⁷ Representative data are shown in Fig. 8a. The net hole concentration is relatively constant along the probed depth, and is between 3×10^{16} to $3 \times 10^{17} \text{ cm}^{-3}$ for different samples using the same doping conditions, corresponding to depletion widths of ~ 75 to 130 nm. Secondary ion mass spectroscopy (SIMS) analysis was then used to measure the Zn concentration as a function of depth (Fig. 8b). At the front surface the concentration is $\sim 5 \times 10^{18} \text{ cm}^{-3}$. The concentration of Zn is larger than the hole concentration near the surface, implying a dopant activation of $\sim 10\%$. We observe Zn segregation at the back InP-Mo interface with a back surface Zn concentration of $\sim 2 \times 10^{20} \text{ cm}^{-3}$. After doping, the Mo back contact also has a low contact resistance of $< 0.05 \text{ } \Omega \text{ cm}^2$ to p -type InP, measured using test structures with ZnAu top contacts. This effect may result from Zn segregation at the back interface creating a p^{++} region or alloy.

To further characterize defect state formation, low- temperature PL was also performed at different stages of the doping process (Fig. 8c): as-grown n -InP sample ($n \sim 8 \times 10^{16} \text{ cm}^{-3}$), a partially compensated Zn doped sample ($n \sim 2 \times 10^{15} \text{ cm}^{-3}$), and a fully converted Zn doped sample ($p \sim 3 \times 10^{17} \text{ cm}^{-3}$). Here the carrier concentrations correspond to the surface values extracted from Mott-Schottky measurements. The PL spectra have distinct peaks that were used to identify defects and states in the band gap by comparison to literature reports for comparably Zn doped single crystal InP. The measurement temperature was 8 K and the excitation source was the 488 nm line from an Ar ion laser. From the literature, we can identify the peaks from high to low energy as the band-to-band (BB) transition at 1.411 eV, the Zn band-to-acceptor (BA) transition at 1.376 eV, a small LO phonon replica of the BA transition (BA-LO) at 1.333 eV, and a broad peak relating to several deep levels (DL) below 1.2 eV.²⁹⁻³² In the partially compensated sample, the BA peak becomes stronger compared to the BB peak, and the intensity of the DL peaks decreases. These trends continue in the fully converted sample. The increase of the BA to BB peak intensity ratio in our samples is attributed to increased Zn doping. DL peaks do not appear in reference S-doped n -InP and Zn-doped p -InP wafers with similar concentrations. In the literature these peaks are associated with sources such as transition metal impurities and phosphorus vacancies.³³⁻³⁵ In our samples out-diffusion of metal impurities from the Mo substrate (99.95% purity) during the InP growth process is a potential explanation for the appearance of DL peaks, and their disappearance must be a result of Zn compensation or annealing out of those states during doping.

4.6 DEVICE PERFORMANCE AND CHARACTERIZATION

Following the doping study, we evaluated the solar cell performance of the completed devices. The band diagram under equilibrium is presented in Fig. 9a, which illustrates the electron selective behavior of the p -InP/ n -TiO₂ heterojunction, using $p = 3 \times 10^{17} \text{ cm}^{-3}$ in InP, $n = 7 \times 10^{16} \text{ cm}^{-3}$ in TiO₂, and previously reported band alignments.³ Electrically, the n -TiO₂ layer acts as an electron selective contact, due to its band alignment with p -InP.³ TiO₂ has a band gap of 3.4 eV and because its conduction band is aligned with that of InP, there is a large valence band offset of ~ 2 eV from the much smaller band gap of InP. Electrons can drift freely from the InP into the TiO₂, but holes are blocked by the band bending and the large valence band offset. Fig. 9b shows the dark and

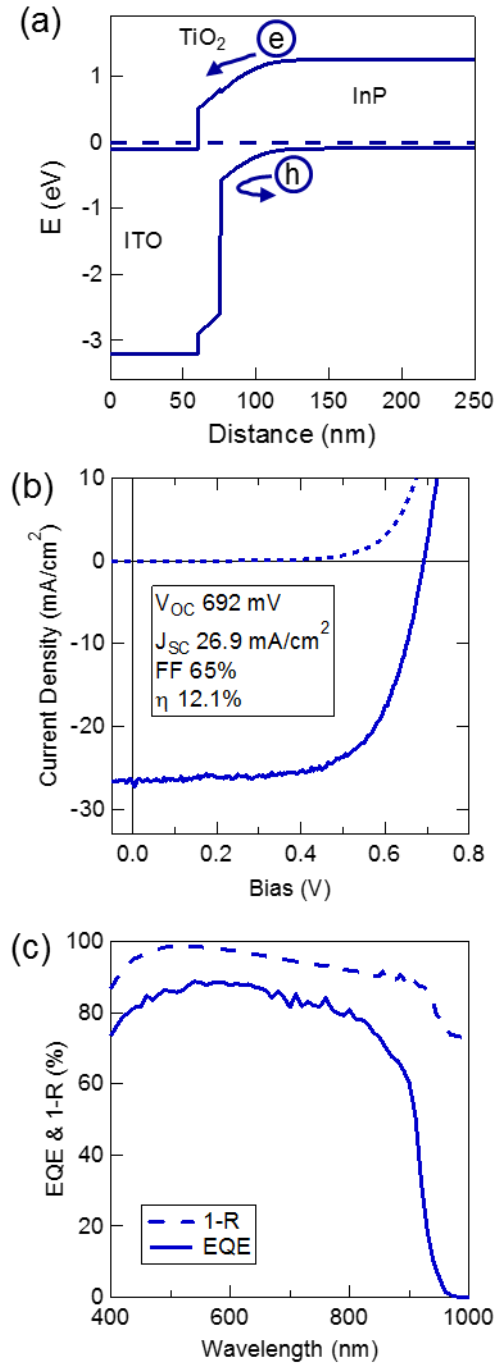


Figure 9. (a) Calculated equilibrium band diagram of the top surface region of the device. (b) J-V measurements for a cell under simulated 1-sun illumination (solid line) and in the dark (dotted line). Device parameters were V_{OC} of 692 mV, J_{SC} of 26.9 mA/cm², FF of 65%, and power conversion efficiency of 12.1%. Cell area was 0.5×0.5 mm². (c) Corresponding EQE and 1-R curves.

illuminated current density vs. voltage (J-V) for a 0.5×0.5 mm² cell. Due to the size of the cell, there is some uncertainty to the J_{SC} measurements due to possible edge effects.³⁶ A probe tip was used to directly contact the ITO pads at the corners, causing shadowing of ~9% of the active area.

From an EBIC line scan (supporting information) current collection did not extend past $\sim 2\text{-}3\ \mu\text{m}$ past the edge of the ITO pads, which leads to a $\sim 2\%$ relative error in the current density. A Solar Light 16S 300W solar simulator was used as the light source at 1-sun intensity ($100\ \text{mW}/\text{cm}^2$, AM1.5G) at $25\ ^\circ\text{C}$. This cell had the highest power conversion efficiency of 12.1% . The cell exhibits a V_{OC} of $692\ \text{mV}$, short-circuit current density (J_{SC}) of $26.9\ \text{mA}/\text{cm}^2$ (not corrected for shadowing), and fill factor (FF) of 65% . In comparison, to reach the InP Shockley-Queisser (SQ) limit of $\sim 33.5\%$ efficiency at 1 sun AM1.5G requires a V_{OC} of $\sim 1.08\ \text{V}$, J_{SC} of $\sim 34.9\ \text{mA}/\text{cm}^2$, and FF of $\sim 89\%$.^{37,38} Series and shunt resistances of $1.5\ \Omega\ \text{cm}^2$ and $1616\ \Omega\ \text{cm}^2$ were extracted by fitting the curve around open-circuit and past short-circuit. Parasitic resistances strongly limit the performance of this cell. The series resistance is due in part to the sheet resistance of the ITO layer, the thickness of which was primarily optimized for minimizing reflection. ITO contributes $>0.3\ \Omega\ \text{cm}^2$ to the series resistance in our measurement geometry.³⁹ The low shunt resistance may be caused by small pinholes in the InP film or conduction paths through grain boundaries; further study is needed. The reflection (1-R) and external quantum efficiency (EQE) of the cell is plotted in Fig. 9c. Extracting the current from the EQE gives $\sim 28\ \text{mA}/\text{cm}^2$, close to the measured J_{SC} value. The current loss due to reflection is $\sim 2.6\ \text{mA}/\text{cm}^2$. The step in the 1-R curve at the band edge of InP around $925\ \text{nm}$ is from sub-band gap light passing through the InP layer and reflecting from the Mo back contact. This shows that although the reflectivity of Mo is not high,⁴⁰ it may still enhance the current collection in the near infrared region where the absorption length ($\sim 1.3\ \mu\text{m}$ at $921\ \text{nm}$)⁴¹ is comparable to the film thickness. The EQE itself has a near constant offset from the 1-R until $\sim 850\ \text{nm}$, with the difference due to parasitic absorption or recombination losses.

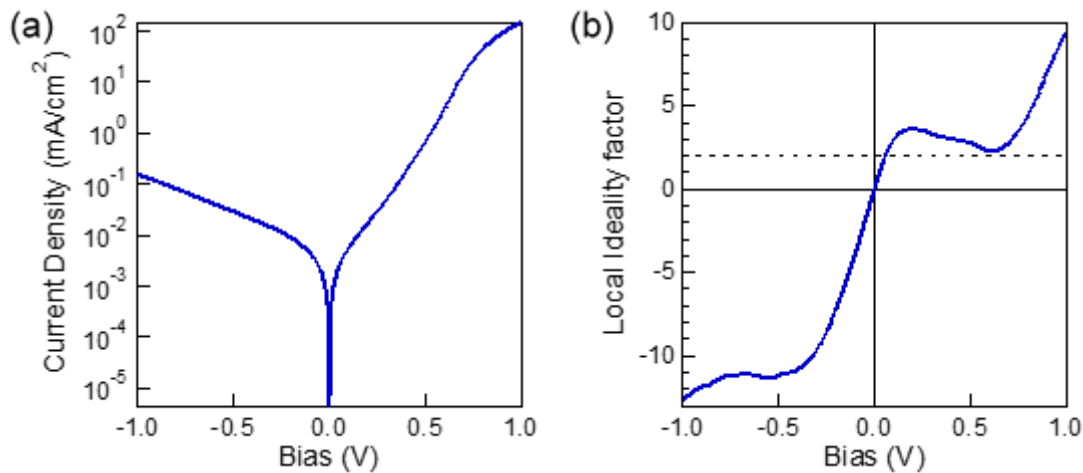


Figure 10. (a) Dark JV curve on semi-log scale. (b). Smoothed local ideality factor extracted from corresponding curves in (a).

The dark JV from Fig. 9b is plotted on a semilog scale in Fig. 10a. The corresponding local ideality factors are shown in Fig. 10b. In reverse bias, the current has an exponential dependence at smaller bias with an ideality factor $\sim 11\text{-}12$. In forward bias, a region with ideality factor ~ 3 appears at smaller bias, possibly due to a shunt. This gives way to a region with ideality factor ~ 2 , then at

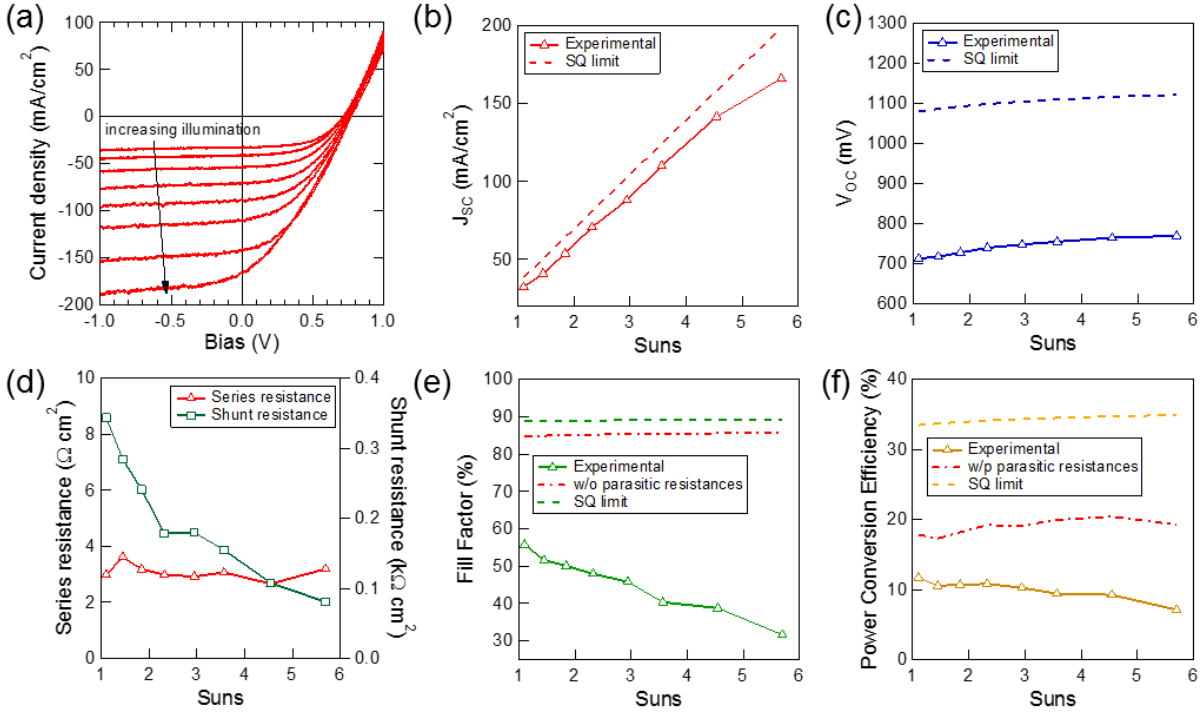


Figure 11. (a) External (η_{ext}) and internal (η_{int}) luminescence efficiency vs. illumination intensity from p-type TF-VLS InP. 1 equivalent sun illumination gives the same photon flux as a 1 sun AM1.5G source when using monochromatic 514 nm light instead. (b) The optical “J-V” curve corresponding to the η_{ext} in (a) is shown in green. Our previously published “J-V” curve for n-type InP is reproduced as well in red for comparison. Dashed line shows theoretical limit for InP.

higher bias the JV becomes series resistance dominated. Future work is necessary to assign features in the JV curve to physical features in cells. If we assume superposition holds, the expected V_{OC} for a J_{SC} of $\sim 27\text{-}28 \text{ mA/cm}^2$ is $\sim 750 \text{ mV}$ from the dark J-V in Fig. 10a. That this is not the case indicates the photocurrent is bias dependent.

The J-V of a representative cell ($1 \times 1 \text{ mm}^2$) was measured at illumination intensities from 1.1 to 5.7 suns (Fig. 11a), and compared to the theoretical ideal cases to examine sources of loss. Measurement temperatures were maintained in the range $27.6\text{-}28.6 \text{ }^\circ\text{C}$, leading to $\sim 2 \text{ mV}$ variation in V_{OC} and negligible impact on other parameters.⁴² The J_{SC} dependence on the illumination intensity is close to ideal (Fig. 11b). J_{SC} linearly increases with illumination intensity up to 4.5 suns, beyond which the series resistance begins to limit J_{SC} . The average J_{SC} (not correcting for shadowing by probe tip) is $\sim 85\%$ of the theoretical maximum, with $\sim 8\%$ loss due to reflection and the remainder due to probe shadowing, parasitic absorption in the window layers, and bulk and surface recombination. In Fig. 11c, the V_{OC} increases logarithmically with illumination intensity, as expected. The ideality factor extracted from the $J_{\text{SC}}\text{-}V_{\text{OC}}$ curve is ~ 1.41 , close to the value extracted by luminescence efficiency measurements discussed in detail below. An ideality factor ≥ 1 indicates non-radiative recombination, which reduces V_{OC} from the theoretical limit. Extrapolating the $J_{\text{SC}}\text{-}V_{\text{OC}}$ curve to 1 sun gives J_{SC} of 29 mA/cm^2 and V_{OC} of $\sim 708 \text{ mV}$.

The FF loss due to parasitic resistances is a major cause of lower efficiency in this device (Fig. 11d and 11e). In an ideal cell, the FF is expected to change only slightly with illumination intensity. In the measured cell, the parasitic series resistance is $\sim 3 \Omega \text{ cm}^2$ and the parasitic shunt resistance is 81 to $343 \Omega \text{ cm}^2$, which were extracted from the J-V curves near open-circuit and past short-circuit. The FF values of 31 to 55% are compared to the ideal case without parasitic resistances, which is plotted in Fig. 11e. In the ideal case, FF is determined by the V_{OC} and the ideality factor. With an ideality factor of 1 and the measured V_{OC} values, the FF would be $\sim 85\%$. Also shown is the theoretical FF of $\sim 89\%$ for this band gap in the SQ limit.³⁸ The measured power conversion efficiencies as a function of illumination intensity are plotted in Fig. 11f, which range from 7.1% (5.7 sun) to 11.7% (1.1 sun). We compare these efficiencies to the projected case without parasitic resistances, also shown in Fig. 11f. These projected efficiencies use the measured J_{SC} and V_{OC} values, but FF with parasitic resistances removed and ideality factor of 1. In this scenario the efficiencies reach 17.3% (1.1 sun) to 20.4% (4.5 suns). While it is unrealistic to assume parasitics can be fully removed, this provides a guide for future development.

4.7 OPTICAL “J-V” AND FUTURE POTENTIAL

To further study the future potential of InP thin film devices grown by the TF-VLS method we measured the external luminescence efficiency (η_{ext}), defined as the number of photons emitted per photon absorbed. From η_{ext} we extracted the internal luminescence efficiency (η_{int}), defined as the radiative recombination rate divided by the total recombination rate.⁴³ In a perfect material η_{int} is 100%. This means radiative recombination is the only carrier recombination mechanism, a necessary condition to reach the SQ limit. In addition, η_{ext} is directly related to the quasi-Fermi level splitting (ΔE_F) or maximum possible V_{OC} through the equation⁴⁴:

$$\Delta E_F = kT \ln \left(\frac{R_{abs}}{R_{em}} \right) + kT \ln(\eta_{ext})$$

$$R_{em} = \pi \int_{E_g}^{\infty} \frac{2n_r^2}{h^3 c^2} \cdot \frac{E^2}{e^{E/kT} - 1} dE$$

R_{abs} is the absorbed photon flux, R_{em} is the emitted black body photon flux at thermal equilibrium, n_r is the refractive index of air, k is the Boltzmann constant, T is the temperature, E is the photon energy, c is the speed of light, h is the Planck constant, and E_g is the band gap. Absorbance is assumed to be an angle-independent step function at the band gap and the factor of π arises from the assumption of Lambertian emission. The second term in the ΔE_F equation is the voltage loss due to $\eta_{ext} < 100\%$. Thus, η_{ext} is a measurement of the maximum V_{OC} achievable in the material, unconstrained by parasitic absorption or contact losses.⁴⁴ Fig. 12a shows measured η_{ext} and extracted η_{int} for different excitation intensities. The excitation source used was a 514 nm Ar ion laser, with intensities from 72 mW/cm^2 to $1.55 \times 10^6 \text{ mW/cm}^2$. The corresponding photon fluxes were converted to equivalent current densities ($J = q \times \text{flux}$) or AM1.5G equivalent suns. With a band gap of 1.344 eV, the total above band gap photon flux under 1 sun AM1.5G illumination is $\sim 2.2 \times 10^{17} \text{ cm}^{-2} \text{ s}^{-1}$ for InP. This photon flux corresponds to an absorbed power density of $\sim 84 \text{ mW/cm}^2$ for monochromatic 514 nm illumination, which we call 1 sun equivalent.

Fig. 12b shows the optical “J-V” curve in green corresponding to the measured η_{ext} in Fig. 12a. To understand the shape of the curve, we model it with the equation:⁴³

$$J \propto An + Bnp + C(np^2 + pn^2)$$

A, B, and C are the Shockley-Read-Hall (SRH), radiative, and Auger recombination coefficients, respectively. n and p are the electron and hole concentrations. Under low level injection, where the excess electron concentration (Δn) is much less than the background acceptor concentration (N_A), n and p are related to ΔE_F by²⁷

$$n \cong \Delta n = \frac{n_i^2}{N_A} \exp(\Delta E_F/kT)$$

$$p \cong N_A$$

Under high level injection, where Δn is greater than N_A , the relations become

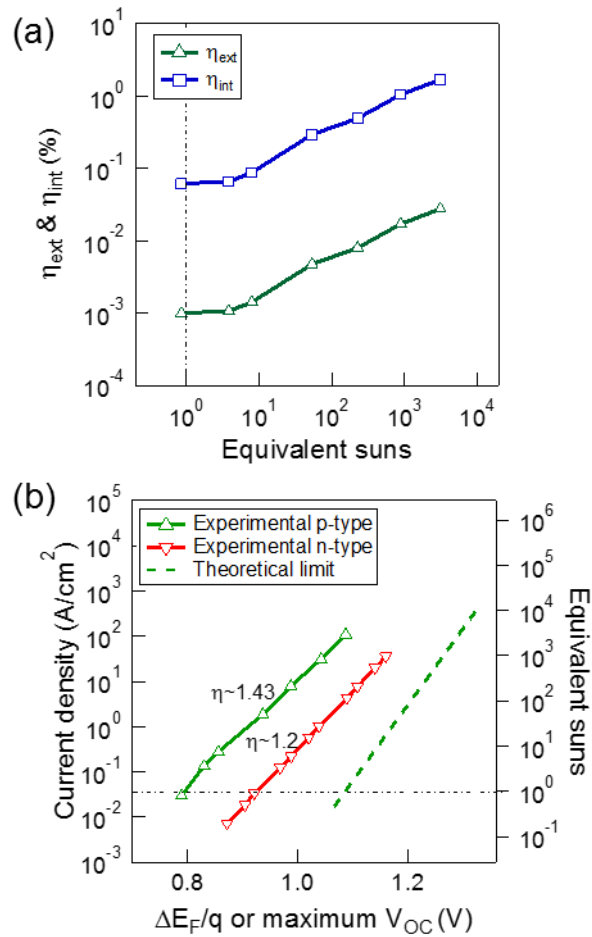


Figure 12. (a) External (η_{ext}) and internal (η_{int}) luminescence efficiency vs. illumination intensity from p-type TF-VLS InP. 1 equivalent sun illumination gives the same photon flux as a 1 sun AM1.5G source when using monochromatic 514 nm light instead. (b) The optical “J-V” curve corresponding to the η_{ext} in (a) is shown in green. Our previously published “J-V” curve for n-type InP is reproduced as well in red for comparison. Dashed line shows theoretical limit for InP.

$$n \cong \Delta n = n_i \exp(\Delta E_F / 2kT)$$

$$p \cong \Delta n$$

n_i is the intrinsic carrier concentration, k is the Boltzmann constant, and T is the temperature. If we then assume one recombination mechanism dominates, J is approximated as

$$J \cong J_0 \exp(\Delta E_F / \eta kT)$$

where η is the ideality factor. This ideality factor depends on the injection level as well as the dominant recombination mechanism. In low level injection, $\eta=1$ for all three recombination mechanisms. However, in high level injection, SRH recombination gives $\eta=2$, radiative recombination gives $\eta=1$, and Auger recombination gives $\eta=2/3$.⁴³ There are two factors this simple model does not include. The first is the exponentially decaying generation rate with depth that will produce a corresponding depth dependent injection level, and the second is the effect of a depletion region at the top surface. Both of these can lead to situations with simultaneous high level and low level injection resulting in η between 1 and 2. In Fig. 12b, we fit $\eta \sim 1.43$ for the optically implied “J-V” of our TF-VLS p -InP, and extract a $\Delta E_F/q$ of ~ 795 mV. While this indicates SRH recombination is present in our material, it is still higher than the electrically achieved V_{OC} of 692 mV and indicates there is room to improve in the optical and contact design of the device.

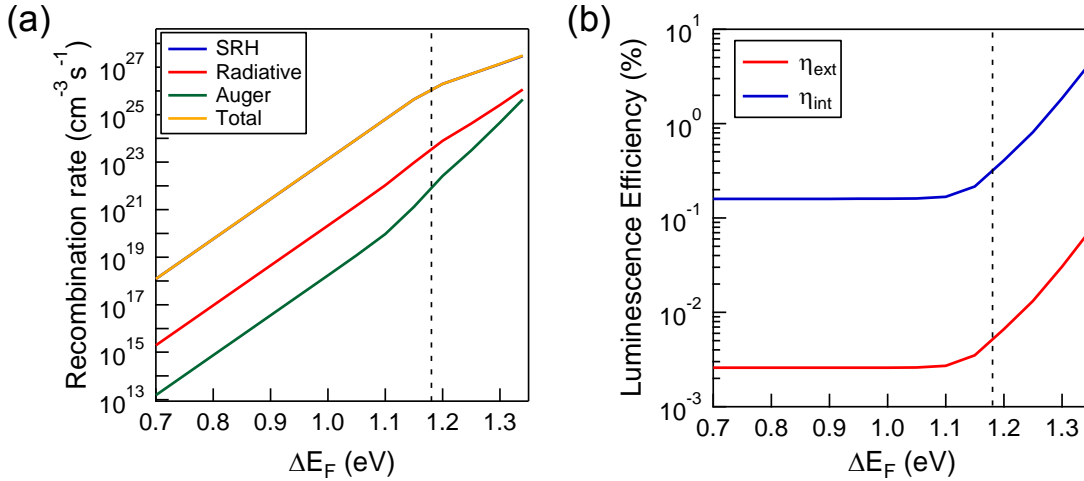


Figure 13. (a) Modeled total and individual recombination rates for SRH, radiative, and Auger mechanisms. SRH curve overlaps with total curve. (b) Modeled external and internal luminescence efficiency. Dashed line shows transition between low level and high level injection.

From this recombination model,⁴³ we can examine each contribution individually. From the InP literature, the radiative coefficient B is $\sim 2 \times 10^{-11} \text{ cm}^3 \text{ s}^{-1}$,⁴⁶ and the Auger coefficient is $\sim 1.6 \times 10^{-30} \text{ cm}^6 \text{ s}^{-1}$.⁴⁹ The SRH coefficient A is the inverse of the SRH lifetime and can be used as a fitting parameter. The carrier concentrations n and p can be expressed in terms of ΔE_F at a given doping concentration also as described in the main text. This allows us to plot recombination rate vs. ΔE_F , shown in Fig. 13a with $A = 1.25 \times 10^9 \text{ s}^{-1}$ and $N_A = 1 \times 10^{17} \text{ cm}^{-3}$. Auger recombination is negligible compared to the other two. Note that according to this model, at our extracted ΔE_F levels, low level

injection conditions hold so the expected ideality is 1. The ideality factors only differ at high level injection. In theory this implies we cannot distinguish between SRH or radiative dominated recombination from the measured ideality factor. In reality during the measurement there may be a depletion region at the surface and the photogeneration rate is not constant with depth, which both allow for high level injection near the surface. Additional assumptions here are that SRH transitions don't saturate, the rate is only governed by minority carrier lifetime, and the states are all at mid-gap.

The internal luminescence efficiency neglecting Auger recombination can also be defined as⁴³

$$\eta_{int} = \frac{Bnp}{Bnp + An} = \frac{1}{1 + \frac{A}{Bp}}$$

From this we can define an external luminescence under the assumption of a perfect reflecting rear mirror and randomly textured front mirror^{2,50}

$$\eta_{ext} = \frac{\eta_{int}}{1 + 4Ln^2\alpha(1 - \eta_{int})}$$

In this equation L is the film thickness, n is the refractive index at the band edge, and α is the absorption coefficient at the band edge. η_{int} and η_{ext} corresponding to Fig. 13a are plotted in Fig. 13b. They are both expected to be flat in low level injection as $p \sim N_A$, but at high level injection $p \sim \Delta n$ and increases with ΔE_F . Fitting our experimental η_{ext} with the model here gives rough estimates for minority carrier lifetimes of 0.1-2.6 ns.

Next we discuss sources of loss contributing to the difference in $\Delta E_F/q$ of bare material and electrical V_{OC} of finished devices. The luminescence efficiency measurement on bare InP samples takes into account recombination losses at the free top surface, in the bulk, and at the back Mo interface. The combined effect of these determines ΔE_F . After configuring the InP into a device, additional sources of loss are introduced which lower ΔE_F directly. The interface between the TiO₂ and InP, being non-epitaxial, can have a large defect density that causes increased non-radiative recombination. Another effect is that the band bending formed by the junction causes drift of minority carriers to the front surface where they recombine, resulting in a larger SRV than at a bare surface. Other factors produce a difference between $\Delta E_F/q$ and V_{OC} of finished devices, such as work function mismatches between the top ITO-TiO₂ contact and back Mo-InP contact, or low built-in potential due to low TiO₂ doping ($\sim 7 \times 10^{16} \text{ cm}^{-3}$). Finally, spatial variation in the luminescence efficiency (which can be seen in Fig. 4b) also contributes to this difference. The $\sim 7 \times$ spatial variation of PL intensity translates to $\sim 50 \text{ meV}$ variation in local ΔE_F , but the variation may be greater over larger areas. This effect could be modeled with band tails to explain lower V_{OC} , as recently studied in CZTS.⁴⁵

For comparison, our previously reported “J-V” curve for as-grown n -InP is reproduced in Fig. 12b with $\eta \sim 1.2$ and ΔE_F of $\sim 930 \text{ mV}$ at 1 sun illumination.¹ The theoretical limit for InP is also plotted as a dashed line for comparison. It is well known that n -type InP has much higher lifetimes than comparably doped p -type InP and thus the potential to reach a higher V_{OC} and efficiency.⁴⁶ However, the lack of a suitable, non-epitaxial hole selective window layer has limited the device

design options. This is an area of active research and will open up new possibilities in the future for using *n*-type InP as the absorber layer for higher performance.⁴⁷ A cell with V_{OC} of 930 mV has the potential to reach 24.1% power conversion efficiency assuming an achievable J_{SC} of 32 mA/cm² and fill factor of 81%.

4.8 CONCLUSIONS

In conclusion, we have introduced a new thin-film InP solar cell design, where large-grain InP is grown directly on a non-epitaxial Mo substrate using the TF-VLS method. We considered film morphology and uniformity, electrical behavior of grain boundaries, and effects of an *ex-situ* Zn doping process. The highest power conversion efficiency achieved under simulated 1 sun illumination is 12.1%, with V_{OC} of 692 mV, J_{SC} of 26.9 mA/cm², and FF of 65%. The highest measured V_{OC} is 692 mV at ~1 sun, while luminescence efficiency measurements indicate a potential V_{OC} of ~795 mV. The results presented here represent a promising starting point for further development of large-scale terrestrial III-V photovoltaics.

REFERENCES

1. R. Kapadia, Z. Yu, H.-H. H. Wang, M. Zheng, C. Battaglia, M. Hettick, D. Kiriya, K. Takei, P. Lobaccaro, J. W. Beeman, J. W. Ager, R. Maboudian, D. C. Chrzan and A. Javey, *Sci. Rep.*, 2013, **3**, 2275.
2. R. Kapadia, Z. Yu, M. Hettick, J. Xu, M. S. Zheng, C.-Y. Chen, A. D. Balan, D. C. Chrzan and A. Javey, *Chem. Mater.*, 2014, **26**, 1340–1344.
3. X. Yin, C. Battaglia, Y. Lin, K. Chen, M. Hettick, M. Zheng, C.-Y. Chen, D. Kiriya and A. Javey, *ACS Photonics*, 2014.
4. H. J. Leamy, *J. Appl. Phys.*, 1982, **53**, R51–R80.
5. O. Kurniawan and V. K. S. Ong, *IEEE Trans. Electron Devices*, 2006, **53**, 2358–2363.
6. D. Drouin, A. R. Couture, D. Joly, X. Tastet, V. Aimez and R. Gauvin, *Scanning*, 2007, **29**, 92–101.
7. A. Romanowski and A. Buczkowski, *Solid State Electron.*, 1985, **28**, 645–652.
8. D. S. H. Chan, V. K. S. Ong and J. C. H. Phang, *IEEE Transactions on Electron Devices*, 1995, **42**, 963–968.
9. L. Gousskov, H. Luquet, L. Soonckindt, A. Oemry, M. Boustani and P. H. Nguyen, *Journal of Applied Physics*, 1982, **53**, 7014–7019.
10. S. Bothra, S. Tyagi, S. K. Ghandhi and J. M. Borrego, *Solid-State Electronics*, 1991, **34**, 47–50.
11. Y. Rosenwaks, Y. Shapira and D. Huppert, *Phys. Rev. B*, 1991, **44**, 13097–13100.
12. G. Brown, V. Faifer, A. Pudov, S. Anikeev, E. Bykov, M. Contreras and J. Wu, *Applied Physics Letters*, 2010, **96**, 022104.
13. A. Morales-Acevedo, *Solar Energy*, 2006, **80**, 675–681.
14. G. Mendis, L. Bowen and Q. Z. Jiang, *Applied Physics Letters*, 2010, **97**, 092112.
15. W. K. Metzger, I. L. Repins, M. Romero, P. Diplo, M. Contreras, R. Noufi and D. Levi, *Thin Solid Films*, 2009, **517**, 2360–2364.
16. C.-S. Jiang, R. Noufi, K. Ramanathan, J. A. AbuShama, H. R. Moutinho and M. M. Al-Jassim, *Applied Physics Letters*, 2004, **85**, 2625–2627.
17. M. Kawamura, T. Yamada, N. Suyama, A. Yamada and M. Konagai, *Jpn. J. Appl. Phys.*, 2010, **49**, 062301.
18. C. Li, Y. Wu, J. Poplawsky, T. J. Pennycook, N. Paudel, W. Yin, S. J. Haigh, M. P. Oxley, A. R. Lupini, M. Al-Jassim, S. J. Pennycook and Y. Yan, *Phys. Rev. Lett.*, 2014, **112**, 156103.
19. R. S. Williams, P. A. Barnes and L. C. Feldman, *Appl. Phys. Lett.*, 1980, **36**, 760–762.
20. G. J. van Gurp, P. R. Boudewijn, M. N. C. Kempeners and D. L. A. Tjaden, *J. Appl. Phys.*, 1987, **61**, 1846–1855.
21. B. Tuck and A. Hooper, *J. Phys. D: Appl. Phys.*, 1975, **8**, 1806.

22. L. L. Chang and H. C. Casey Jr., *Solid State Electron.*, 1964, **7**, 481–485.
23. A. W. Nelson and L. D. WestBrook, *J. Cryst. Growth*, 1984, **68**, 102–110.
24. K. M. Yu, W. Walukiewicz, L. Y. Chan, R. Leon, E. E. Haller, J. M. Jaklevic and C. M. Hanson, *J. Appl. Phys.*, 1993, **74**, 86–90.
25. L. Y. Chan, K. M. Yu, M. Ben-Tzur, E. E. Haller, J. M. Jaklevic, W. Walukiewicz and C. M. Hanson, *J. Appl. Phys.*, 1991, **69**, 2998–3006.
26. H. S. Marek and H. B. Serreze, *Appl. Phys. Lett.*, 1987, **51**, 2031–2033.
27. S. M. Sze and K. K. Ng, *Physics of Semiconductor Devices*, John Wiley & Sons, 2006.
28. J. D. Plummer, M. Deal and P. D. Griffin, *Silicon VLSI Technology: Fundamentals, Practice, and Modeling*, Prentice Hall, Upper Saddle River, NJ, 1st edition., 2000.
29. S. Banerjee, A. K. Srivastava and B. M. Arora, *J. Appl. Phys.*, 1990, **68**, 2324–2330.
30. J. Chevrier, A. Huber and N. T. Linh, *J. Appl. Phys.*, 1980, **51**, 815–817.
31. E. Kubota, Y. Ohmori and K. Sugii, *J. Appl. Phys.*, 1984, **55**, 3779–3784.
32. Y. Moon, S. Si, E. Yoon and S. J. Kim, *J. Appl. Phys.*, 1998, **83**, 2261–2265.
33. M. S. Skolnick, E. J. Foulkes and B. Tuck, *J. Appl. Phys.*, 1984, **55**, 2951–2961.
34. H. Temkin, B. V. Dutt and W. A. Bonner, *Appl. Phys. Lett.*, 1981, **38**, 431–433.
35. H. Temkin, B. V. Dutt, W. A. Bonner and V. G. Keramidas, *J. Appl. Phys.*, 1982, **53**, 7526–7533.
36. C. R. Osterwald and K. A. Emery, *Solar Cells*, 1983, **10**, 1–5.
37. C. H. Henry, *Journal of Applied Physics*, 1980, **51**, 4494–4500.
38. M. A. Green, *Solid-State Electronics*, 1981, **24**, 788–789.
39. U. Malm and M. Edoff, *Prog. Photovolt: Res. Appl.*, 2008, **16**, 113–121.
40. B. W. Veal and A. P. Paulikas, *Phys. Rev. B*, 1974, **10**, 1280–1289.
41. O. J. Glembocki and H. Piller, in *Handbook of Optical Constants of Solids*, ed. E. D. Palik, Academic Press, Burlington, 1997, pp. 503–516.
42. P. Singh and N. M. Ravindra, *Solar Energy Materials and Solar Cells*, 2012, **101**, 36–45.
43. S. L. Chuang, *Physics of Photonic Devices*, Wiley, 2 edition., 2012.
44. O. D. Miller, E. Yablonovitch and S. R. Kurtz, *IEEE J. Photovolt.*, 2012, **2**, 303–311.
45. T. Gershon, B. Shin, N. Bojarczuk, T. Gokmen, S. Lu and S. Guha, *Journal of Applied Physics*, 2013, **114**, 154905.
46. Y. Rosenwaks, Y. Shapira and D. Huppert, *Phys. Rev. B*, 1991, **44**, 13097–13100.
47. G. Hautier, A. Miglio, G. Ceder, G.-M. Rignanese and X. Gonze, *Nat Commun*, 2013, **4**.
48. Y. Rosenwaks, I. Tsimberova, H. Gero and M. Molotskii, *Phys. Rev. B*, 2003, **68**, 115210.
49. O. Semyonov, A. Subashiev, Z. Chen and S. Luryi, *Journal of Applied Physics*, 2010, **108**, 013101.

50. O. D. Miller, *Photonic Design: From Fundamental Solar Cell Physics to Computational Inverse Design*, 2013.

CHAPTER 5

MANUFACTURING COST ANALYSIS OF TF-VLS GROWTH*

5.1 INTRODUCTION

Historically, III-V material systems grown by the vapor-solid method, such as metalorganic chemical vapor deposition (MOCVD), have been used in the highest performance solar cells,¹ especially in demanding extraterrestrial scenarios.² However, the cost of these cells in modules has been significantly higher than conventional electricity generators.³ These costs are driven by three main factors: epitaxial single crystal growth substrates, inefficient use of organometallic precursors, and capital depreciation due to low throughput.^{3,4} There is significant opportunity to reduce costs and increase performance if new process technologies can be developed to address these factors. Recently, we have created a new process called thin-film vapor-liquid-solid (TF-VLS) growth, which drastically mitigates the cost components above. The technique has been shown to yield high optoelectronic quality III-V thin films on non-epitaxial substrates, thus providing an attractive route for producing large scale III-V solar panels at high efficiency and low cost.^{5,6} However, no detailed cost analysis has yet been performed for this approach. Here, we present one such analysis using TF-VLS-grown InP configured in a standard thin-film module platform. The results show the potential of this new growth technique for lowering the cost of III-V photovoltaics.

We want to point out that the process flow and the associated cost structures described in this paper are applicable to other III-V materials with only minor adaptations. Additionally, although the focus in this paper is on photovoltaics, other applications that use III-Vs, such as power devices or solid-state lighting, may also benefit from this low-cost growth process.

* This chapter has been submitted for publication in a similar form.

5.2 CURRENT CELL STRUCTURE AND BENCHMARK CELL PERFORMANCE

A cell based on TF-VLS InP can be configured as an n -body or p -body device, with the n -body configuration more desirable due to the higher implied V_{OC} from luminescence efficiency measurements. However, a suitable window layer deposited by a non-epitaxial process has not yet been demonstrated for an n -body cell. For a p -body cell, amorphous titanium oxide (n -TiO₂) is an effective window layer, and our previously published n -TiO₂/ p -InP single crystal wafer-based devices have reached an efficiency of 19.2%.⁷ We have adapted this cell structure for our TF-VLS-grown InP, as shown in Figure 1(a). A 60 nm indium tin oxide (ITO) layer serves as our transparent conducting front electrode and anti-reflection coating. Below that is a 10 nm layer of n -TiO₂, which is deposited by atomic layer deposition (ALD). TiO₂ has an optical band gap of 3.4 eV, making it a high transparency window layer. Furthermore, the conduction bands of TiO₂ and InP are well aligned, which enables this heterojunction to freely extract minority electrons from the InP and

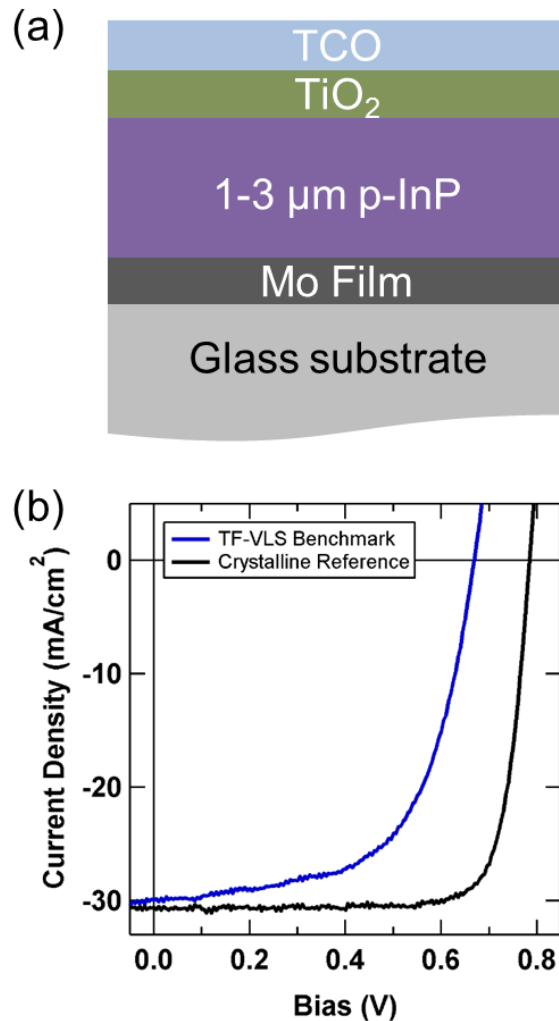


Figure 1. (a) Demonstrated InP cell showing ITO/ n -TiO₂/ p -InP/Mo device stack. (b) JV comparison of InP TF-VLS benchmark cell to crystalline InP reference cell.

block majority holes.⁷ The TiO₂ role is similar to that of the CdS window layer in CIGS or CdTe cells. Next is our 2 μm TF-VLS *p*-InP absorber layer, which was *ex-situ* doped using surface diffusion of Zn vapor at 425 °C. Finally, 1 μm Mo serves as the back contact.

As seen in Figure 1(b), preliminary *p*-body cells have reached AM1.5G power conversion efficiency of 12.3%, open-circuit voltage of 675 mV, short-circuit current density of 29.9 mA/cm², and fill factor of 61.0% with no finger grid over an area of 1x1 mm² defined by the ITO front electrode. For comparison, our reference cells fabricated on single crystal *p*-InP have reached power conversion efficiency of 19.2%, open-circuit voltage of 785 mV, short-circuit current density of 30.5 mA/cm², and fill factor of 80.1% with finger grid over an area of 5x5 mm².⁷ For both the TF-VLS and single crystal cell, the J_{SC} is short of the ~35 mA/cm² limit for InP under AM1.5G, and can be further improved using double layer anti-reflection coatings. The low fill factor of the TF-VLS cell can be improved in the future by using a finger grid and more optimized ITO.⁸ Although the open-circuit voltage of the TF-VLS cells is respectable for a first iteration, it is below the optically implied V_{OC}; thus, further improvements in the contacts are both possible and necessary. Due to the current growth scheme, Mo is necessarily the back contact to *p*-InP, but this is not ideal and may be a source of V_{OC} loss. The optimal contact technology and heterojunction structures for TF-VLS-grown material are still under development, but with maturation, could allow cells to approach the implied V_{OC}.

5.3 PROPOSED MODULE ARCHITECTURE AND MANUFACTURING PROCESS FLOW

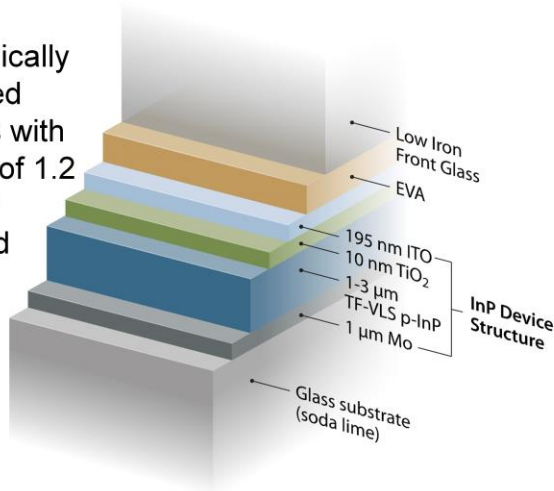
To perform a full module cost analysis, we are proposing an adaptation of a standard process for producing monolithically integrated CdTe or CIGS modules. These have been demonstrated already in high volume production^{9,10} and are proven low-cost technologies on a \$/m² basis.¹¹⁻¹³ Due to similar equipment requirements as for CIGS or CdTe growth, TF-VLS InP cells can be a drop-in replacement into existing module manufacturing processes. This minimizes process up-scaling risk and allows TF-VLS cells to benefit from module advancements.

A common misconception is that large-scale use of III-Vs is infeasible because the group III components are simply too expensive to be economical. However, with a move to thin-films and high materials utilization efficiency, this is not necessarily the case. The proposed cell structure used for cost analysis is similar to the one presented in the previous section with adjustments to allow for monolithic integration. Figure 2 shows the complete module and proposed process steps.

To begin, a 1 μm thick layer of Mo is sputtered onto a soda lime glass (SLG) substrate followed by the P1 laser scribe to isolate the back contacts for each cell. Next, a 1 μm thick layer of In is sputtered, along with a 50 nm SiO_x cap on top. Then, the TF-VLS growth is performed and afterwards the SiO_x cap is removed by an hydrofluoric acid (HF) rinse. The 10 nm TiO₂ layer is sputtered on, followed by the P2 scribe to the Mo substrate. ITO sputtering and the P3 scribe complete the monolithic cells. The module is then finished with standard busbar connections, ethylene vinyl acetate (EVA) and front glass encapsulation, and edge seals. The cost breakdown for each step is presented in the next section.

(a)

Monolithically
integrated
modules with
an area of 1.2
 \times 0.6 m²
assumed



(b)

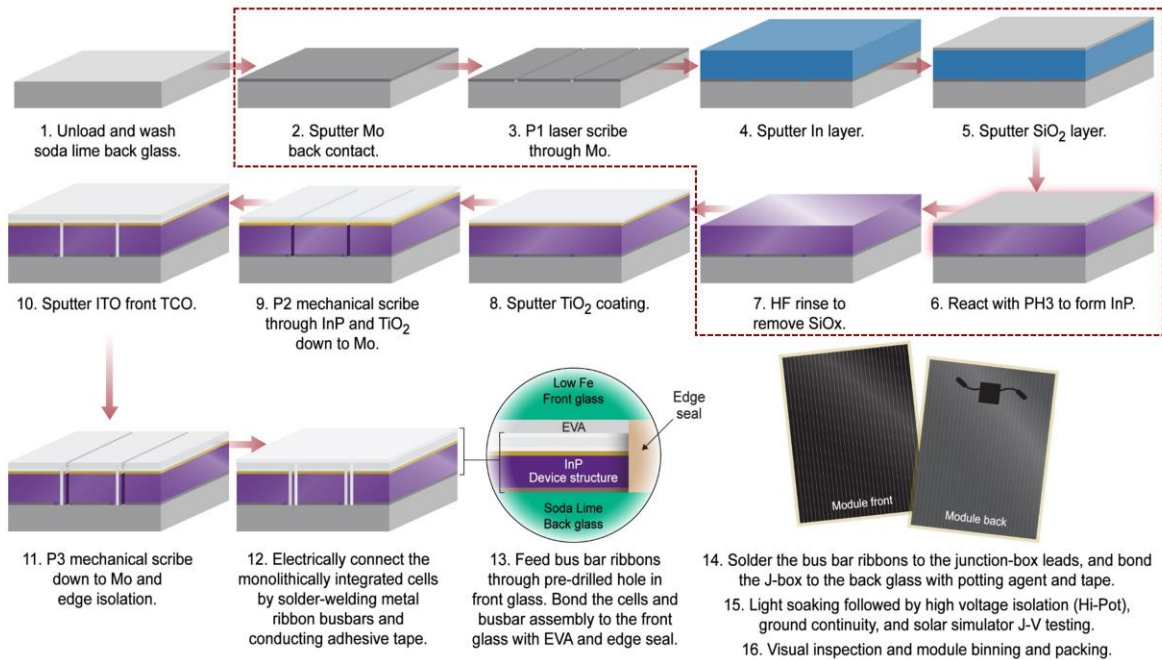


Figure 2. (a) InP module architecture showing cell and encapsulation. (b) Proposed manufacturing process flow for monolithically integrated TF-VLS InP module. Boxed steps are the TF-VLS growth process.

5.4 MANUFACTURING COST ANALYSIS

In order to help illuminate the cost drivers of this technology and understand its potential to compete with existing systems, the authors performed a manufacturing cost analysis of the InP module architecture described in Section 1. In order to compute these costs, the authors map out a potential process flow for manufacturing these modules at scale, shown in Figure 2(b), based on

conversations with manufacturers and experts in both industry and academia. Then, the cost of ownership for each step, which includes the materials, labor, depreciation, utilities, and maintenance costs are computed using a bottom-up cost model developed at NREL. These input data are gathered from material suppliers, equipment vendors, and industry, and then aggregated and anonymized since the data is often business sensitive. Step-by-step costs are then combined to obtain the total module costs. All calculations are performed in Excel.

5.4.1 Module cost components

As seen in Figure 3, for the benchmark 12% efficient module, the projected cost per watt peak is estimated at \$0.76 assuming 500 MW_(DC) annual production and U.S. manufacturing. \$0.26/W_(DC) of the total, or 34%, is due to the TF-VLS growth process. The cost of materials and equipment for each step is based on a survey of material suppliers, equipment vendors, and industry members. Labor counts were similarly based on discussion with industry and equipment vendors and are closely matched to industry norms. It is important to note that these cost calculations assume U.S. manufacturing and the purchase of new equipment for each step; lower costs can oftentimes be realized through the purchase of used or refurbished equipment. We assume an unskilled U.S. labor rate of \$22.16/hour and a skilled labor rate of \$32.00/hour with 40% benefits on wage and salary, although the actual wage rates will vary by location within the U.S. On an area basis, the projected

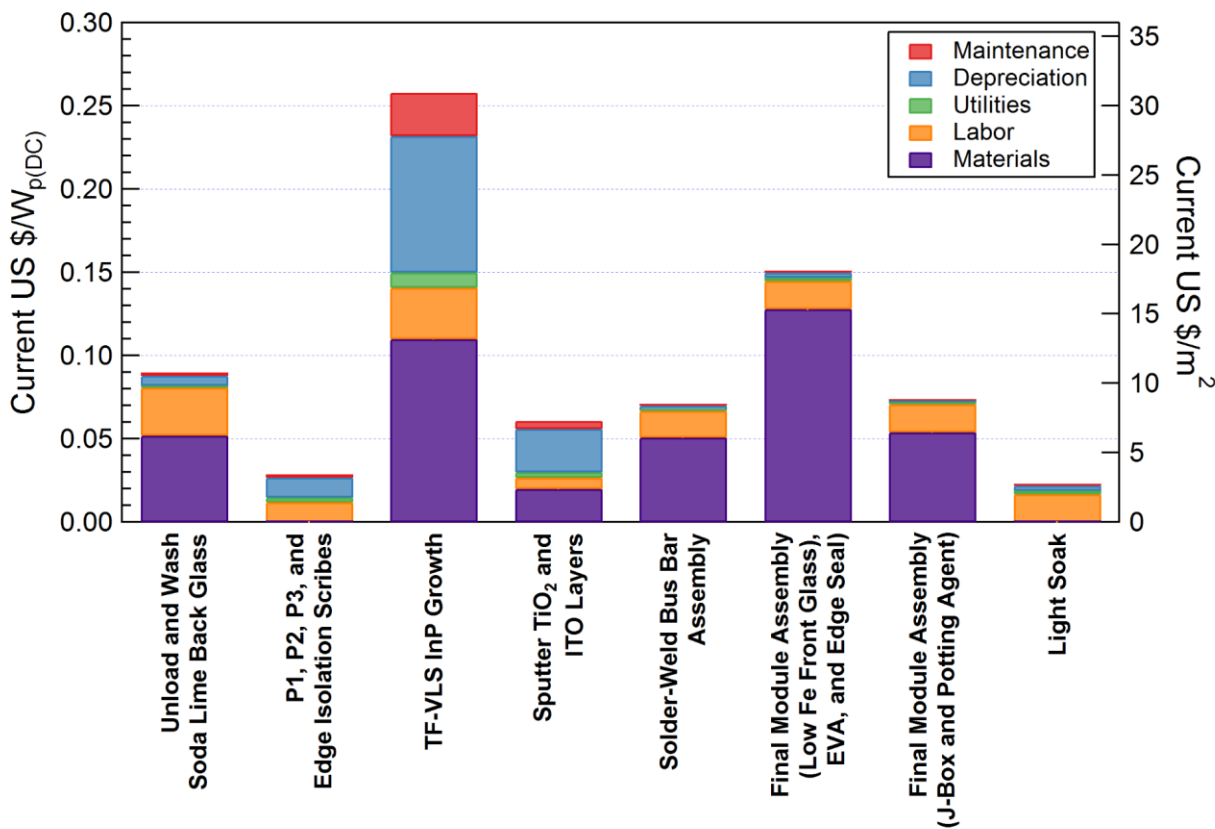


Figure 3. InP module cost breakdown. Total areal cost is \$91/m², with \$60/m² coming from non-TF-VLS steps.

cost is \$91/m² for the entire module and \$31/m² for the TF-VLS steps alone. The modules in our analysis are assumed to be monolithic modules with a size of 1.2x0.6 m².

5.4.2 Cost breakdown of InP TF-VLS growth

In this section, we describe assumptions made in analyzing each step, the cost advantages of the TF-VLS growth process versus MOCVD, as well as examine the similarities to CdTe and CIGS deposition. In traditional MOCVD, the three major components that substantially impact costs are the epitaxial wafer substrate, low materials utilization efficiency, and low throughput resulting in high capital depreciation costs.^{2,3} On the other hand, thin-film technologies such as CdTe and CIGS avoid all three issues, and thus are able to achieve a lower cost per square meter.¹¹⁻¹³ As the TF-VLS growth process for III-Vs parallels that of CdTe and CIGS deposition, it gains many of the same advantages. The entire TF-VLS growth process can be split into five main steps as shown in Figure 4, and detailed in the NREL bottom-up cost model.

First, a simple sputtered Mo on glass replaces the epitaxial wafer as the growth substrate. This represents a substantial manufacturing process gain as there is no longer the upfront cost of the wafer, re-surfacing, or breakage costs. The cost of 3.2 mm tempered SLG is estimated as \$6.26/m²,

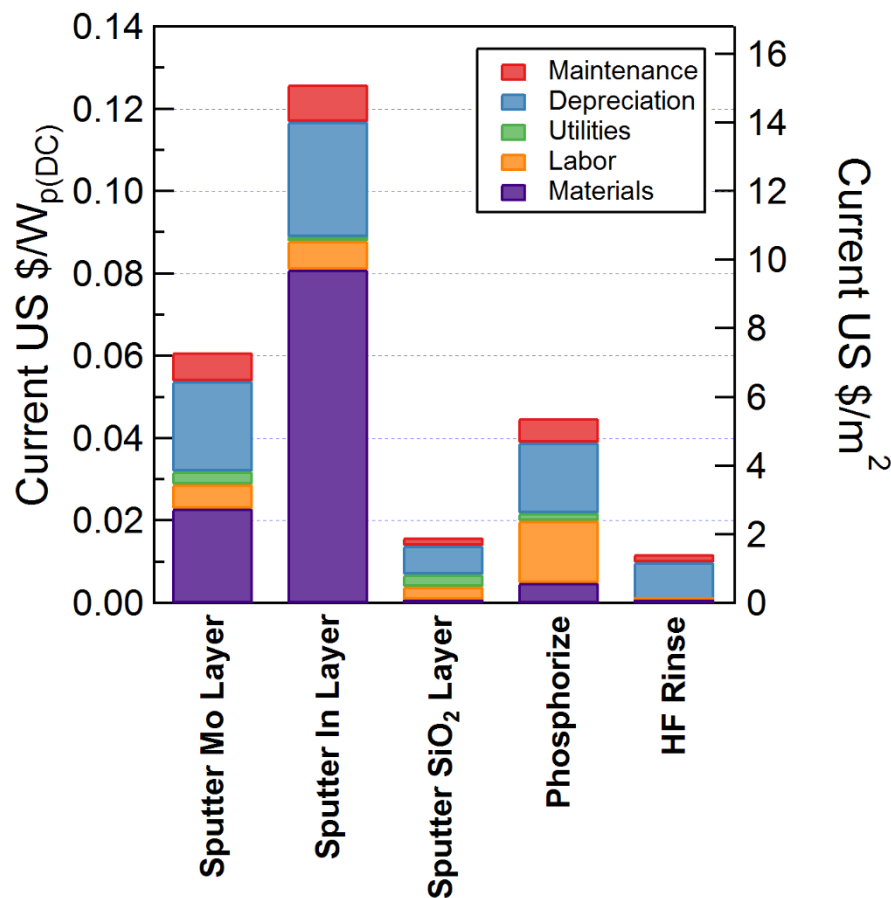


Figure 4. TF-VLS growth process cost breakdown. The total cost is \$31/m².

and the sputtered Mo is 1 μm thick. We assume the throughput of sputtering the Mo is 120 modules/hour and that the Mo target price is \$150/kg. Next, the In layer is sputtered onto the SLG substrate. Here the starting assumption is 1 μm of elemental In at \$650/kg pure element price plus a \$90/kg tolling charge, sputtered from rotatable source targets. In this case, the target utilization is typically 85% and the substrate collection efficiency is around 55%. For our materials costs calculation, we also assume that the 45% of In not collected by the substrate is recovered with 90% collection efficiency and has \$120/kg value, based upon advice provided by a relevant supplier. Even as the highest cost step in the process, the materials cost is still \$0.08/ $W_{\text{(DC)}}$ or $< \$10/\text{m}^2$, which is quite low compared to the use of metalorganic precursors such as trimethylindium. The price of In is sensitive to supply chain dynamics from competing uses such as ITO and CIGS.¹⁴ It is possible to move to electrodeposited In¹⁵ in the future with a goal of realizing higher materials utilization efficiency and increased ease of recovery. This would help to further decrease the sensitivity of module cost to In price increases. Subsequently, the 50 nm SiO_x cap layer is sputtered on top.

The second major step is phosphorization. As the process requirements for this step are very similar to those of the selenization/sulfurization steps in CIGS manufacturing, we assume similar tools can be used. Namely, the temperatures, pressures, and types of precursor are very similar. Using the specifications for the Wilro CIGS Selenization & Sulfurization furnace, and assuming a 2-minute reaction time, 50-minute heating time, 75-minute cooling time, and 40 module batch size, the estimated cost for phosphorization is \$5.38/ m^2 , or \$0.045/ $W_{\text{(DC)}}$ at 12% AM 1.5G power conversion efficiency. Additionally, a utilization efficiency of 70% for the phosphine was assumed, with a cost of \$350/kg. Finally, an HF rinse removes the SiO_x growth cap. Here we assume a 10:1 solution of $\text{H}_2\text{O}:\text{HF}$ with a materials cost of \$0.80/liter, and equipment costs and HF usage sourced from equipment vendors. The time to etch the 50 nm thick SiO_x layer was assumed to be 2.1 minutes with a 0.2-minute set-up time and 40 modules per batch.

5.4.3 High throughput enabled by TF-VLS growth

The growth process time depends on the temperature and PH_3 partial pressure (or equivalently, concentration) and is independent of the total area. The TF-VLS process is also relatively insensitive to the flow patterns in the chamber, dramatically simplifying chamber design compared to MOCVD. Additionally, by tuning the SiO_x cap thickness and porosity, P diffusion through the cap can be maximized. This diffusion rate is also controlled by the difference in chemical potential between the P in the vapor phase and the P dissolved in the In liquid. This means that the growth rate, to first order, is linearly dependent on the P partial pressure. For reference, a lab scale process with identical SiO_x cap and In thicknesses (50 nm/1 μm), yet a low PH_3 partial pressure of 10 Torr, already results in growth time of < 5 minutes. For industrial scale processes of ~ 100 Torr PH_3 partial pressure, growth times of < 2 minutes are reasonable. In the future, further gains in throughput may be found by combining load lock systems to minimize the time spent ramping the temperature.

5.5 MODULE COST PER WATT PROJECTIONS

For the benchmark 12% efficient module case, the total module costs are estimated to be \$0.76/W_(DC). With modest improvements in device performance within the mid-term, this would decrease to \$0.61/W_{p(DC)} for 15% efficient modules. In the long-term, assuming 930 mV open-circuit potential (the optically implied V_{oc}) and 24% efficient modules, \$0.40/W_{p(DC)} could be attainable. The estimated minimum sustainable prices (MSP) for these modules were also computed and are shown in Figure 5. All MSPs assumed sales, general, and administrative (SG&A); and research and development (R&D) costs of 7% and 5% of sales price, respectively. A 28% corporate tax rate, and 7-year, straight-line depreciation for equipment is also assumed. Note that SG&A and R&D costs can vary dramatically by company and according to the stage of a company's developments; our assumptions are based upon reasonable values observed within the financial statements of PV companies currently having greater than 1 GW production capacity. The nominal weighted average cost of capital (WACC) was assumed to be 15% for the benchmark case, 13% for the short-term case, and 9% for the long-term case, reflecting a potential for decrease in cost of capital as the technology matures and the perceived risk decreases. However, the WACC and its evolution in time also contain significant uncertainty, and thus the bulk of this analysis is more focused on module cost rather than MSP.

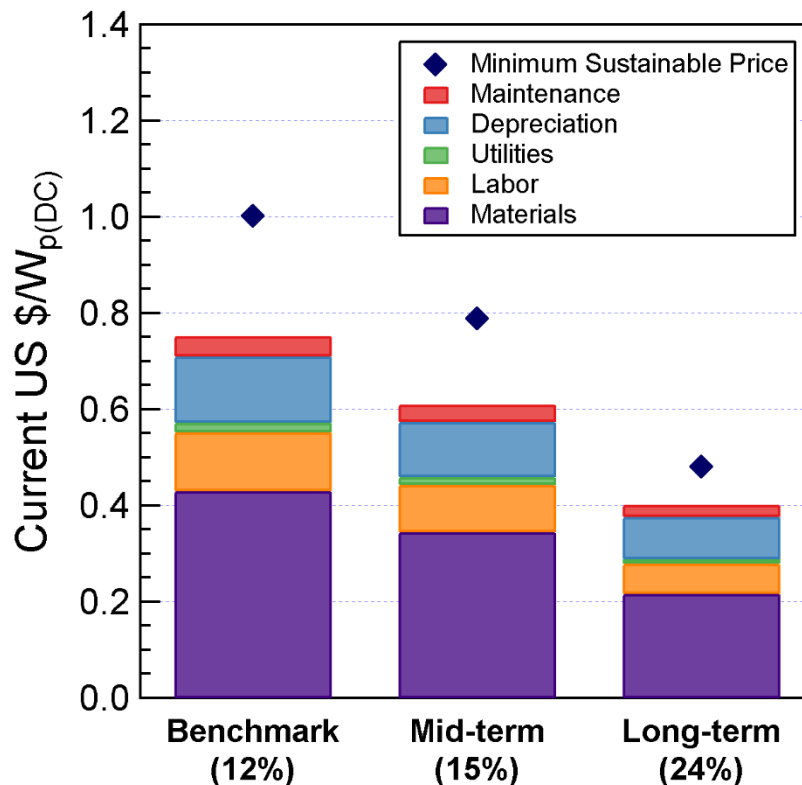


Figure 5. Projected module cost and minimum sustainable module price for benchmark (12% module efficiency, 15% WACC), short-term (15% module efficiency, 13% WACC), and long-term (24% module efficiency, 9% WACC) cases.

5.6 CONCLUSIONS

In this paper, we have presented a cost analysis of InP solar cell modules manufactured with the TF-VLS growth process on a standard monolithic thin-film module platform. The initial cell architecture is a simple stack of ITO/*n*-TiO₂/*p*-InP/Mo. At an annual production capacity of 500 MW_(DC), the short-term benchmark case of 12% efficient modules is expected to reach a cost of \$0.76/W_(DC) while the long-term potential case of 24% efficient modules is expected to reach a cost of \$0.40/W_(DC). We also demonstrate that the TF-VLS growth process is ideally suited to make more economical use of the group III metal In by both using it in elemental form and with higher utilization efficiency. TF-VLS growth addresses the three main cost components associated with traditional MOCVD growth: the epitaxial wafer substrate, low utilization efficiency of expensive metalorganic precursors, and high capital depreciation costs due to low throughput. Avoiding these issues enables a lower manufacturing cost of \$31/m² for the example of InP. In the future, it is also possible to use the TF-VLS growth process to produce low-cost epitaxial growth substrates for subsequent MOCVD growth of III-V heterojunctions to produce more complex multijunction devices. The TF-VLS process also has broader applicability, and may be used as the base for other industries such as integrated circuits, solid-state lasers, solid-state lighting, and power devices.

REFERENCES

1. Green MA, Emery K, Hishikawa Y, Warta W, Dunlop ED. Solar cell efficiency tables (version 44). *Progress in Photovoltaics: Research and Applications* 2014; **22**: 701–710. DOI: 10.1002/pip.2525.
2. Yoon H, Granata JE, Hebert P, *et al.* Recent advances in high-efficiency III–V multi-junction solar cells for space applications: ultra triple junction qualification. *Progress in Photovoltaics: Research and Applications* 2005; **13**: 133–139. DOI: 10.1002/pip.610.
3. Woodhouse M, Goodrich A. Manufacturing Cost Analysis Relevant to Single-and Dual-Junction Photovoltaic Cells Fabricated with III-Vs and III-Vs Grown on Czochralski Silicon. National Renewable Energy Laboratory 2014. <http://www.nrel.gov/docs/fy14osti/60126.pdf>
4. Bosi M, Pelosi C. The potential of III-V semiconductors as terrestrial photovoltaic devices. *Progress in Photovoltaics: Research and Applications* 2007; **15**: 51–68. DOI: 10.1002/pip.715.
5. Kapadia R, Yu Z, Wang H-HH, *et al.* A direct thin-film path towards low-cost large-area III-V photovoltaics. *Scientific Reports* 2013; **3**. DOI: 10.1038/srep02275.
6. Kapadia R, Yu Z, Hettick M, *et al.* Deterministic Nucleation of InP on Metal Foils with the Thin-Film Vapor–Liquid–Solid Growth Mode. *Chemistry of Materials* 2014; **26**: 1340–1344. DOI: 10.1021/cm403403v.
7. Yin X, Battaglia C, Lin Y, *et al.* 19.2% efficient InP heterojunction solar cell with electron selective TiO₂ contact. *ACS Photonics* 2014. DOI: 10.1021/ph500153c.
8. Battaglia C, Erni L, Boccard M, *et al.* Micromorph thin-film silicon solar cells with transparent high-mobility hydrogenated indium oxide front electrodes. *Journal of Applied Physics* 2011; **109**: 114501. DOI: 10.1063/1.3592885.
9. Dhere NG. Toward GW/year of CIGS production within the next decade. *Solar Energy Materials and Solar Cells* 2007; **91**: 1376–1382. DOI: 10.1016/j.solmat.2007.04.003.
10. Matsunaga K, Komaru T, Nakayama Y, Kume T, Suzuki Y. Mass-production technology for CIGS modules. *Solar Energy Materials and Solar Cells* 2009; **93**: 1134–1138. DOI: 10.1016/j.solmat.2009.02.015.
11. Green MA. Learning experience for thin-film solar modules: First Solar, Inc. case study. *Progress in Photovoltaics: Research and Applications* 2011; **19**: 498–500. DOI: 10.1002/pip.1057.
12. Woodhouse M, Goodrich A, Margolis R, *et al.* Perspectives on the pathways for cadmium telluride photovoltaic module manufacturers to address expected increases in the price for tellurium. *Solar Energy Materials and Solar Cells* 2013; **115**: 199–212. DOI: 10.1016/j.solmat.2012.03.023.
13. Zweibel K. Thin film PV manufacturing: Materials costs and their optimization. *Solar Energy Materials and Solar Cells* 2000; **63**: 375–386. DOI: 10.1016/S0927-0248(00)00057-X.

14. Woodhouse M, Goodrich A, Margolis R, James TL, Lokanc M, Eggert R. Supply-Chain Dynamics of Tellurium, Indium, and Gallium Within the Context of PV Manufacturing Costs. *IEEE Journal of Photovoltaics* 2013; **3**: 833–837. DOI: 10.1109/JPHOTOV.2013.2242960.
15. Lobaccaro P, Raygani A, Oriani A, Miani N, Piotta A, Kapadia R, Zheng M, Yu Z, Magagnin L, Chrzan DC, Maboudian R, Javey A. Electrodeposition of High-Purity Indium Thin Films and its Application to Indium Phosphide Solar Cells. *Journal of the Electrochemical Society* 2014; **161**: D794-D800. DOI: 10.1149/2.0821414jes

CHAPTER 6

SUMMARY AND FUTURE OUTLOOK

This dissertation makes the case for using InP in a fully non-epitaxial solar cell structure for large-scale photovoltaics. InP is a member of the III-V semiconductor family, which is well-known for high luminescence efficiency and thus suitability for high-efficiency photovoltaics.^{1,2} The problem for large-scale use of III-Vs in general has been the large cost of manufacturing by traditional methods. Alternative growth and fabrication techniques were explored using InP as a model material and their effect on device performance and manufacturability were presented here.

Chapters 2 and 3 explore growth of InP on non-epitaxial Mo substrates by MOCVD and CSS, respectively.^{3,4} The results from these studies demonstrate that InP optoelectronic quality is maintained even by growth on non-epitaxial metal substrates. Structural characterization by SEM and XRD show stoichiometric InP can be grown in complete thin films on Mo. The films are polycrystalline with columnar grains and have grain sizes on the order of 5-7 μm . Additionally, nucleation and morphology can be controlled by selectively patterning SiO_x (on which InP does not nucleate) and Mo. Photoluminescence measurements show peak energies and widths to be similar to those of reference wafers of similar doping concentrations.

In chapter 4 the TF-VLS growth technique is introduced and cells fabricated from InP produced by this technique are characterized. The TF-VLS method results in lateral grain sizes of $>500 \mu\text{m}$ and exhibits superior optoelectronic quality. Luminescence efficiency measurements indicate high potential V_{OC} of $\sim 930 \text{ mV}$ for as-grown n -type InP.^{5,6} An *ex-situ* Zn doping process was introduced to convert the InP to p -type. First generation devices using a n - TiO_2 window layer along with this p -type TF-VLS grown InP have reached $\sim 12.1\%$ power conversion efficiency under 1 sun illumination with V_{OC} of 692 mV, J_{SC} of 26.9 mA/cm^2 , and FF of 65%. The cells are fabricated using all non-epitaxial processing. Optical measurements show the InP in these cells have the potential to support a higher V_{OC} of $\sim 795 \text{ mV}$, which can be achieved by improved device design.

Chapter 5 describes a cost analysis of a manufacturing process using an InP cell as the active layer in a monolithically integrated module. The cell structure from chapter 4 is compatible with existing thin-film solar module processing flows and is used as the modeled active layer. Importantly, TF-VLS growth avoids the hobbles of traditional techniques: the epitaxial wafer substrate, low

utilization efficiency of expensive metalorganic precursors, and high capital depreciation costs due to low throughput. Production costs are projected to be $\$0.76/W_{(DC)}$ for the benchmark case of 12% efficient modules and would decrease to $\$0.40/W_{(DC)}$ for the long-term potential case of 24% efficient modules. A notable result is that the cost of the TF-VLS growth steps alone is only $\$31/m^2$, a drastic reduction compared to traditional methods. This enables TF-VLS growth to be relevant not only for photovoltaics, but also as a way to produce virtual growth substrates for other optoelectronic devices.

As the PV industry continues to grow, III-V semiconductors will play a bigger role due to their efficiency potential.⁷ The current PV market is composed almost solely of modules using single junction cells, the best of which are approaching the SQ limit. The results in chapter 5 show InP modules can be cost competitive in the PV market, but as the cell efficiencies get higher down the road, the module cost per watt will become dominated by non active-layer components like encapsulation, wiring, and assembly. These costs are largely fixed per unit area and so to reduce cost per watt further, device structures that have the potential to surpass the single-junction SQ efficiency limit are required to decrease the area needed to produce each watt.⁸ One prime candidate to achieve this is multi-junction cells, similar to what is currently being used in extraterrestrial applications.⁹ III-Vs are particularly suitable for multi-junctions as the ternary and quaternary compounds can be tuned to access band gaps spanning the solar spectrum. The non-epitaxial growth techniques presented here light the way for producing low-cost III-V multi-junctions, whether in tandem with proven single-junction cells or in completely new materials combinations. These possibilities point toward a promising future for InP and related III-V photovoltaics.

REFERENCES

1. H. Gauck, T. H. Gfroerer, M. J. Renn, E. A. Cornell and K. A. Bertness, *Appl Phys A*, 1997, **64**, 143–147.
2. I. Schnitzer, E. Yablonovitch, C. Caneau and T. J. Gmitter, *Applied Physics Letters*, 1993, **62**, 131–133.
3. M. Zheng, Z. Yu, T. J. Seok, Y.-Z. Chen, R. Kapadia, K. Takei, S. Aloni, J. W. Ager, M. Wu, Y.-L. Chueh and A. Javey, *Journal of Applied Physics*, 2012, **111**, 123112.
4. D. Kiriya, M. Zheng, R. Kapadia, J. Zhang, M. Hettick, Z. Yu, K. Takei, H.-H. Hank Wang, P. Lobaccaro and A. Javey, *Journal of Applied Physics*, 2012, **112**, 123102–123102–6.
5. R. Kapadia, Z. Yu, H.-H. H. Wang, M. Zheng, C. Battaglia, M. Hettick, D. Kiriya, K. Takei, P. Lobaccaro, J. W. Beeman, J. W. Ager, R. Maboudian, D. C. Chrzan and A. Javey, *Sci. Rep.*, 2013, **3**, 2275.
6. R. Kapadia, Z. Yu, M. Hettick, J. Xu, M. S. Zheng, C.-Y. Chen, A. D. Balan, D. C. Chrzan and A. Javey, *Chem. Mater.*, 2014, **26**, 1340–1344.
7. M. A. Green, K. Emery, Y. Hishikawa, W. Warta and E. D. Dunlop, *Prog. Photovolt: Res. Appl.*, 2015, **23**, 1–9.
8. J. Jean, P. R. Brown, R. L. Jaffe, T. Buonassisi and V. Bulović, *Energy Environ. Sci.*, 2015, **8**, 1200–1219.
9. <http://www.spectrolab.com/space.htm>

APPENDIX A

SUPPLEMENTARY INFORMATION FOR CHAPTER 3

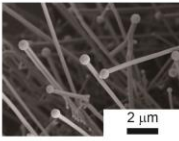
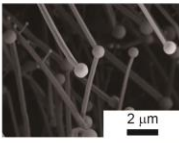
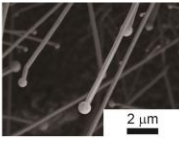
T_{sub} (°C)	T_{so} (°C)	P (Torr)	Growth time (min)	
485	650	1	30	
550	700	10	30	
550	700	40	30	

Figure S2. Growth conditions for InP nanowires with In-rich tips.

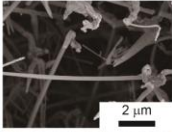
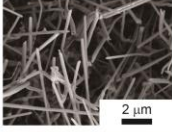
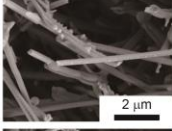
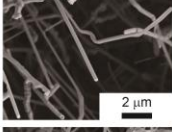
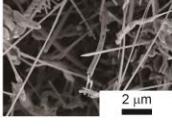
T_{sub} (°C)	T_{so} (°C)	P (Torr)	Growth time (min)	
500	700	1	30	
550	700	0.1	30	
550	700	1	30	
600	700	1	30	
650	700	1	30	

Figure S3. Growth conditions for straight InP nanowire.

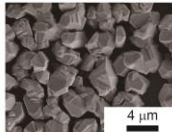
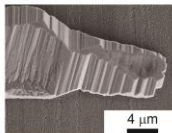
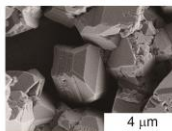
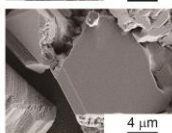
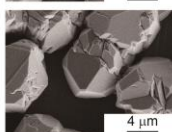
T_{sub} (°C)	T_{so} (°C)	P (Torr)	Growth time (min)	
600	800	0.2	15	
675	750	1	30	
675	785	1	60	
675	800	1	60	
680	800	0.1	30	

Figure S4. Growth conditions for polycrystalline InP at T_{sub} below 680 °C.

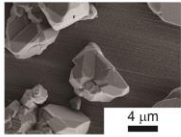
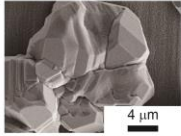
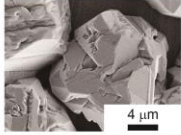
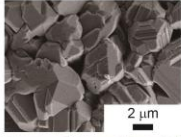
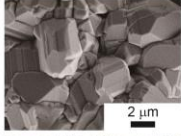
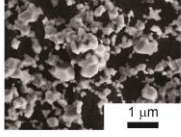
T_{sub} (°C)	T_{so} (°C)	P (Torr)	Growth time (min)	
685	700	1	30	
685	785	1	30	
685	785	1	60	
685	800	0.1	30	
685	800	1	30	
685	800	40	30	

Figure S5. Fabrication conditions for polycrystalline InP at $T_{\text{sub}} = 685$ °C. The data indicates that temperature of source (T_{so}) does not affect the crystalline morphology.

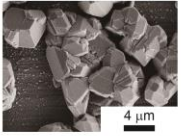
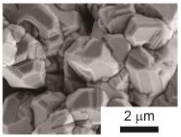
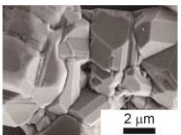
T_{sub} (°C)	T_{so} (°C)	P (Torr)	Growth time (min)	
700	750	0.1	30	
700	750	1	30	
700	770	1	30	

Figure S6. Growth conditions for polycrystalline InP at $T_{\text{sub}} = 700$ °C.